

PHOTOINITIATED DYNAMICS OF CLUSTER ANIONS VIA
PHOTOELECTRON IMAGING AND PHOTOFRAGMENT MASS
SPECTROMETRY

by

Luis Antonio Velarde

A Dissertation Submitted to the Faculty of the

DEPARTMENT OF CHEMISTRY

In Partial Fulfillment of the Requirements
For the Degree of

DOCTOR OF PHILOSOPHY

In the Graduate College

THE UNIVERSITY OF ARIZONA

2008

THE UNIVERSITY OF ARIZONA
GRADUATE COLLEGE

As members of the Final Examination Committee, we certify that we have read the dissertation prepared by Luis Antonio Velarde entitled Photoinitiated Dynamics of Cluster Anions via Photoelectron Imaging and Photofragment Mass Spectrometry and recommend that it be accepted as fulfilling the dissertation requirement for the Degree of Doctor of Philosophy.

Andrei Sanov

Date: 11 April 2008

Stephen Kukolich

Date: 11 April 2008

Mark Smith

Date: 11 April 2008

Craig Aspinwall

Date: 11 April 2008

Bonner Denton

Date: 11 April 2008

Final approval and acceptance of this dissertation is contingent upon the candidate's submission of the final copies of the dissertation to the Graduate College.

I hereby certify that I have read this dissertation prepared under my direction and recommend that it be accepted as fulfilling the dissertation requirement.

Dissertation Director: Andrei Sanov

Date: 11 April 2008

STATEMENT BY AUTHOR

This dissertation has been submitted in partial fulfillment of requirements for an advanced degree at The University of Arizona and is deposited in the University Library to be made available to borrowers under rules of the Library.

Brief quotations from this dissertation are allowable without special permission, provided that accurate acknowledgment of source is made. Requests for permission for extended quotation from or reproduction of this manuscript in whole or in part may be granted by the head of the major department or the Dean of the Graduate College when in his or her judgment the proposed use of the material is in the interests of scholarship. In all other instances, however, permission must be obtained from the author.

SIGNED: _____
Luis Antonio Velarde

ACKNOWLEDGEMENTS

I would like to express my great thanks to Professor Andrei Sanov. I could not have hoped for a better advisor for my Ph.D. Throughout these years as a graduate student, his enthusiastic and inspirational support has definitely made a mark in my life as a scientist. His mentoring and constructive criticism has definitely made me a better scientist, a better speaker, and a better writer. My warmest gratitude goes to Terefe Habteyes. Terefe and I worked together in the construction of the fragmentation apparatus while becoming good friends in the process. I have great admiration for his determination and drive. I will miss spending part of our mornings on the whiteboard discussing about some particular ion formation or dissociation mechanism or perhaps, sharing some Gaussian tips.

Big thanks to Emily Grumbling and Kostya Pichugin for the fruitful collaborations between the two machines, for your friendship, and for making the days in the lab more enjoyable. I wish you luck on your future careers! I am also grateful to past Sanov group members that I have been privileged to work with in previous years. Professor Richard Mabbs, who was a postdoc in the lab when I first joined the group and definitely an excellent role model for all of us. Many thanks to Eric Surber for his continuing friendship and for teaching me the fundamentals of vacuum technology and mass spectrometry on my first year of research. Thanks to Ahu Akin for her valuable comments and suggestions on data acquisition and analysis.

My deepest appreciation is also extended to my committee, Professors Steve Kukulich, Mark Smith, Bonner Denton, and Craig Aspinwall. I would also like to give special thanks to Professor Lucy Ziurys and Professor Richard Glass for the time they took to discuss with me about my research findings or my graduate education. I owe special thanks also to the machine and electronics shops from the Chemistry Department. Thanks to Lee, Ed, Marcus, and Mike, who besides their technical expertise that greatly helped us in our research, they were always willing to teaching me and share their own ideas that in most cases led to better designs of our components.

Thanks so much to all of the friends who have helped me through these years at The University of Arizona. Words cannot express my gratitude to my parents, my brother, and my sisters for their constant love and understanding. Thanks to Carmen Velarde for supporting my aspirations since I was a little kid. Finally Tomika, thank you for your patience through all the time that it took for me to write this dissertation. Thank you for your love and encouragement, for always being there to support me and expect nothing but the best of me.

DEDICATION

To my wife Tomika

TABLE OF CONTENTS

LIST OF FIGURES	9
LIST OF TABLES	12
ABSTRACT	13
CHAPTER 1 GENERAL INTRODUCTION	15
1.1 Anion photochemistry: Competitive pathways	16
1.2 Negatively Charged Clusters and Anion Solvation	17
1.3 Photoelectron Imaging of Negative Ions	19
1.4 Anion Photodissociation: Where does the excess electron go?	21
1.5 Overview of this Dissertation	23
CHAPTER 2 EXPERIMENTAL METHODS	25
2.1 Overview	25
2.2 Vacuum Hardware	29
2.3 Ion Production	30
2.4 Linear Time-of-Flight Mass Spectrometer	33
2.5 Laser Interaction and Mass Selection	37
2.6 Reflectron Time-of-Flight Mass Spectrometer	39
2.7 Photoelectron Imaging	44
CHAPTER 3 MOLECULAR AND CLUSTER ANIONS OF CARBON DIOXIDE	55
3.1 An Excess Electron on Carbon Dioxide	55
3.1.1 Long-Lived 2A_1 Metastable State of CO_2^-	56
3.1.2 Temporary Anion States	58
3.2 Negatively Charged Clusters of Carbon Dioxide	62
3.2.1 Cluster Formation	62
3.2.2 Cluster Geometries and Electronic Isomers	67
3.3 Cluster Photochemistry and Photoelectron Dynamics	69
3.3.1 Cluster Photofragmentation	69
3.3.2 Photoelectron Imaging of $(CO_2)_n^-$	72
3.4 Summary	83

TABLE OF CONTENTS – *Continued*

CHAPTER 4	PHOTODISSOCIATION OF CO_2^- IN WATER CLUSTERS	86
4.1	Introduction	86
4.2	Experimental Details	88
4.3	Results	89
4.4	Discussion	92
4.4.1	Trapping of the excess electron on CO_2 : Stabilization by Hydration	95
4.4.2	Core Dissociation Mechanism for the $\text{CO}_2^-(\text{H}_2\text{O})_m$ Clusters	96
4.5	Summary	100
CHAPTER 5	PHOTODETACHMENT AND PHOTOFRAGMENTATION PATHWAYS IN THE $[(\text{CO}_2)_2(\text{H}_2\text{O})_m]^-$ CLUSTER ANIONS	101
5.1	Introduction	101
5.1.1	The $[(\text{CO}_2)_n(\text{H}_2\text{O})_m]^-$ Cluster Series	101
5.1.2	Decay Channels for Excited Clusters	103
5.1.3	A Hydrated Dimer Anion?	104
5.2	Experiment	105
5.3	Results and Analysis	106
5.3.1	Photoelectron Images and Cluster Structure	106
5.3.2	Photofragment-Ion Mass Spectra	112
5.4	Discussion	113
5.4.1	Charge Localization in $[(\text{CO}_2)_2(\text{H}_2\text{O})_m]^-$, $m = 2-11$	113
5.4.2	Solvent-Evaporation and Core-Dissociation Pathways in $[(\text{CO}_2)_2(\text{H}_2\text{O})_m]^-$, $m = 3-11$	119
5.4.3	Photoinduced Ion-Molecule Reaction in $\text{CO}_2^-(\text{H}_2\text{O})_m\text{CO}_2$, $m = 3-6$ Cluster Anions	120
5.4.4	Channel Competition	123
5.5	Summary	125
CHAPTER 6	SOLVENT RESONANCE EFFECT ON THE ANISOTROPY OF $\text{NO}^-(\text{N}_2\text{O})_n$ CLUSTER ANION PHOTODETACHMENT	127
6.1	Introduction	127
6.2	Experimental	129
6.3	Results and Data analysis	130
6.3.1	Photoelectron images and energy spectra	130
6.3.2	Photoelectron angular distributions for unsolvated NO^-	137
6.3.3	Solvation effects on photoelectron anisotropy	140
6.4	Discussion	143
6.5	Summary	148

TABLE OF CONTENTS – *Continued*

CHAPTER 7	OBSERVATION OF THE CH_3SOCH^- AND $\text{CH}_3\text{SOCH}^-\cdot\text{H}_2\text{O}$ ANIONS: A PHOTOELECTRON IMAGING AND PHOTOFRAGMENTATION STUDY	149
7.1	Introduction	149
7.2	Experimental Setup	151
7.3	Results	153
7.3.1	Photoelectron Imaging of CH_3SOCH^- , CH_3SOCH^- , and HCSO^-	153
7.3.2	Photofragmentation Spectra	158
7.3.3	Isomeric Structures and Computational Results	160
7.4	Discussion	163
7.4.1	Photodetachment Bands	163
7.4.2	Dissociation Mechanisms	165
7.5	Summary	170
CHAPTER 8	PHOTOELECTRON IMAGING OF ACETONITRILE CLUSTER ANIONS	172
8.1	Dipole-Bound Anions of CH_3CN	172
8.2	The HCCN^- and H_2CN^- anions	174
8.2.1	Photoelectron Imaging of the $\text{HCCN}^-(\text{H}_2\text{O})_n$ Cluster Anions	178
8.2.2	$\text{H}_2\text{CCN}^-(\text{CH}_3\text{CN})_n$ Series	178
CHAPTER 9	CONCLUSIONS AND FUTURE OUTLOOK	179
9.1	Dissertation Summary	179
9.2	Future Directions	181
9.2.1	Photoelectron Imaging of Mass-Selected Photofragments	181
9.2.2	Studies of Hydration Stabilized Anions	183
9.2.3	$[\text{M}-n\text{H}]^-$, $n = 1, 2$ Anions	183
REFERENCES	185

LIST OF FIGURES

1.1	Schematic photoelectron energy diagram and anionic transitions.	20
1.2	Simulated photoelectron angular distributions as a function of the anisotropy parameter β	22
2.1	Schematic diagram of the experimental apparatus.	27
2.2	Detailed mechanical drawing of the apparatus.	28
2.3	Bias network for the ion MCP detector.	36
2.4	Mass spectra of $\text{O}_2^-(\text{H}_2\text{O})_n$ cluster anions by expansion of air (1 atm.) . .	38
2.5	Event timing sequence for a nanosecond laser system.	40
2.6	Photofragment acquisition demonstrated for the N_2O_2^- anion at 532 nm .	43
2.7	Bias network for the imaging detector with gated gain.	46
2.8	Photoelectron imaging of atomic O^- at 532 nm (2.33 eV).	49
2.9	Velocity distributions and photoelectron energy spectra for atomic O^- at 532 nm.	50
2.10	Photoelectron angular distributions (PADs) for atomic O^- at 532 nm. . .	53
2.11	Kinetic energy dependence of β : O^- image at 355 nm and its Cooper-Zare curve.	54
3.1	CO_2^- as a distonoid radical: spin density, atomic charges, and HOMO. . .	57
3.2	Potential energy curves for CO_2^- as a function of bending angle and basis sets.	63
3.3	Qualitative curves for CO_2^- showing the diffuse state and non-adiabatic couplings.	64
3.4	Mass spectrum of parent $(\text{CO}_2)_n^-$ clusters optimized for medium-range masses.	66
3.5	Photofragmentation of $(\text{CO}_2)_{16}^-$ with 355 nm light.	71
3.6	Photoelectron imaging of $(\text{CO}_2)_n^-$ clusters, $4 \leq n \leq 9$ at 400 nm	74
3.7	Energy dependence of the photoelectron anisotropy for representative monomer-based and dimer-based $(\text{CO}_2)_n^-$ cluster anions.	76
3.8	Optimized structures for the $(\text{CO}_2)_2^-$ dimer anion and its HOMO as a linear combination of monomer molecular orbitals.	80
3.9	Optimized structures for dimer-based structures of the $(\text{CO}_2)_3^-$ cluster anions	81
3.10	Optimized structures for dimer-based structures of the $(\text{CO}_2)_4^-$ cluster anions	82

LIST OF FIGURES – *Continued*

4.1	Mass spectrum of parent $\text{CO}_2^-(\text{H}_2\text{O})_m$ cluster anions.	90
4.2	355 nm photofragment mass spectrum for the $\text{CO}_2^-(\text{H}_2\text{O})_m$ cluster anions.	93
4.3	Branching ratio of the core-dissociation and water-evaporation fragments as a function of the parent $\text{CO}_2^-(\text{H}_2\text{O})_m$ cluster size.	94
5.1	Representative mass spectrum of parent $(\text{CO}_2)_2(\text{H}_2\text{O})_m^-$ cluster anions.	107
5.2	355 nm photoelectron images of $(\text{CO}_2)_2(\text{H}_2\text{O})_m^-$ cluster anions.	109
5.3	eBEmax values for photoelectron bands arising from the dimer-based and monomer-based $(\text{CO}_2)_2(\text{H}_2\text{O})_m^-$ clusters at 355 nm.	110
5.4	Photofragment mass spectra obtained from $(\text{CO}_2)_2(\text{H}_2\text{O})_m^-$, $m = 3-11$, cluster anions at 355 nm.	114
5.5	Probability for the nascent O^- fragment to undergo an intracuster ion-molecule association reaction with CO_2	124
6.1	Raw and Abel-inverted NO^- photoelectron images and the corresponding photoelectron energy spectra.	131
6.2	Experimental NO^- photoelectron spectra compared to its simulation.	132
6.3	Raw and Abel-inverted photoelectron images and corresponding photoelectron images and their corresponding spectra obtained at 355 nm for $\text{NO}^-(\text{N}_2\text{O})_n$, $n = 0-7$	134
6.4	Raw and Abel-inverted photoelectron images and corresponding photoelectron images and their corresponding spectra obtained at 355 nm for $\text{NO}^-(\text{H}_2\text{O})_n$, $n = 0-3$	135
6.5	N_2O^- photofragment resulting from the 532 nm dissociation of N_3O_2^- anion.	136
6.6	Qualitative potential energy curves for NO and NO^- and plausible autodetachment from the NO^- resonance.	139
6.7	Anisotropy parameter (β) values determined for NO^- photodetachment transitions at 786, 532, 355, and 266 nm along with the Cooper-Zare curve fit.	141
6.8	Photoelectron anisotropy parameters for $\text{NO}^-(\text{N}_2\text{O})_n$ and $\text{NO}^-(\text{H}_2\text{O})_n$ as a function of average eKE.	144
7.1	Representative mass spectrum displaying the $\text{CH}_3\text{SOCH}^-(\text{H}_2\text{O})_n$ anions.	154
7.2	Raw photoelectron images (left) and corresponding energy spectra for the CH_3SOCH^- and $\text{CH}_3\text{SOCH}^-\cdot\text{H}_2\text{O}$ anions.	156
7.3	Raw photoelectron image (left) and corresponding energy spectrum for the HCSO^- anion acquired at 355 nm.	157
7.4	532 nm photofragment mass spectrum of parent CH_3SOCH^- and $\text{CH}_3\text{SOCH}^-\cdot\text{H}_2\text{O}$ anions.	159

LIST OF FIGURES – *Continued*

7.5	Optimized minimal energy structures for $C_2H_4SO^-$ isomers obtained at the B3LYP/aug-cc-pVTZ level of theory.	161
7.6	(a) Mulliken spin densities and charges for CH_3SOCH^- obtained at the B3LYP/aug-cc-pVTZ level of theory; (b) spin density (α - β) contour plot showing the location of the unpaired electron; (c) HOMO; (d) HOMO-1. . .	162
7.7	Schematic picture of the states involved in photodetachment from the CH_3SOCH^- anion.	166
7.8	Schematic reaction coordinate calculated at the B3LYP/aug-cc-pVTZ. . . .	168
8.1	(a) raw photoelectron image of the $CH_3CN \cdot H_2O^-$ anion at 532 nm; (b) Abel-inverted reconstructed image; (c) photoelectron energy spectra; (d) PAD corresponding to $\beta = 0.95 \pm 0.1$	173
8.2	Mass spectrum of parent anions, displaying the formation of $HCCN^-$ and H_2CN^-	175
8.3	355nm photoelectron images (left) and energy spectra (right) of the $HCCN^-(H_2O)_n$, $n = 0 - 2$, Cluster Anions.	176
8.4	355nm photoelectron images (left) and energy spectra (right) of the $H_2CCN^-(CH_3CN)_n$, $n = 0 - 2$, Cluster Anions.	177

LIST OF TABLES

3.1	Vertical detachment energies and band widths for the photodetachment of $(\text{CO}_2)_n^-$ clusters.	75
5.1	Anionic photofragments of mass-selected $(\text{CO}_2)_2(\text{H}_2\text{O})_m^-$, $m = 3-11$ parent clusters observed at 355 nm.	115
7.1	Energies and VDEs for the optimized minimal energy structures of $\text{C}_2\text{H}_4\text{SO}^-$ obtained at the B3LYP/aug-cc-pVTZ level of theory.	161

ABSTRACT

Mass-selected cluster anions are employed as model micro-solutions to study solvent effects on the structural motifs and electronic structure of anionic solutes, including the roles of the solvent in controlling the outcomes of photochemical processes. Interaction of light with cluster anions can potentially lead to cluster photodissociation in addition to photodetachment. We investigate these competing processes by means of photoelectron imaging spectroscopy combined with tandem time-of-flight (TOF) mass spectrometry. Photoelectron images are reported for members of the $[(\text{CO}_2)_n(\text{H}_2\text{O})_m]^-$ cluster series. For homogeneous solvation, the photodetachment bands show evidence of cluster core switching between a CO_2^- monomer anion and a covalent $(\text{CO}_2)_2^-$ dimer anionic core, confirming previous observations. The Photoelectron Angular Distributions (PADs) of the monomer- and dimer-based clusters reveal an interference effect that result in similar PADs. Stabilization of the metastable CO_2^- anion by water solvent molecules is highlighted because its ability to "trap" the excess electron on CO_2 . Most surprising is the effect of the water solvent in quenching the autodetachment channel in excited states normally embedded in the electron detachment continuum, allowing excited $\text{CO}_2^-(\text{H}_2\text{O})_m$ clusters to follow reaction paths that lead to cluster fragmentation. Observed $\text{O}^-(\text{H}_2\text{O})_{m-k}$ photoproducts are attributed to photodissociation of the CO_2^- cluster core and are dominant for small parent clusters, whereas a water evaporation channel dominates for larger clusters. Addition of a second CO_2 to these clusters is shown

to preferentially form monomer based clusters, whose photodissociation exhibit an additional CO_3^- based channel, characteristic of a photoinitiated intracluster ion-molecule reaction between nascent O^- and the additional CO_2 solvent molecule. Changes in the PADs of NO^- are monitored as a function of electron kinetic energy for the $\text{NO}^-(\text{N}_2\text{O})_n$ and $\text{NO}^-(\text{H}_2\text{O})_n$ cluster anions. In contrast with hydration, angular distributions become progressively more isotropic for the N_2O case, particularly when the photoelectron kinetic energies are in the vicinity of the $^2\Pi$ shape resonance of the N_2O solvent molecules. First time observation of the CH_3SOCH^- anion of dimethylsulfoxide is reported along with the photoelectron images of this organic anion and of the monohydrated cluster. Observed photodissociation products are HCSO^- and SO^- .

CHAPTER 1

GENERAL INTRODUCTION

Among the most active research areas in the field of gas-phase chemical dynamics is the characterization of the structural and physical properties of isolated ions and molecules and their connections to chemical reactivity. These studies seek answers to the most fundamental questions about chemical bonding, elementary chemical reactions, and energy redistribution processes. The need for a microscopic understanding of solvation and the changes in structure and dynamics as the system progresses from the gas- to the condensed-phase has attracted the attention of many experimentalist and theorists. Ionic clusters present valuable tools for this purpose due to their ability to be mass-selected, providing therefore controlled environments where the solvent effects can be investigated in great detail.

In this dissertation, novel reactive pathways are reported for negatively charged cluster anions excited with photons in the ultraviolet and visible range. These experiments are carried out using a beam of mass-selected negative ions that is allowed to interact with short pulses of laser radiation. A new experimental apparatus was built to combine the capabilities of negative ion photoelectron imaging (developed previously in our laboratory and explained in detail by Surber [1]) with tandem mass spectrometry for the detection of ionic photofragments. The experimental observations afforded by this newly developed spectrometer provide two important pieces of information necessary to obtain a more complete picture of the photochemistry and dynamics of a wide range of atomic,

molecular, and cluster anions.

Of particular emphasis to this dissertation is the interactions and processes involving nascent photoproducts, namely photoelectrons and ionic photofragments. For instance, we have observed photoelectron-photoelectron wave interference, photoelectron-solvent molecule scattering, and photofragment-solvent molecule intracuster reactions. Additionally, we highlight the important role of solvation on the stabilization of metastable anions and the opening of “solvent-enabled” excited state dynamics, usually disfavored in the bare anion because of acute competition with electron detachment.

An introductory background and an overview of the body of work presented in this dissertation follows the rest of this Chapter. A description of the important processes and experimental techniques relevant to the experiments presented in subsequent chapters is provided below.

1.1 Anion photochemistry: Competitive pathways

When a molecular anion AB^- interacts with a photon, several processes may occur and in principle compete with each other, namely:



Process 1.1 is referred as direct photodetachment, and the resulting neutral could

either be on its ground or excited states. By energy conservation, the photodetached electrons are ejected with kinetic energies that reveal the discrete electronic and vibrational states of the remaining neutral (with very high resolution some rotational states may be determined as well). This technique is known as photoelectron spectroscopy.

If the photon interaction results in population of an excited state of the anion, processes 1.2–1.5 may occur. Autodetachment, or spontaneous electron emission, is illustrated in 1.2. It typically occurs when the potential energy curves of the neutral and the excited anionic state intersect (or if the neutral becomes more stable than the anion at a particular geometric arrangement). Anionic fragmentation, depicted in processes 1.3 and 1.4, usually results from a vertical transition to a repulsive excited state, a repulsive wall of an excited attractive state, or from a predissociation process—provided there is enough energy available. Our recently built experimental apparatus allow us to successfully characterize processes 1.1 to 1.4 by detecting both photoelectrons and ionic fragments. Dissociative photodetachment, described in 1.5, is often a consequence of neutral that is unstable after removal of the excess electron by the photon interaction. Coincidence techniques are typically used to characterize such processes (see for example the review by Continetti [2]). Radiative decay plays a minor role on the relaxation of excited anions.

1.2 Negatively Charged Clusters and Anion Solvation

Most of the anionic clusters studied in this dissertation are found to have the excess electron localized on an atomic or molecular moiety (cluster core) that is surrounded by the remaining neutral cluster components—considered as neutral solvents. One

exception is the dipole bound $[\text{CH}_3\text{CN}\cdot\text{H}_2\text{O}]^-$ anion discussed in Chapter 8. Because ionic clusters can be easily mass-selected [3], it is possible to create defined surrounding conditions where the exact number of solvent molecules around the ionic core can be determined. Clusters are therefore used as model “micro-solutions” that provide a simpler, well-defined, environment for the study of solvation effects at a molecular level [4, 3, 5]. Furthermore, step-wise solvation can be employed to study the progressive evolution in reactivity and to monitor any changes in the intrinsic properties of the core anion as a function of the number of solvent molecules (solvent domain). The process of ion solvation is of central importance to chemistry and therefore these studies provide great insights for the interrelation between the gas-phase observations with the ones in condensed environments.

The outcomes of chemical reactions are greatly influenced by the solvation effects that arise from the intermolecular interactions between the ionic solute and its local solvent environment. The presence of additional particles around the solute presents a limitation to its available physical space, posing physical barriers to the motion of the reactive species. In addition, the solvent acts as an energy bath, opening a pathway for internal relaxation of the solute and for the stabilization of energetic products formed during reactions. Yet, a less obvious effect of solvation is the perturbation caused to the electronic structure of the solute and to the potential energy curves that dictate the fate of particular chemical reactions.

In condensed-phase media, such as liquids or solids, due to the poorly defined local environments around the solute and the very large number of interactions involved, the effects of solvation are usually observed by monitoring macroscopic properties that are

statistical, rather than dynamical. Ionic clusters are especially appealing because their well-defined microscopic environments make possible the study solvation effects at a molecular level, providing detailed dynamical information about the solute-solvent and solute-solute interactions.

1.3 Photoelectron Imaging of Negative Ions

Photoelectron spectroscopy is a powerful tool for experimentally characterizing the electronic structure of many ions and molecules, since the obtained photoelectron spectrum provides a direct probe of the involved molecular orbitals. Three experimental observables result from a “complete” photoelectron spectroscopy experiment, namely: the photoelectron kinetic energy, the detachment cross-section, and the photoelectron angular distribution.

For negative ions, an energetic analysis of the photodetachment process is schematically shown in Figure 1.1. Important quantities are the adiabatic electron affinity (AEA), defined as the difference between the energy of neutral on its ground vibrational and electronic state and that of the anion. A positive value for the AEA is typically an indication of a stable anion. The vertical detachment energy (VDE) is nominally assigned to the peak with maximum intensity in the spectrum, corresponding to a vertical transition which provides the largest Franck-Condon overlap.

Absolute and relative cross sections obtained at different experimental conditions and photon energies can be used to characterize the nature of the observed photoelectron bands. The photoelectron angular distributions (PADs), often disregarded by photoelectron spectroscopist, are directly tied to the symmetry of the molecular orbitals

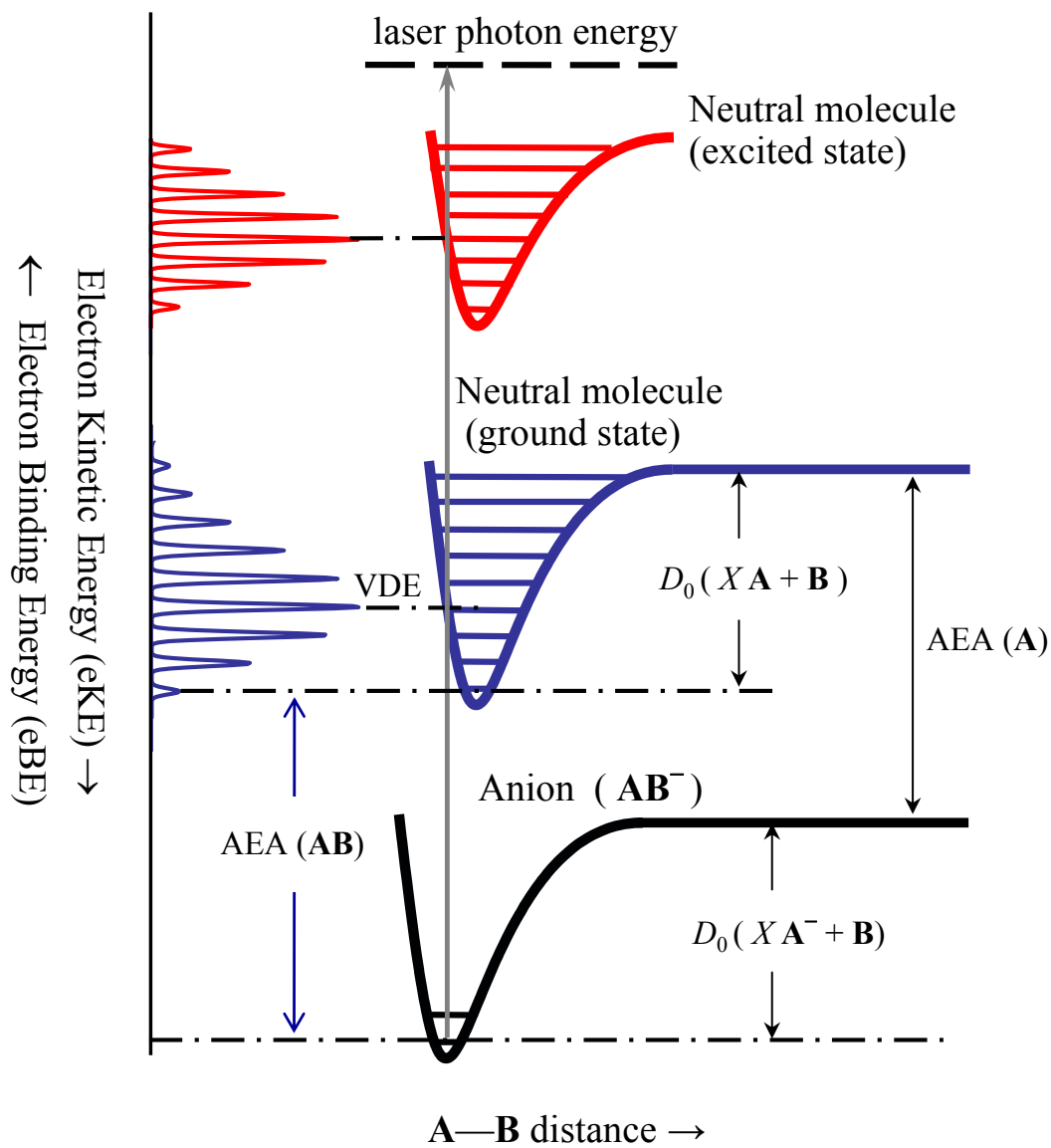


Figure 1.1: Schematic photoelectron energy diagram and anionic transitions.

involved. With the advancement of imaging techniques [6, 7] in recent years, as applied in particular to photoelectron imaging of negative ions [8, 9, 10], information contained in the angular distributions has been utilized to gain further understanding of the bound electron orbitals and subtle intermolecular interactions in ionic clusters, as well as providing a new perspective to time-resolved studies of anionic reactivity [10].

For a one-photon process involving linearly polarized light, the PADs are generally described by the Cooper-Zare equation [11, 12, 13]:

$$I(\theta) = a[1 + \beta P_2 \cos(\theta)] \quad (1.6)$$

where θ is the angle between the photoelectron velocity and the laser polarization vectors, $I(\theta)$ is the probability of electron emission at a particular angle θ , a is a normalization constant that is proportional to the total photodetachment cross-section, $P_2(\cos \theta)$ is the second-order Legendre polynomial, and β is the anisotropy parameter. The anisotropy parameter ranges from $\beta = -1$ for a purely perpendicular transition to $\beta = +2$ for a purely parallel transition. It can be seen from Equation 1.6 that this parameter fully characterizes a one-photon PAD and provides direct experimental evidence of the nature of the photodetachment process and the symmetry properties of the bound orbitals from which the photodetached electrons originate [10]. Simulated PADs using Equation 1.6 are visually displayed in Figure 1.2.

1.4 Anion Photodissociation: Where does the excess electron go?

A natural query that arises in dissociation studies involving singly charged anions concerns the localization of the excess charge on a particular fragment. Arguments based on the difference in the electron affinities of the departing fragments could be made.

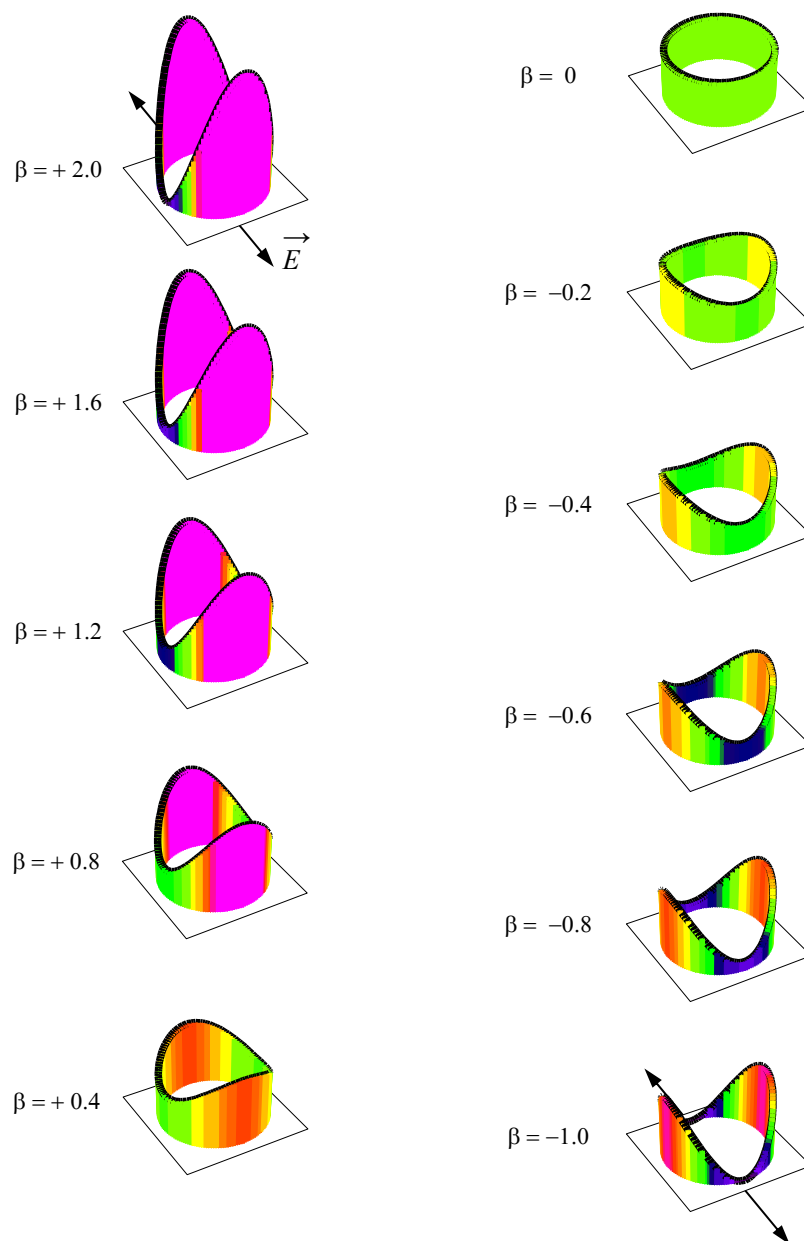


Figure 1.2: Simulated photoelectron angular distributions as a function of the anisotropy parameter β .

However, the identity of the ionic fragments is governed by the properties of the potential energy surfaces corresponding to the states being populated at a particular excitation energy. The observation of particular photoproducts can therefore be used to infer the nature of the excited states that are accessed with the energy provided by the photon. In the case of cluster anions, the solvent molecules may also compete for this additional electron, resulting in a charge-transfer-to-solvent (CTTS) process. Identifying the anionic fragments resulting from cluster photofragmentation, may also be used to characterize other important dynamic processes, such as caging and recombination and intracuster ion-molecule reactivity. This reasoning motivated the construction of a new experimental apparatus that, in addition to photoelectron imaging, could reveal the identity of the ionic fragments, if any, that are formed upon photoexcitation.

1.5 Overview of this Dissertation

The rest of this dissertation is divided into eight additional chapters. The experimental apparatus designed to perform the combined photoelectron imaging/photofragmentation experiments is described in Chapter 2. The studies conducted on the $[(\text{CO}_2)_n(\text{H}_2\text{O})_m]^-$ cluster series are presented in Chapters 3, 4, and 5. Results for the homogeneous $(\text{CO}_2)_n^-$ clusters are discussed in Chapter 3. Solvent-enabled photodissociation of the CO_2^- radical anion in water clusters is introduced in Chapter 4, and the interesting fragmentation channels resulting from the addition of a second CO_2 molecule to the $\text{CO}_2^-(\text{H}_2\text{O})_m$ clusters are presented in Chapter 5. The loss of photoelectron anisotropy by a solvent resonant electron scattering process on the photodetachment from the $\text{NO}^-(\text{N}_2\text{O})_n$ cluster anions is reported in Chapter 6. Finally, photoelectron imaging

and photodissociation studies of various deprotonated anions of dimethyl sulfoxide and acetonitrile are presented in Chapters 7 and 8, respectively.

Highlights of the work reported in Chapters 3–7 are published (or are manuscripts in preparation) according to the following publication list. I would like to express my sincere gratitude to all the co-authors of these publications for their valuable participation in the research process involved in these exciting findings.

Chapter 3

R. Mabbs, E. Surber, L. Velarde, and A. Sanov, *J. Chem. Phys.* **120**, 5148 (2004).

Chapter 4

T. Habteyes, L. Velarde, and A. Sanov, *Chem. Phys. Lett.* **424**, 268 (2006). T. Habteyes, L. Velarde, and A. Sanov, *J. Chem. Phys.* **26**, 154301 (2007).

Chapter 5

L. Velarde, T. Habteyes, and A. Sanov, *J. Chem. Phys.* **125**, 114303 (2006).

Chapter 6

L. Velarde, T. Habteyes, E. Grumbling, K. Pichugin, and A. Sanov, *J. Chem. Phys.* **127**, 084302 (2007)

Chapter 7

L. Velarde, T. Habteyes, R. Glass, and A. Sanov (to be submitted)

CHAPTER 2

EXPERIMENTAL METHODS

2.1 Overview

This chapter describes the design and implementation of the various components that comprise the experimental apparatus used to perform the experiments described in subsequent chapters. In general, it consists of a pulsed ion source and a linear time-of-flight mass spectrometer (TOF-MS) succeeded by a reflectron time-of-flight mass spectrometer (ReTOF-MS). The instrument design is based on the ion generation and tandem mass spectrometry (MS/MS) techniques pioneered by Lineberger and co-workers [3, 14]. A pulsed laser interacts with the ion beam at the spatial focus of the linear TOF. Timing of the laser firing is critical for the study ions with a particular mass-to-charge ratio (m/z). The interaction of a mass-selected, negatively charged, parent ion with a laser photon may induce photofragmentation or photodetachment. Nascent ionic fragments can be detected at the focal plane of the reflectron. A velocity-mapped imaging (VMI) assembly, mounted with its axis mutually perpendicular to the propagation direction the laser and ion beams, allows for the position sensitive detection of the detached photoelectrons.

The ion source, primary TOF, and imaging parts of this apparatus are similar to the group's first negative-ion machine described in detail elsewhere [1, 15]. In addition to the richness of the photoelectron imaging technique, detection of ionic photoproducts offers

further information about the structural subunits of the parent anion and the photoinitiated dynamics of a particular system. Some modifications were made to the imaging assembly in order to have the additional capability of imaging photoelectrons from the reflected, mass-selected, photofragments.

The overall experimental setup is shown schematically in Figure 2.1. Atomic, molecular, and/or cluster anions are generated in the source chamber. A pulsed supersonic free-jet expansion of the sample gas into the vacuum chamber is intersected perpendicularly by a continuous 1 keV electron beam whose current is being monitored using a Faraday cup. Negative ions are formed by secondary electron attachment to neutral species. The resulting anions are then pushed into a Wiley-McLaren type TOF-MS by a -1 kV pulse on the extraction plate. A secondary acceleration process brings the total kinetic energy to ~ 3 keV. The accelerated anions enter the ion optics section, where they are steered by a set electrostatic deflectors and spatially focused by an Einzel lens. A fast potential switch references the ion beam back to ground potential. Once in the detection/photolysis region, an in-line detector (D1) provides the time-of-flight resolved masses. Mass-selected negative ions are intersected by a linearly polarized laser beam. Resulting anionic photofragments are detected off-axis (D2) with appropriate reflectron settings. Photoelectrons are focused by a VMI stack into the imaging detector (D3) located in the direction perpendicular to both the ion and the laser beams. A CCD camera captures resulting images and the signal is transferred to a computer for multiple-shot counting and data analysis.

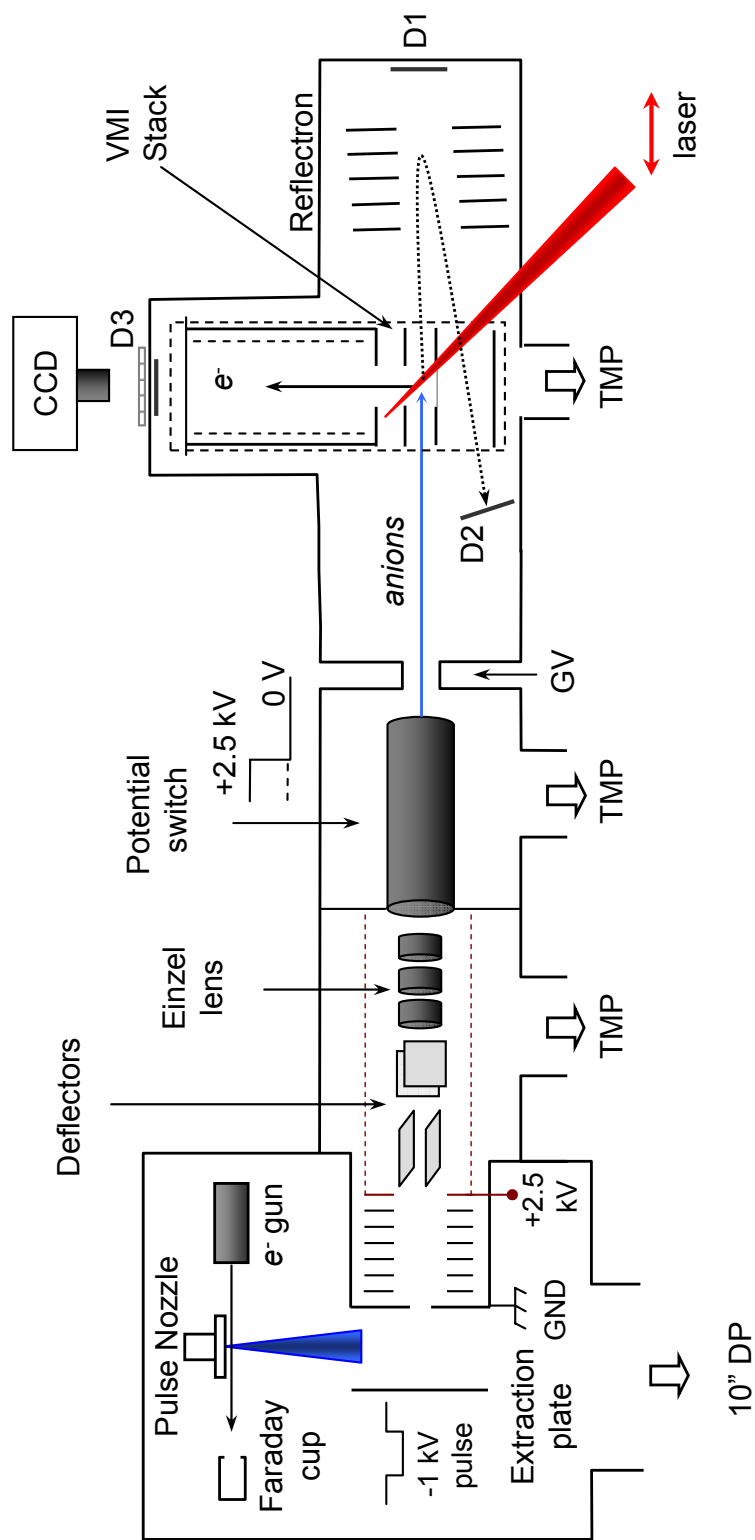


Figure 2.1: Schematic diagram of the experimental apparatus. DP: diffusion pump, TMP: turbo-molecular pump, D1: in-line ion/neutral detector, D2: off-axis ion detector, D3: photoelectron imaging detector. The double-headed arrow by the laser beam indicates the direction of the laser polarization.

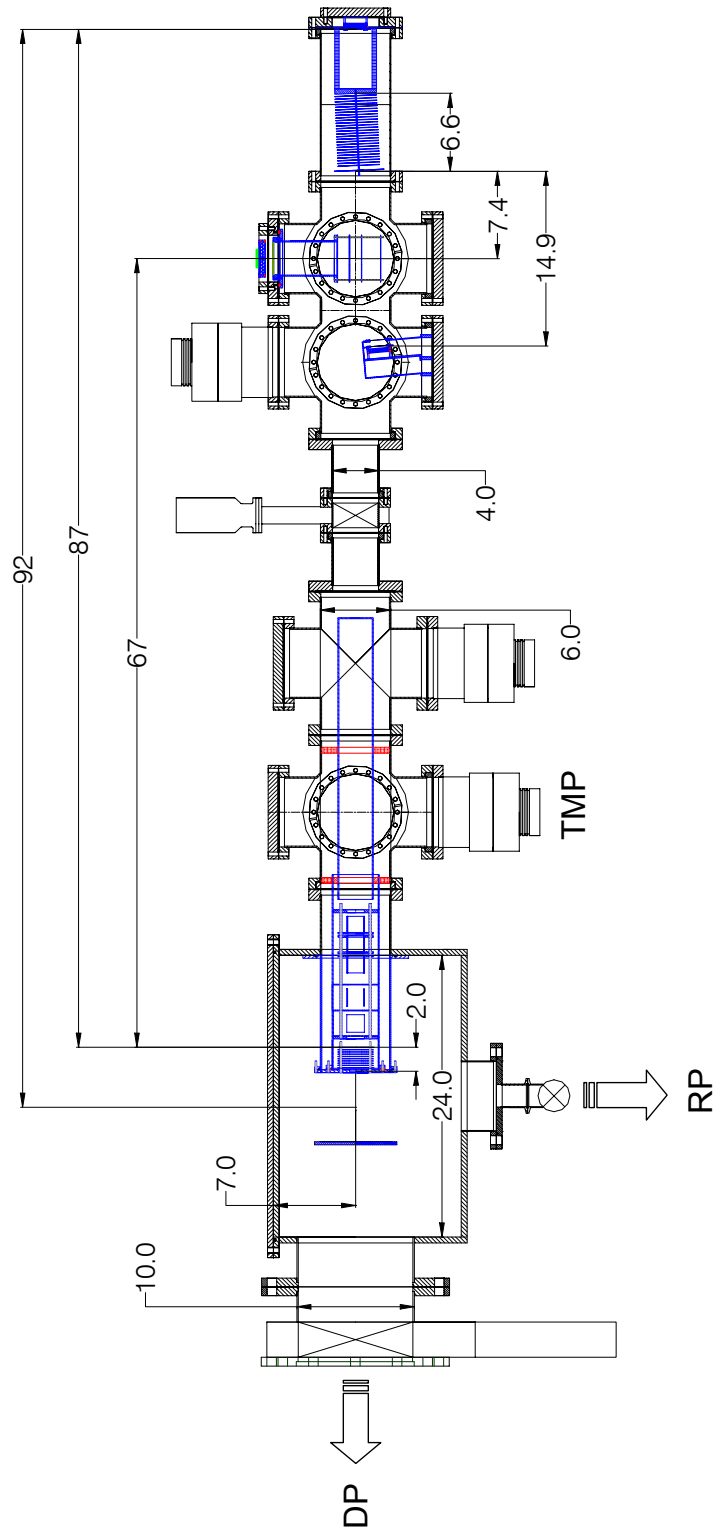


Figure 2.2: Detailed mechanical drawing of the apparatus (all dimensions are in inches). RP: rotary pump, DP: diffusion pump, TMP: turbo-molecular pump.

2.2 Vacuum Hardware

The system consists of three differentially pumped sections, namely: (i) the source chamber; (ii) the ion optics region; and (iii) the detection/photolysis chamber. All the main vacuum components are made of stainless steel (SS) and a detailed mechanical drawing of the complete apparatus is displayed in Figure 2.2. The custom-made source chamber has inner dimensions of 25"×24"×16" for length, width, and height respectively. The chamber is held under vacuum by a Varian VHS-10 diffusion pump (DP), with a nominal pumping speed of 5300 l/s for air. The DP is connected to the chamber by a 90° radius elbow located immediately after a pneumatic gate valve (Vacuum Research Ltd., 10" ASA flanges). High quality Santovac 5 pump oil is used for its low back-streaming rate properties. The DP is water-cooled and backed by an Edwards E2M40 rotary vane pump (30 cfm pumping speed).

Initially, a manual bellows valve (KF-50 flanges) is opened to bring the chamber to a rough vacuum (~ 30 mTorr) using the Edwards pump while the foreline backing the DP is closed by means of a pneumatic valve (KF-50 flanges). Once this is achieved, the roughing valve is closed, the foreline valve opened, and when the DP oil is sufficiently hot, the 10" gate valve is finally opened to achieve a $\sim 5 \times 10^{-7}$ Torr base pressure in the source chamber.

A 0.015" stainless sheet with a 4 mm orifice is centered and spot welded at the ground electrode of the acceleration stack. This aperture separates the source chamber from the rest of the instrument. In the ion optics region, two turbomolecular pumps –TMPs– (Leybold, model Turbovac 361) with a ~ 400 l/sec pumping speed bring this section to a base pressure of 5×10^{-8} Torr. The TMPs are connected by 8" CF flanges and backed (in

a parallel configuration) by a single rotary vane pump (Leybold, model Trivac B D16B) with a pumping speed of 13.4 cfm. The detection chamber is divided from the ion optics region by a pneumatic gate valve (6" CF flange, 4" opening). A couple of 8"-6" CF reducer nipples connect the gate valve in-line with the rest of the apparatus. A third TMP (Leybold, model Trivac B D16B) backed by a rotary vane pump (Leybold, model Trivac B D16B) is located at the detection region and brings the base pressure of this last section to $1-5 \times 10^{-9}$ Torr.

2.3 Ion Production

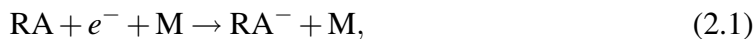
Supersonic expansion of the sample gas into vacuum is controlled by a pulsed nozzle valve (General Valve, Series 99) with a nozzle orifice of $\sim 800 \mu\text{m}$ and a conical half-angle of 45° . The valve is opened by lifting a spring-loaded poppet (Kel-F or PEEK) by means of the magnetic force of a solenoid. The firing of the nozzle is controlled by the IOTA ONE high speed valve driver (Parker Hannifin Corp., General Valve) externally triggered by a TTL pulse (T_0) from a delay generator (Stanford Research Systems, Inc., model DG535). An extra delay of 1–3 ms between the trigger pulse and the nozzle opening, set manually at the IOTA ONE driver, seems to increase the stability of the ion production signal. The valve is pulsed at 50 Hz and is opened only for about 150–250 μs of the total experimental period (200 ms), giving a duty cycle of $\sim 1\%$. The source chamber pressure is $1-5 \times 10^{-5}$ Torr when the nozzle is operating, while the pressure in the detection region raises to about 3×10^{-8} Torr.

About 5 mm away from the nozzle orifice, a 1 keV electron beam intersects the supersonic jet in a perpendicular arrangement. The electron beams ends in a Faraday

cup detector. The electron flux is measured by means of an ampmeter (Fluke Corp. multimeter, model 83 III) connected in series between the cup and the chamber walls, which are used as the common ground throughout the apparatus. The metallic body of the nozzle is also grounded to avoid charging in close proximity to the electron beam.

The electron gun (Southwest Vacuum Devices, Inc., model CE 3K/5U) produces a stream of high energy electrons by thermionic emission from a bent tungsten filament cathode. The filament is heated by passing a current of 3 to 3.5 Amps through it. The filament cathode and the control grid are floated¹ to -1 kV. The control grid, located a few millimeters away from the filament, is biased to ~ 80 – 170 Volts with respect to the cathode and has a small aperture where the electrons escape as they are accelerated to a ground cylindrical anode. This creates a 1 keV electron beam that is referenced to ground. A focus electrode set at about -1 keV is located between this anode and a collimating aperture—also at ground potential. Next, two sets of electrostatic deflector plates use $\pm(0$ – $60)$ Volts to steer the beam (vertically and horizontally) in order to maximize the overlap with the gas expansion. Only teflon coated wires and cables with crimped connections are used in the source chamber for their lower outgassing properties.

Anion formation [3] can occur via three-body stabilization



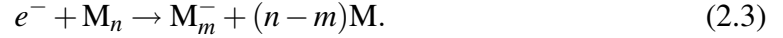
or by dissociative electron attachment



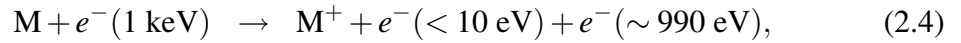
Klots and Compton [16] proposed a mechanism for the formation of anionic clusters that can be considered as a combination of mechanisms 2.1 and 2.2 called “evaporative

¹All floated power supplies are held inside a plexiglass box to avoid electric shock.

attachment". In this process the third body in 2.1 is actually a component of the cluster, and it can be represented as



If an electron is trapped by an anionic resonance [17] of a single monomer M, the temporary anion state $[M^{-}]^*$ can be stabilized by collisions with constituents already attached to the cluster. The excess energy necessary for this stabilization is then taken away by ejection of neutral monomers. These kind of resonant processes generally happen at low electron energies. Therefore, the formation mechanism by high energy (~ 1 keV) electron impact must involve the secondary electrons formed by ionization of the neutral species



Since the supersonic jet is observed to be an electrically neutral plasma, the high energy electron must scatter out of the jet while the low energy electron cools in the expansion through inelastic events [3]. The ion density in the plasma is approximately 10^9 cm^{-3} [3, 18]. The plasma remains collisionally coupled to the free-jet expansion allowing for long drift distances without significant ion loss. These long drift lengths between the expansion and the extraction are important for reactive formation of other anionic species by allowing for low energy ion-neutral collision [18].

2.4 Linear Time-of-Flight Mass Spectrometer

The expanding jet is directed between two parallel plates, namely the extraction plate and the ground electrode of an acceleration stack. About 18 cm downstream from the nozzle, the anions are extracted from the plasma into a Wiley-McLaren type TOF-MS by means of a pulsed transverse electric field between the extraction plate and the ground electrode, which are separated by approximately 15 cm. The potential on the extraction plate is driven by a pulse generator module (Directed Energy Inc., model PVM-4210) with a fast rise/fall time (<20 ns) designed for capacitive loads. Triggering occurs on the leading edge of a TTL pulse from the Stanford DG535 delay generator (channel C). The duration of the extraction voltage is determined by the positive slope of a second TTL pulse (channel D). In practice, the TTL output from the CD channel of the Stanford delay generator is sent to the gate input of the PVM-4210 pulser, while an adjustable potentiometer controls the output voltage applied to the extraction plate (0 to -950 Volts). Because the expansion crosses through the middle of this extracting field, the first acceleration stage provides the ion beam around 0.5 keV of initial kinetic energy in the direction of the TOF-MS. A 4 mm diameter aperture, placed at this ground electrode plate, separates the source chamber from the rest of the machine while letting a cylindrical volume of anions pass through the small opening.

The extracted anions enter a second acceleration region where a uniform electric field is supplied by an acceleration stack consisting of 10 circular electrodes, 1/32" thick, 3.0" OD, with a 1" diameter opening. The plates are separated by 0.160" teflon spacers (Fluoro-Plastics, Inc.) and electrically connected by 1 M Ω laser-spiraled high precision resistors. The plate farthest from the source chamber is connected to a high-voltage

power supply (Bertan, Inc.) set to ~ 2.5 kV that is also used to float the consecutive ion optics. All electrical connections from this section on use only Kapton insulated high-vacuum wire. The acceleration stage provides the ions and additional 2.5 keV of kinetic energy, making the total kinetic energy of the ions $\sim 3000 \pm 200$ eV. The spread in energy distribution originates from the spatial distribution of the gas expansion [19]. The field-free region from the end of the acceleration stack is ~ 1.7 m to the laser interaction and ~ 2.2 m to the end of the flight-tube (see Figure 2.2). The location of the Wiley-McLaren space focus is fine-tuned by making small adjustments to the voltages on the extraction plate and on the secondary acceleration stage.

A set of deflectors (horizontal and vertical) provide $\pm(0-100)$ Volts additional to the float potential to steer the ion beam. A three element Einzel lens is responsible for the transverse spatial focusing of the ion beam at the longitudinal focus given by the Wiley-McLaren conditions. Each component of the lens is a 1.5" OD SS cylinder, 1.5" long, separated from each other by 0.160" teflon spacers. The middle electrode is set to a decelerating +1 kV, while the outer ones are at the float voltage (+2.5 kV).

At the output of the Einzel lens the ions are referenced back to the ground potential without affecting their kinetic energy by means of a fast potential switch as described by Johnson and co-workers [20]. The potential switch is a thin 3" OD stainless steel tube, 24" long, with a 3/4" aperture at the exit (knife edge on the direction of the incoming beam). It is operated by a high-voltage pulse generator (Directed Energy, Inc., model PVM-4140) synchronized with the extraction plate; i.e., it is only energized to the float voltage (+2.5 kV) for the duration of the CD pulse from the Stanford DG535. The ions enter the tube when the switch is at the beam potential then, at the trailing edge of the CD

pulse, the switch potential rapidly drops to ground while the ions are still inside the tube. This potential switch also serves as a mass gate to avoid detection of unwanted species, making it a good tool to eliminate detection of undesirable ions that might saturate the detector.

The ions are detected at the end of the ~ 2.3 m long flight tube (see Figure 2.2) by a 25 mm diameter chevron-configured dual microchannel plate (MCP) detector with a metal anode (Burle, Inc.). A bias of about +1 keV at the front end of the MCP post-accelerates the ions before impacting the detector. A 70 wpi (wires-per-inch) mesh (Precision Eforming, LLC., 90% max. transmission), connected to ground potential, is placed prior to the MCP to provide an homogeneous post-accelerating zone and also to isolate this field from the rest of the flight tube. The signal from the detector anode is capacitively coupled before the resulting ac signal is sent to a 100X (100MHz) preamplifier (Phillips Scientific, model 6931). The coupling RC circuit that provides the bias network to the MCP and ac couples the ion signal is shown in Figure 2.3.

The amplified spectral signal is then recorded and averaged by a 300 MHz digitizing oscilloscope (Tektronix Inc., model TDS3032). The averaged spectra is then transferred to a computer through a GPIB interface (National Instruments, Inc.) and the Wavestar software (Tektronix, Inc.).

To convert the acquired spectra from the time-of-flight to the mass scale, the empirical equation [21]:

$$t = a \left(\frac{m}{z} \right)^{1/2} + t_0 \quad (2.6)$$

is used, where t is the time-of-flight for the ion with mass-to-charge m/z . By making an “educated guess” of the m/z assignment for two peaks, m_1/z and m_2/z , together with

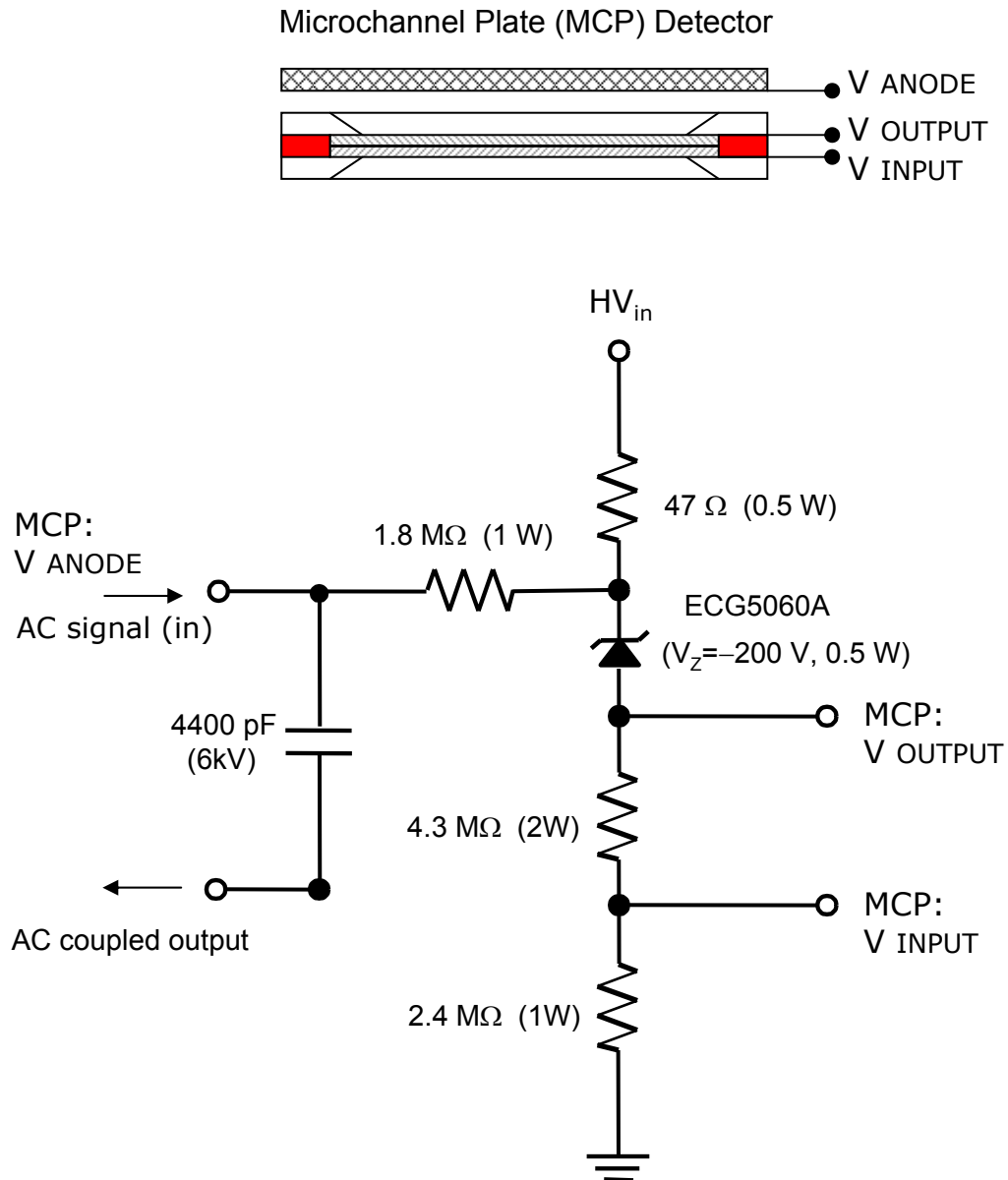


Figure 2.3: Bias network for the ion MCP detector. The Zener diode provides a regulated 200 V voltage drop between the anode and V_{OUTPUT} . The voltage divider gives 35.8% of HV_{in} at V_{INPUT} . The 4400 pF capacitance is given by two 2200 pF capacitors in parallel and blocks the HV dc component of the anode while it allows the ac signal to pass to the preamplifier. Under typical operating conditions $V_{ANODE} \simeq HV_{in} = 2.6 \text{ kV}$, $V_{OUTPUT} = 2.4 \text{ kV}$, and $V_{INPUT} = 0.93 \text{ V}$.

their corresponding measured times-of-flight, t_1 and t_2 , a system of two equations and two unknowns is created that allows us to solve for the constants a and t_0 in equation 2.6 and therefore to determine the rest of the unknown masses. Our criterion for a good calibration is that t_0 should be as close to zero as possible and a typically ranges from 2 to 3 $(\mu\text{s})^{-2}$ for our current setup. The first mass spectra obtained with this machine is shown in Figure 2.4 with the nozzle backed by the lab's air at ~ 1 atm.

2.5 Laser Interaction and Mass Selection

An Nd:YAG laser system (Spectra-Physics, model Quanta-Ray Lab 130-50) is used for most of our experiments. It provides ~ 8 ns pulses at 1064 nm with a 50 Hz repetition rate. The laser is equipped with the necessary crystals (KTP) for second, third, and fourth harmonic generation. Maximum laser power available are approximately 320, 120, 50, and 15 mJ/pulse for the 1064 nm, 532 nm, 355 nm, and 266 nm outputs respectively. Only about 30–60% of the maximum power is used for a typical experiment.

The laser beam travels in the same horizontal plane of the ion beam, intersecting in a perpendicular arrangement at the focal point of the TOF-MS. The laser is linearly polarized in the direction of the ion beam propagation. It enters and exits the apparatus, p -polarized, through a couple of fused silica windows placed at Brewster's angle (55.5°). This minimizes reflection losses at the air/glass interfaces. The beam is focused by a fused silica lens with a focal length of 2 m. The waist of the focused beam falls inside a 90° bent cooper tube located after the exit window. This tube serves as a beam dump to the high power laser. At the laser-ion interaction region, we estimate the laser beam diameter to be ~ 5 mm, providing a 100% overlap with the focused ion beam. A series of apertures

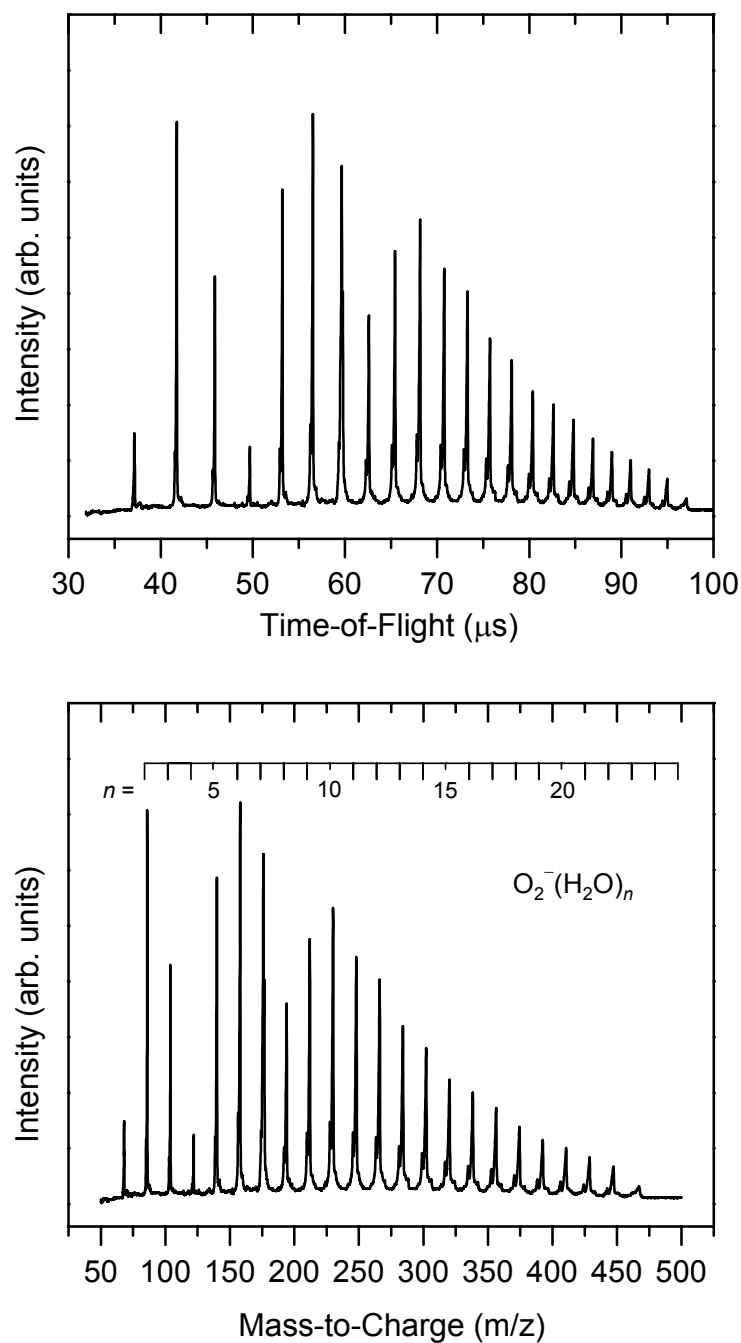


Figure 2.4: Mass spectra of $\text{O}_2^-(\text{H}_2\text{O})_n$ cluster anions by expansion of 1 atm of air. (a): time-of-flight spectra as recorded by the oscilloscope. (b): conversion to m/z and peak assignment. Notice the square root relation of the time-of-flight scale with the m/z scale.

(baffles) are placed inside the 1" SS tubes connecting the windows to the chamber. Their purpose is to minimize scattered light that may release photoelectrons from the metallic walls of the chamber. This is particularly important for high photon energies that may overcome the work function of the metal.

The timing of the laser is controlled by the Stanford delay generator for low jitter performance. Channel A gives the TTL pulse that controls the powering of the flash lamps and channel B controls the firing of the laser by means of a Q-Switch. Typically, the lamps are powered about 195 μs before the Q-Switch opens. This delay is fine tuned to achieve maximum laser power. With this delay fixed, the timing of the Q-Switch opening (channel B) is then scanned to overlap in time with only the selected ion (mass-selection). For anions with $m/z = 10\text{--}200$, this overlap typically happens about 5–10 μs before the ions strike the MCP detector located at the end of the flight tube, with the longer times corresponding the heavier/slower ions.

A good overlap between the laser pulse and the anion packet is tested by maximizing the neutral signal at the in-line MCP. The neutrals are observed by applying a voltage to the reflectron big enough to deflect all charged species. If no neutrals are observed for a particular wavelength, the reduction on the parent ion signal is also a good, but less sensitive, indicator.

2.6 Reflectron Time-of-Flight Mass Spectrometer

Mass analysis of the anionic fragments is achieved by a single-stage linear field reflectron mass spectrometer [22, 18]. The reflectron assembly is tilted 2.5° , altering the trajectory of the reflected ions by 175° to the direction of the primary ion beam. Since the incoming

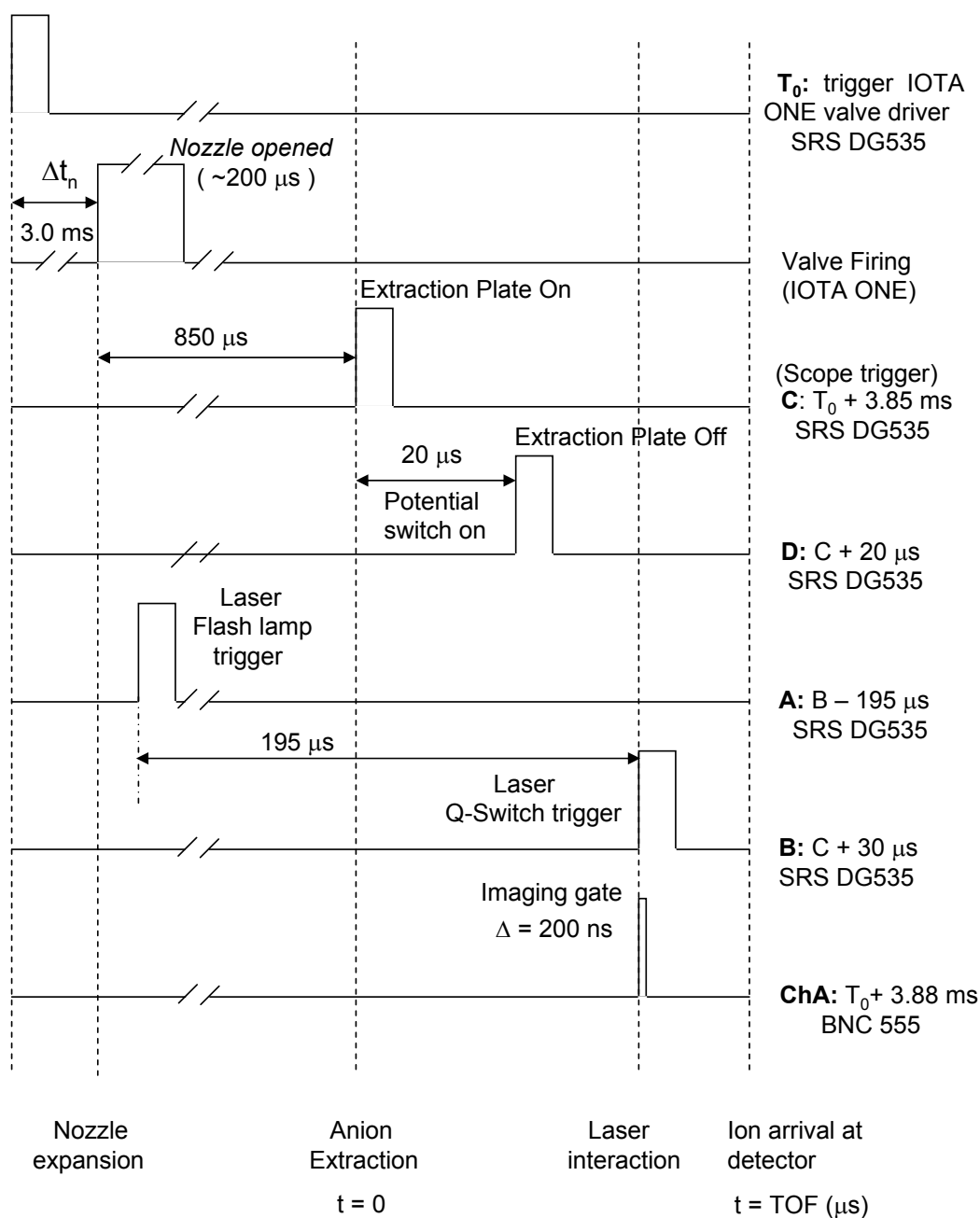


Figure 2.5: Event timing sequence for a nanosecond laser experiment. Only the leading edge of the pulses are used for timing purposes. Values are representative of the delays used on a typical experiment. The 3 ms delay between T_0 and the nozzle firing Δt_n is optional.

ions are referenced to ground potential, the reversing field begins with a ground electrode (4.173" OD, 1/32" thick SS) that has a 0.315" diameter aperture for the ions entering the reflectron. After a 0.6" separation, it is followed by 26 SS circular electrodes (3.15" OD, 1/32" thick) with a 2.025" diameter opening. The plates are separated by alumina spacers (OrThec Ceramics, Inc.) that are 0.197" (± 0.001) thick, bringing the total length of the reflectron to 6.609". All plates are electrically connected by 1.0 M Ω high precision ($\pm 0.1\%$) metal film resistors. The rear plate is connected to a high-voltage power supply (Bertan, Inc., +5 kV max.) that establishes the reflectron voltage (V_r) necessary for the ions of interest to be reflected at 50–90% of the total reflectron depth. An exit slit 3/4" long, 0.315" wide, is placed at the front plate of the reflectron.

The ions are detected by an off-axis chevron-type dual MCP (Burle, Inc.). A post-acceleration voltage of +1 kV is established between the front of the MCP and a grounded mesh as explained for the in-line detector in Section 2.4. The position of the off-axis MCP is about 15" away from the reflectron entrance and it is mounted on a SS mounting wedge at 95°. The detector is encapsulated by a thin SS box that shields the primary ion beam from the detector voltages. The box is also tilted 95° and has a 1.38" diameter opening for the MCP detector. A grid (5 wpi, InterNet, Inc.) is placed at this opening and a +20 Volts bias is applied to discriminate against low energy electrons. The capacitively coupled ac signal is preamplified by a 100X (100 MHz) bipolar amplifier (Phillips Scientific Inc., model 6931), averaged for 512 experimental cycles by the digitizing oscilloscope, and transferred to a computer for data analysis. In general, the signal with the laser blocked is subtracted from the laser on signal to ensure that the detected fragment originates only from the laser-ion interaction.

In the linear potential created inside the reflectron, the ions follow parabolic trajectories where the turning point is determined by the mass of the ion, its kinetic energy, and the reflectron potential. Anions of the same mass but with different energies (beam energy spread) are refocused at the off axis detector by means of the deeper penetration for the more energetic anions, who eventually catch up with the less energetic ones at the reflectron focal plane. Ions with different masses follow different trajectories (penetration depths), and therefore have different arrival times at the detector, with the lighter ions arriving first. The energy spread for each mass is also compensated as described above. Trajectories for the flight of the ions in the reflectron were performed using the SIMION program (Scientific Instrument Services, Inc.) to help on the design of the overall reflectron assembly.

In a typical fragmentation experiment, the parent anions are refocused on the off-axis detector first and the signal is optimized by varying the applied reflectron potential. Once this is achieved, this optimum voltage setting for the parent ions is recorded as V_p as well as its arrival time t_p . Then the reflectron strength is reduced to

$$V_f = V_p \left(\frac{m_f}{m_p} \right), \quad (2.7)$$

so that fragment ions of mass m_f can be focused on the off-axis detector. This is based on the fact that the kinetic energy of the fragment is simply a (m_f/m_p) fraction of the parent kinetic energy. Fragment ions under this focusing condition spend exactly the same time in transit to the detector as their parents did, arriving at the recorded time t_p . They also follow the exact same trajectories of the parents, striking the detector in the same area and eliminating any spatially-dependent detection efficiency [18]. By scanning the reflectron potential we can find, and record, all possible photofragments. This scanning method

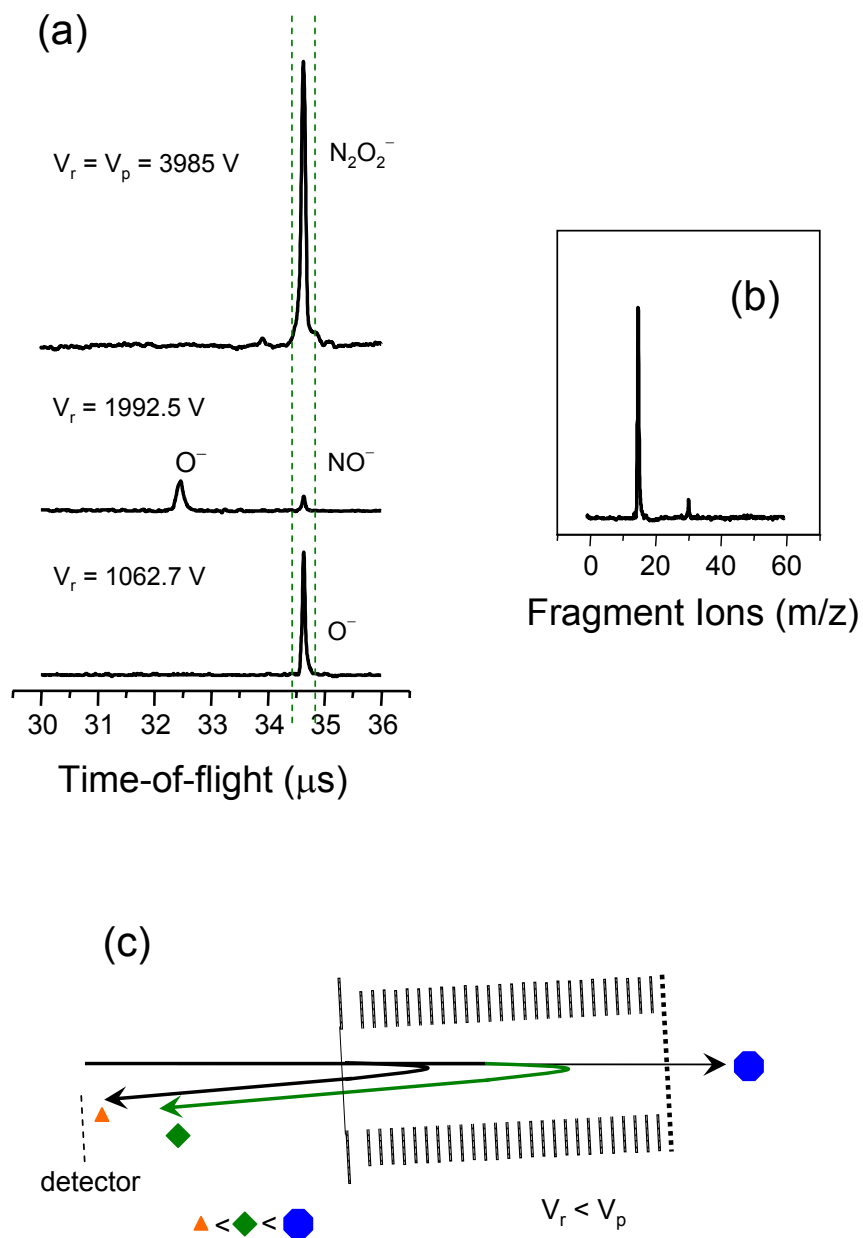


Figure 2.6: Photofragment acquisition for N_2O_2^- at 532 nm. (a): in the scanning mode, the reflectron voltage (V_r) is varied to record the fragments arriving the time window of the optimum parent settings. (b): compiled photofragment spectra. (c) schematic representation of the reflectron operation in the scanning mode with trajectories optimized for the middle-sized ions.

[23, 18, 14], unfortunately precludes simultaneous detection of all fragments. However, it provides unambiguous identification of the photofragment mass and excellent conditions for comparing relative photofragmentation yields. This procedure is illustrated in Figure 2.6.

2.7 Photoelectron Imaging

The velocity-mapped [24] imaging [6, 7] assembly consists of four OFHC (oxygen-free high conductivity) copper plates, 1/32" thick, with a 1" diameter opening. They are vertically stacked by means of #0-80 molybdenum threaded rods and nuts. Alumina spacers and washers (Kimball Physics, Inc.) isolate the plates from the metallic rods. These materials are chosen because of their high work function (~ 4.7 eV) that reduce unwanted photoelectrons originated from stray laser light hitting the surrounding metal surfaces. The first three plates (from the top down) are similar to the setup described in detail by Surber [1] with a 1" spacing between them. The ion and laser beams travel between the second and third plates. The bottom electrode is 1.6" apart and is added to image photoelectrons detached from reflected, mass-selected, photofragments by using a second laser. The potential of this new experimental methodology is described in detail in Chapter 9.

Under imaging conditions for photoelectrons originating from the parent anions, the top plate is in electrical contact with the floated electron flight tube and it is held at positive bias (typically 300–1000 Volts). The next electrode down is at ground and in contact with the mounting rods. The third plate is set at a repulsive negative potential (100–350 Volts) to extract the photoelectrons into the ~ 15.5 cm long field-free time-of-flight tube. The

last plate (for fragment photoelectron imaging) is not used and kept at ground potential. The ratio of the positive to negative voltages is kept constant. An empirical value between 2.2–2.6 is found to give the best focusing conditions. Larger voltages give shorter electron flight times and therefore more compact images. Screening of external magnetic fields that can alter the electron trajectories is essential, therefore a μ -metal shield surrounds the entire imaging assembly.

The electrons are detected by a 40 mm position sensitive detector mounted on a 6" CF flange. This imaging detector consists of a dual chevron-type MCP detector with a P43 phosphor screen anode coupled to a fiber optic vacuum window (Burle, Inc.). A post-acceleration stage before the electrons impinge on the detector is established by applying a +2 kV potential to the first MCP surface. To discriminate against noise, the second MCP is kept at a low gain mode with only a +3 kV bias. A timed +1 kV pulse (Directed Energy Inc, model PVM-4150) is superposed to this dc voltage, bringing the potential difference across the two imaging MCPs to a total of ~ 2 kV that efficiently amplifies the photoelectron signal only for a 200 ns window timed around the laser firing (see Figure 2.5). The RC circuit that controls the applied potentials is shown in Figure 2.7. The P43 phosphor anode is constantly kept at +6.5 kV. A fine electroformed nickel mesh of 333 wpi (Precision Eforming, LLC., 70% max. transmission) is located in the flight tube ~ 0.65 " prior to the first MCP of the detector. This mesh shields the detector voltages from the rest of the field-free region so that the flight of the photoelectrons remains unaffected.

The photoelectron images are acquired by a 1 Megapixel CCD camera (DALSA, Inc., model Pantera TF 1M30) equipped with a 12×12 mm, 1024×1024 pixels, CCD chip that

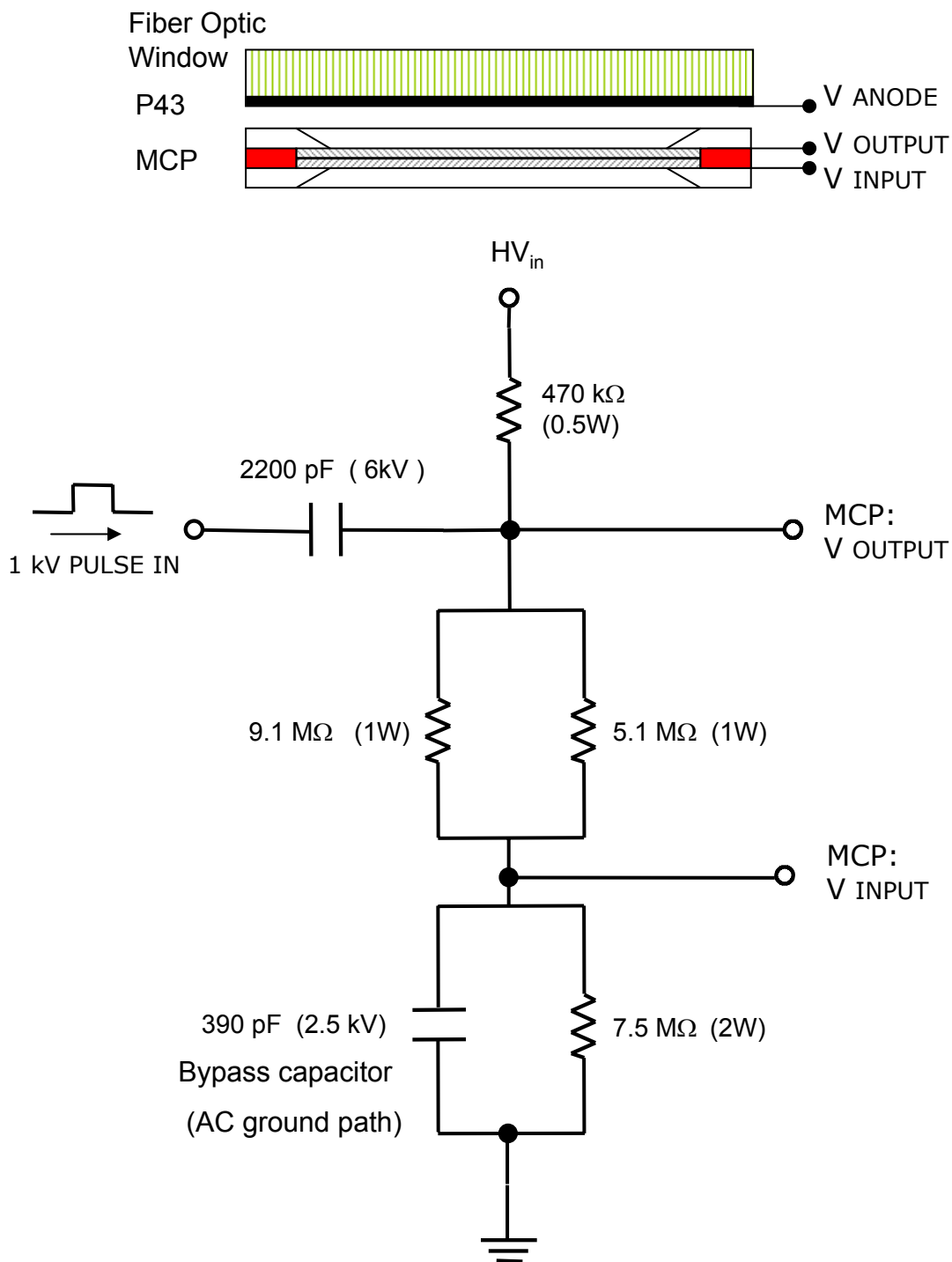


Figure 2.7: Bias network for the imaging detector with gated gain. The voltage divider gives 69.6% of the dc component of V_{OUTPUT} at V_{INPUT} . Typical values are $V_{\text{ANODE}} = 6.5 \text{ kV}$, $V_{\text{OUTPUT}} = 3 \text{ kV} + 1 \text{ kV (pulsed)}$, and $V_{\text{INPUT}} = 2 \text{ kV}$.

is capable of a 30 fps speed (without binning). A fast ($f/1.4$) 1" CCTV lens (Fujinon, Inc.) of 25 mm focal length, collects the image from the fiber optic window and the phosphor screen into the CCD. A PIXCI CL1 frame grabber (EPIX, Inc.) connected via CameraLink interface (National Semiconductor Corp.), transfers the image into a computer. The XCAP program (EPIX, Inc.) sets the contrast, gain, and repetition rate for the camera. This information is saved in a setup file named "setup.fmt". A modified version of the DAQ46 acquisition program developed by the Neumark group [25] reads the setup file, gathers and process each frame, and accumulates the signal of about $1-5 \times 10^4$ experimental cycles in an event-counted mode. A threshold intensity value is manually entered to discriminate against background noise². For most of the experiments, a 5 Hz acquisition rate is used, and the CCD collects for ~ 200 ms, storing photoelectron signals from about ~ 10 laser shots (maximum) per frame.

The photoelectron images are analyzed by using the Basis Set EXpansion (BASEX) program developed by Driblinski, Reisler, and co-workers [26]. Basically, this is an inversion algorithm that makes use of the cylindrical symmetry of the images (with respect with the laser polarization) to expand the experimental 2D data over a basis set of analytical Abel-transformed functions. The expansion coefficients are then used to reconstruct the original 3D velocity distribution. Photodetachment from the well-characterized O^- atomic anion served as a test and calibration system for this new imaging spectrometer. The photoelectron imaging process for this atomic system is demonstrated in Figure 2.8 for detachment with 532 nm light.

The main BASEX-inverted output includes a two column (radius, intensity) data file

²A threshold value too high may affect the measured anisotropy.

that is integrated over angle and an optional file in polar coordinates (radius, angle, intensity) where the angle is defined with respect to the laser polarization axis. Since the imaging experiments provide a map of the free electron velocity (or linear momentum), the obtained radial coordinate R can be thought of as the electron velocity in pixel scale, where the intensities provide the electron velocity distribution $P(v)$.

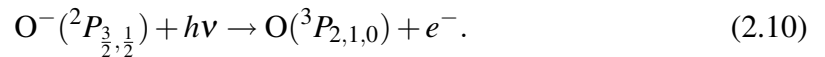
Since the electron kinetic energy (eKE) scales as the square of velocity, we use the following relation to convert from the velocity to the energy domain:

$$\frac{(eKE)_c}{v_c^2(\text{pixels})} = \frac{(eKE)_i}{v_i^2(\text{pixels})}, \quad (2.8)$$

where the $(eKE)_c$ (generally $(eKE)_c = h\nu - EA$) is the calibration value given to the corresponding $v_c(\text{pixels})$. The i th electron kinetic energy value $(eKE)_i$ is then calculated for each $v_i(\text{pixels})$ given by the BASEX output file. The velocity distribution $P(v)$ is converted into the energy spectrum $P(eKE)$ by means of the $P(v)dv = P(eKE)d(eKE)$ equality. Thus,

$$P(eKE) = P(v) \frac{dv}{d(eKE)} \quad (2.9)$$

the $dv/d(eKE) \propto 1/v$ Jacobian is therefore necessary to transform from the velocity to the energy space. The photoelectron velocity distributions and energy spectra are shown in Figure 2.9 for the O^- image displayed in Figure 2.8. The ring corresponds to the six unresolved fine-structure transitions



The angular distributions (PADs) are obtained by integrating over the radial direction for a particular angle. Integration is performed successively in 0.5° increments. The radial integration limits are usually determined by the FWHM of a particular peak.

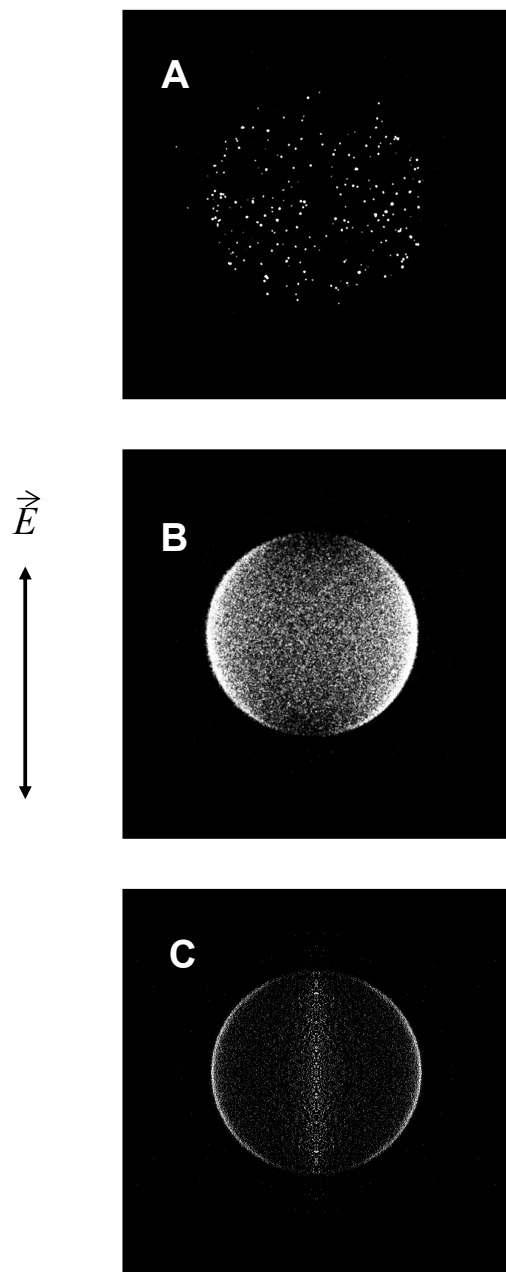


Figure 2.8: Photoelectron imaging of atomic O^- at 532 nm. (A): raw image after 9 laser shots. (B): after 15000 shots. (C): Abel-inverted image.

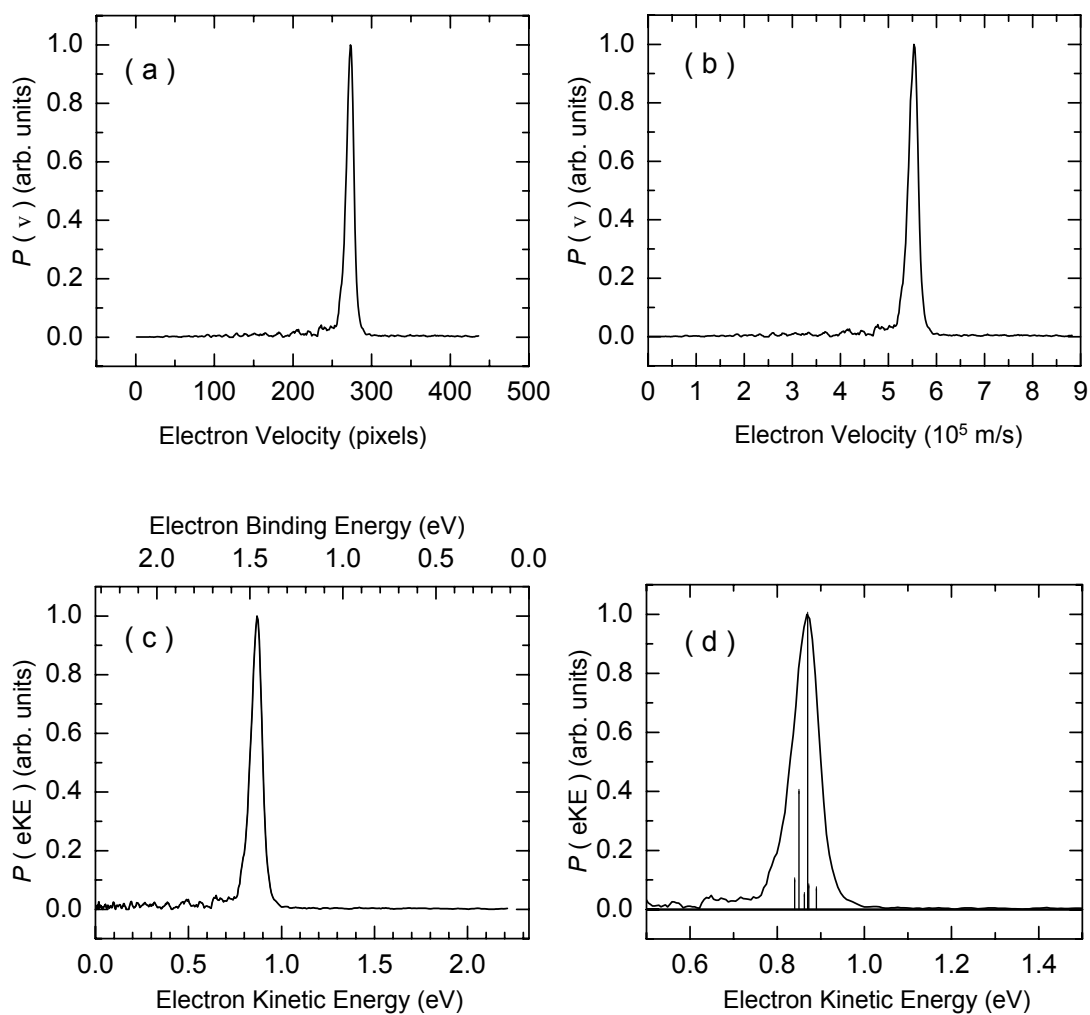


Figure 2.9: Velocity distributions (a),(b) and photoelectron energy spectra (c),(d) for atomic O^- at 532 nm. A stick plot of the unresolved spin-orbit transitions (see [27]) is shown in (d).

The integrated values for each angle θ are plotted, and the experimental anisotropy parameter β is obtained by a least-squares best fit to the Cooper-Zare model [12, 13] in the form

$$I(\theta) = a[1 + \beta P_2 \cos(\theta)], \quad (2.11)$$

where a is a constant proportional to the detachment cross-section, $I(\theta)$ is the probability of electron emission at an angle θ (see Mabbs and Sanov [10]), $P_2 \cos(\theta)$ is the second-order Legendre polynomial, and β is the anisotropy parameter. For a pure parallel transition $\beta = 2$ corresponding to a $\cos^2(\theta)$ distribution, and for a perpendicular transition $\beta = -1$ corresponding to a $\sin^2(\theta)$ distribution. The PADs for the O^- image in Figure 2.8 are displayed in Figure 2.10. Our obtained value of $\beta = -0.89 \pm 0.06$ for the fine-structure averaged anisotropy parameter compares quite well with the recently determined value of -0.89 ± 0.01 at 532 nm [27]. The perpendicular nature of the PADs for this atomic anion was first observed by Hall and Siegel [28] and is attributed to an interference effect of the $\ell' = \ell \pm 1$ photoelectron partial waves as predicted by Cooper and Zare [12].

Since the anisotropy parameter is strongly dependent on the photoelectron kinetic energy [12, 13], it is often necessary to image a particular system at a variety of laser wavelengths. Figure 2.11 (a) and (b) shown the raw and Abel-inverted images for photodetachment of O^- at 355 nm. Besides the inner ring, corresponding to the now accessible 1D state of the neutral, noticeable changes occur to the angular distributions in the image compared to the one at 532 nm shown in Figure 2.8. The measured anisotropy parameters $\beta(\text{eKE})$ are plotted in Figure 2.11(c) together with a set of Cooper-Zare functions reported on the literature [29, 27]. Another interesting feature

is that photoelectrons with low kinetic energy give more symmetric PADs. Wigner [30] recognized that near the detachment threshold, the cross section is proportional to $(eKE)^{\ell+\frac{1}{2}}$, predicting therefore that s partial waves will dominate the detachment process for low eKEs, thus giving more isotropic PADs.

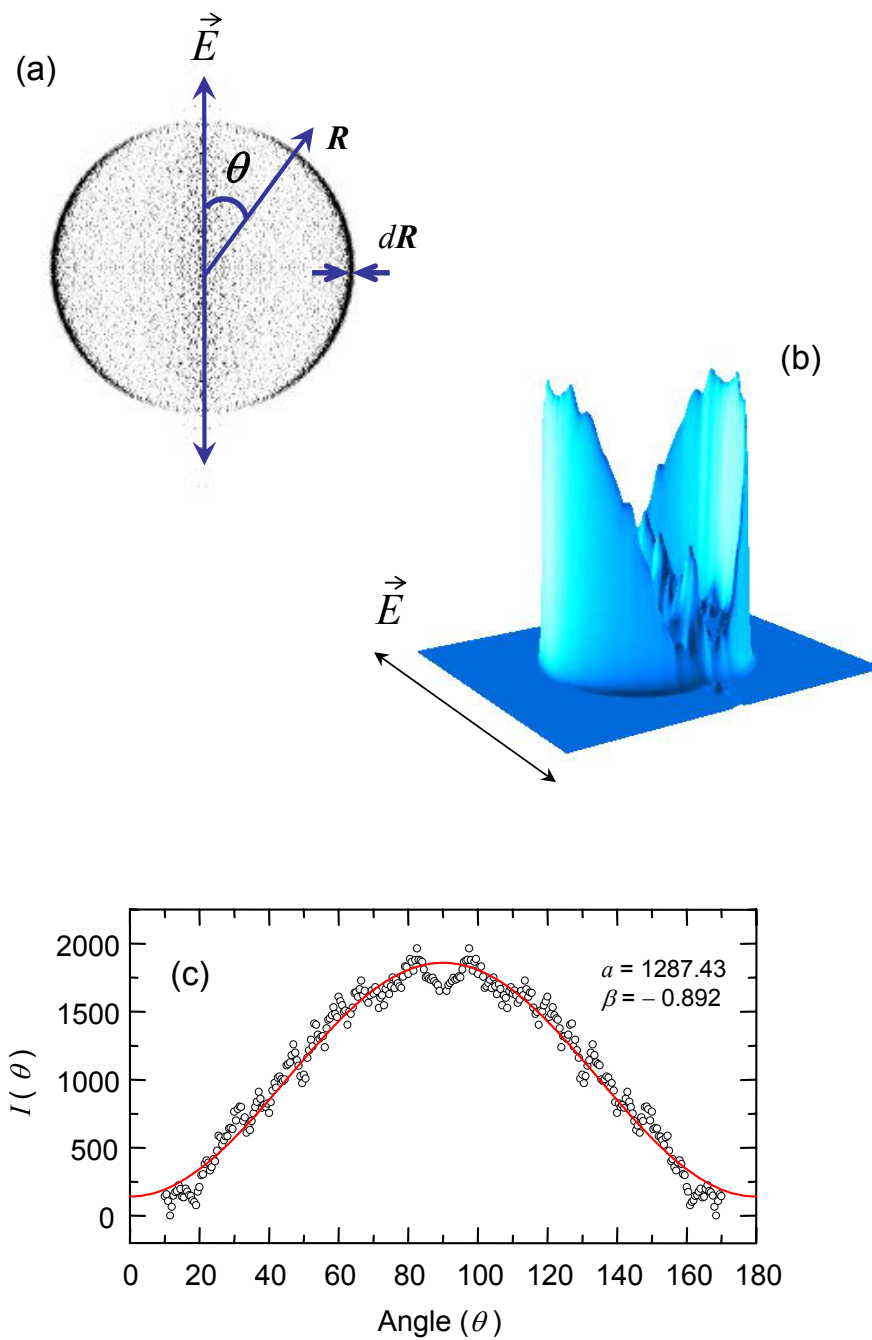


Figure 2.10: Photoelectron angular distributions (PADs) for atomic O^- at 532 nm.

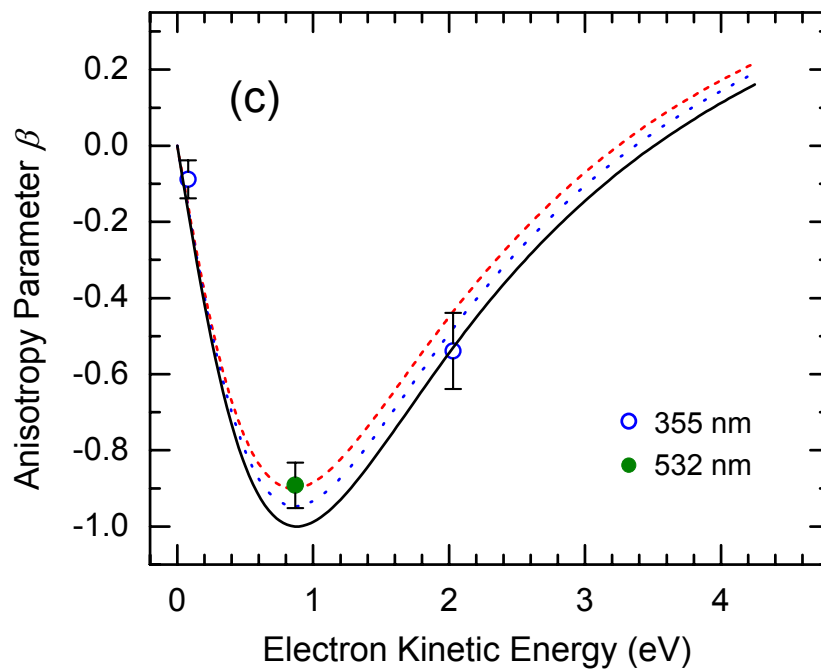
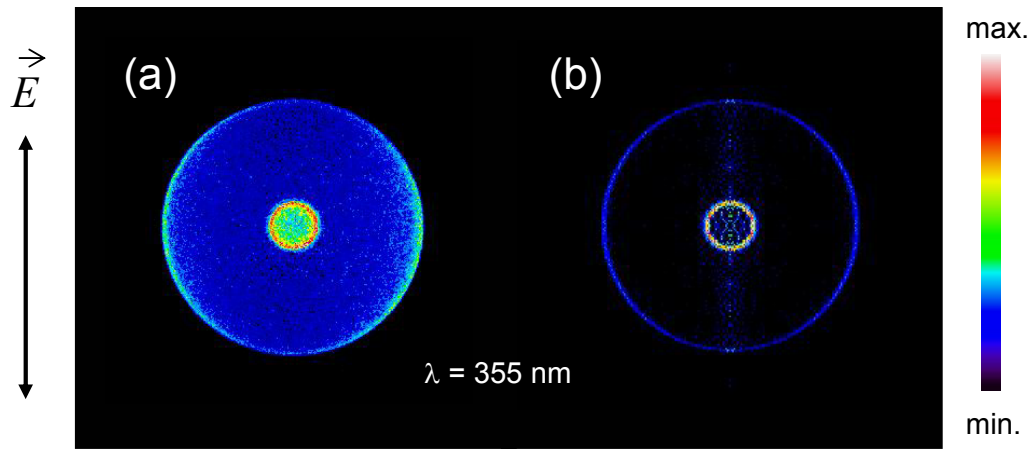


Figure 2.11: Kinetic energy dependence of β : O^- image at 355 nm and its Cooper-Zare curve. (a): raw image at 355 nm. (b) Abel-inverted reconstructed image. (c) Experimentally measured β parameters. The plotted lines correspond to the $\ell = 1$ Cooper-Zare curves with $A = 0.57$. The cosine of the partial-wave phase shift is 0.925 [27] for the dashed line, 0.96 [29] for the dotted line, and 1.0 for the solid.

CHAPTER 3

MOLECULAR AND CLUSTER ANIONS OF CARBON DIOXIDE

3.1 An Excess Electron on Carbon Dioxide

Though most of this chapter deals with the negatively charged clusters of carbon dioxide and their electron binding motifs, bare CO_2^- is on itself a very interesting species considering that the attachment of an excess electron to the CO_2 molecule is not a trivial process. Low-energy electron bombardment to CO_2 has attracted the attention of many experimentalists and theorists, especially the strong rise in the scattering cross section close to threshold (zero kinetic energy) and the narrow resonance peak centered near 3.8 eV (see for example the compiled values of Itikawa [31] and references therein). It is well established that the resonant behavior arises from the formation of a short-lived $^2\Pi_u$ negative ion [17, 32] and the behavior at lower energies is attributed to the presence of a virtual state of $^2\Sigma_g^+$ symmetry [17, 33, 34, 35, 36]. On the other hand, a metastable CO_2^- anion with lifetimes in the microsecond range has been observed by many diverse processes, including dissociative electron attachment to organic molecules containing a bent O–C–O subunit [37, 38, 39], fast double electron transfer to CO_2^+ ions [40], cesium ion sputtering on a gas cathode containing CO_2 [41], and electron collisions with CO_2 clusters [42]. These long-lived CO_2^- species are understood in terms of a bent structure of C_{2v} symmetry that is stable with respect to vertical electron loss [43].

Upon sufficient bending (or stretching) the virtual state becomes electronically bound

in a totally symmetric diffuse orbital by virtue of the long-range interactions caused by the multi-pole and polarization forces [35, 44, 45, 46]. The ${}^2\Pi_u$ short-lived anion could also become bound by enough stretching of the C–O bonds and/or bending [47, 45]. The degeneracy of the $\Lambda = \pm 1$ components of the ${}^2\Pi_u$ state is lifted by bending, resulting in two coupled branches of 2A_1 and 2B_1 symmetry [43, 48]. The connection between the metastable anion and the short-lived scattering states has been a subject of much debate and a short summary is provided below.

A different kind of metastable anions with lifetimes in the millisecond range have been observed and rationalized in terms of higher-spin states [49, 50, 51]. These states are not discussed here, and we focus on the species with μs lifetimes generated by electron collisions on molecules and clusters.

3.1.1 Long-Lived 2A_1 Metastable State of CO_2^-

Intuitively, one does not expect the closed-shell CO_2 neutral molecule to effectively capture an excess electron at its equilibrium geometry (C–O bond distances of 1.161 Å and an angle $\angle\text{OCO}$ of 180° [52]). Indeed, resonant electron scattering experiments have measured a lifetime of only a few femtoseconds with respect to spontaneous re-emission of the electron (autodetachment). A minimal energy structure of C_{2v} symmetry with stretched C–O bond lengths (1.24 Å) and significantly bent ($\angle\text{OCO} \sim 138^\circ$) lies in a shallow potential well in lowest (2A_1) energy curve of CO_2^- [43, 53, 44]. This structure is energetically lower than that of the same geometry neutral by over 1 eV, and is trapped in the potential well facing a barrier large enough to temporarily prevent electron autodetachment. This energetic conditions are consistent with a metastable CO_2^- state

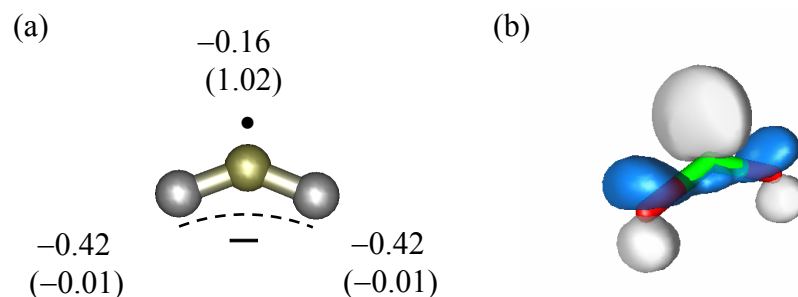


Figure 3.1: CO_2^- as a distonoid radical. Geometry optimized at the MP2/aug-cc-pVTZ level of theory. The C–O distances are 1.237 Å and the angle $\angle\text{OCO} = 137.32^\circ$. (a): spin-charge separation: the ESP atomic charges calculated with the MP2 density are shown on the top row next to the atom, the Mulliken spin densities are displayed below (in parenthesis). (b): Highest occupied molecular orbital (A_1 symmetry).

capable sustaining the the $90 \pm 20 \mu\text{s}$ lifetime observed by Compton et al. [38, 39, 54, 55]. The calculated lifetimes of 100–150 μs for this 2A_1 state [56] are in good agreement with the above experimental value. The calculations also confirmed that the anion is in its ground vibrational state. The long-lived anion can be prepared via precursors already containing a bent configuration or in a cluster environment as mentioned above.

Although this species is vertically stable, adiabatically it is unstable to electron autodetachment and the experimental value of $-0.6 \pm 0.2 \text{ eV}$ [54] has been determined for the adiabatic electron affinity for CO_2 . In good agreement with the experimental value are the theoretical values of -0.67 eV obtained at the CCSD(T)/6-311+G(3df) level of theory [53] and the more recently calculated -0.544 eV at the equation-of-motion coupled-cluster EOM-CCSD level with the aug-cc-PVQZ basis set [57].

Infrared signatures of the long-lived CO_2^- anion have been detected in matrix isolation experiments. Thompson and Jacox [58] assigned the observed infrared absorption at 1658.3 cm^{-1} to the asymmetric stretching fundamental of an isolated (bent) CO_2^-

anion—assignment corroborated in further IR studies [59]. The photoelectron spectrum for CO_2^- is also consistent with this bent ion picture, showing non-existing Frank-Condon overlap between the lowest lying vibrational levels of the anion and the lowest levels of its neutral [60]. The onset of the observed spectral band is at around 0.4 eV and peaks at 1.4 eV corresponding to vertical detachment from the anion at its equilibrium geometry, leaving the remaining neutral highly excited in the bending vibrational coordinate [60].

Schwarz and co-workers [40] postulated that the carbon dioxide radical anion could be thought of as a distonic-like radical (in the recent proposed terminology, a distonoid radical [61]) with an unpaired electron localized mostly on the central carbon and the excess negative charge delocalized mainly between the two oxygens as shown in Figure 3.1(a). In this pseudo-biradical anion, the negative charge and the spin site are located in different symmetry planes, i.e. in orthogonal π and σ orbitals respectively as illustrated by the HOMO in Figure 3.1(b). This charge and spin separation stabilizes the CO_2^- radical anion on its metastable state.

3.1.2 Temporary Anion States

The CO_2 molecule possesses two low lying unoccupied orbitals of σ_g and π_u symmetry. As discussed above, CO_2 cannot bind an extra electron in its equilibrium geometry to form a stable anion. Instead, electron attachment to the linear ground state can lead to a $^2\Sigma_g^+$ and a $^2\Pi_u$ resonances. In the linear geometry, the $^2\Pi_u$ is a typical shape resonance, whereas the $^2\Sigma_g^+$ represents a virtual state [17].

In the $^2\Pi_u$ shape resonance, the electron is trapped within the centrifugal barrier imparted by the angular momentum ($\Lambda = 1$) to form a short-lived negative ion. Upon

bending, it splits into two 2A_1 and 2B_1 components that are coupled via the Renner-Teller effect [43, 48]. In the time-dependent picture, the eigenvalues for the ${}^2\Pi_u$ resonance are described by the complex Siegert energies:

$$E_{res} = E_r + i\Gamma/2, \quad (3.1)$$

where Γ is the resonance width related to its lifetime by $\tau = \hbar/\Gamma$ and the real part determines the position of the resonance (vertical electron affinity). Typical values are $E_r = 3.8$ eV and $\Gamma = 0.33$ eV [32, 62, 63]. From these numbers, a lifetime of about 2 fs is estimated for the transient ${}^2\Pi_u$ anion.

The virtual state of ${}^2\Sigma_g^+$ can be loosely described as a nearly bound *s*-wave state in the electron plus molecule potential. It accounts for the situation in which a bound state of the electron and the CO₂ is “on the verge of being born” [64]. A virtual state is not a physical state in terms of a true bound state or even an autoionizing state, however it causes CO₂ to be extraordinary efficient in scattering low-energy electrons with de Broglie wavelengths much greater than the size of the molecule. This scattering interaction happens without significant time delays [65] and the system acquires a totally symmetric vibronic character. As the system stretches or bends, the virtual state could become electronically bound by means of multi-pole and polarization forces, with the excess electron occupying a diffuse orbital of 2A_1 symmetry [35, 44, 45, 46]. This weakly bound state is capable of sustaining vibrational Feshbach resonances that explain the vibrational structure observed by Allan well below the ${}^2\Pi_u$ resonance [64]. This diffuse state has been ascribed as a “gateway” into the formation of the valence long-lived anion [44] similar to the coupling between dipole-bound and valence states (see for example [66]). Sommerfeld [44] successfully calculated a cut through the *adiabatic* potential energy

surface that shows the change in character of the ground state from valence to diffuse, both having 2A_1 symmetry. He shows that starting from the valence equilibrium structure of CO_2^- and approaching linearity, the energy curve from the valence state increases steadily until it experiences avoided crossing with the diffuse state in proximity to the neutral curve. This coupling generates a barrier of ~ 50 meV in the lower potential and then the adiabatic curve drops below the bent equilibrium energy just before merging into the neutral curve. This crossing (or merging) with the neutral surface occurs at bending angles around 150° – 155° and consequently the system is considered no longer bound. Crossing or tunneling through this barrier is then responsible for changes in character from valence to diffuse –and vice versa– with some probability of ending in fast electron loss (therefore limiting the lifetime of the valence anion to the μs range).

Quantum chemical computations using only one set of diffuse functions will attempt to converge to a neutral CO_2 plus a free electron after the anion potential crosses the neutral curve as the $\angle OCO$ angle increases toward linearity. This is illustrated in Figures 3.2 (c) and (d) for the potential energy curves calculated by the author using the Gaussian suite of programs [67] at the MP2/6-311+G(3df) and MP2/aug-cc-pVTZ level of theory, respectively. These curves resemble the surface cut reported by Gutsev et al. [53]. The traces shown with dashed lines in these two plots (shown after crossing the neutral) have been proven not to be correct [44, 45], and are displayed here only to show the effect of the basis set. Nonetheless, these calculations are qualitatively correct in the sense that close to linearity the electron turns into a diffuse s -wave that attempts to free itself from its bondage to CO_2 . Only highly diffuse basis sets will reproduce the real behavior of the weakly-bound region found close to the autodetachment threshold as discussed by

Sommerfeld [44].

In absence of any diffuse functions the calculations retain the electron in the LUMO of neutral CO₂ throughout the entire potential curve, therefore qualitatively describing the *diabatic* components of the ²Π_u resonance without attempting any transitions to the diffuse state (which is a mix of higher virtual orbitals [44, 45]). The energy curves obtained with this approach are displayed in Figures 3.2 (a) and (b) calculated at the MP2/6-311G(3df) and MP2/cc-pVTZ level, respectively, and they resemble the curve obtained by Krauss and Neumann [43]. Notice that *in the bound region*, the curves (c) and (d) containing diffuse functions give lower energy values for the equilibrium CO₂⁻ anion, approaching more accurate values for the electron affinity and for the depth of the “trapping” potential well.

The diffuse and the valence states are by nature diabatic states that are coupled by the electronic Hamiltonian. We know that the ²Π_u shape resonance captures the electron temporarily into the LUMO of neutral CO₂ mediated by the centrifugal barrier in the effective radial potential. If bent, this state splits into a ²B₁ and a ²A₁ resonances coupled by the Renner-Teller effect [48]. The diffuse state is weakly-bound by means of multi-pole and polarization forces that arise after the molecule bends (or stretches) and it exists in relative proximity to the neutral curve [46]. This diffuse state has a totally symmetric orbital of ²A₁ symmetry (*s*-type orbital) and experiences avoided crossing with the ²A₁ adiabat originated from the Renner-Teller pair. This coupling gives an open channel for a diffuse to valence character change (and viceversa). Transition implicated in the formation of the metastable anion by zero-energy electron impact and as a likely autodetachment route for the valence anion. Similar avoided crossings are

also experienced on the symmetric stretch coordinate with a slightly bent anion, giving an adiabatic curve that could be traced first to the diffuse state upon increasing C–O bond lengths —situation that is relevant to the possible pathways for the formation of the stable anion upon electron attachment to CO₂ [45].

Thus, we have a system where the two Renner-Teller components and the diffuse state are vibronically coupled. A complete description of the CO₂⁻ radical anion will require a careful study of the non-adiabatic coupling elements, the resonant states, and regions that are electronically bound. A qualitative picture of these states is adapted from the model proposed by Allan [68] and is displayed in Figure 3.3.

3.2 Negatively Charged Clusters of Carbon Dioxide

3.2.1 Cluster Formation

In the pioneer work of Klots and Compton [69], formation of (CO₂)_n⁻ clusters with $2 \leq n \leq 6$ was observed in a TOF mass spectrometer as a result of electron attachment to a supersonic beam of carbon dioxide. No metastable decay via autodetachment or dissociation was observed for as long as 2 ms. In a latter work [16], they attributed the formation of these negatively charged clusters to a process of evaporative electron attachment (also discussed in Chapter 2, Section 2.3). In this process, the physical mechanism by which an electron attaches to a neutral cluster must involve temporary anion states of a monomeric component, namely via low-energy resonances in the electron-molecule system. If the electronic energy is rapidly redistributed into the internal degrees of freedom of the cluster environment, the temporary anion can become stable (or metastable) with respect to autodetachment and the redistributed excess energy is cooled

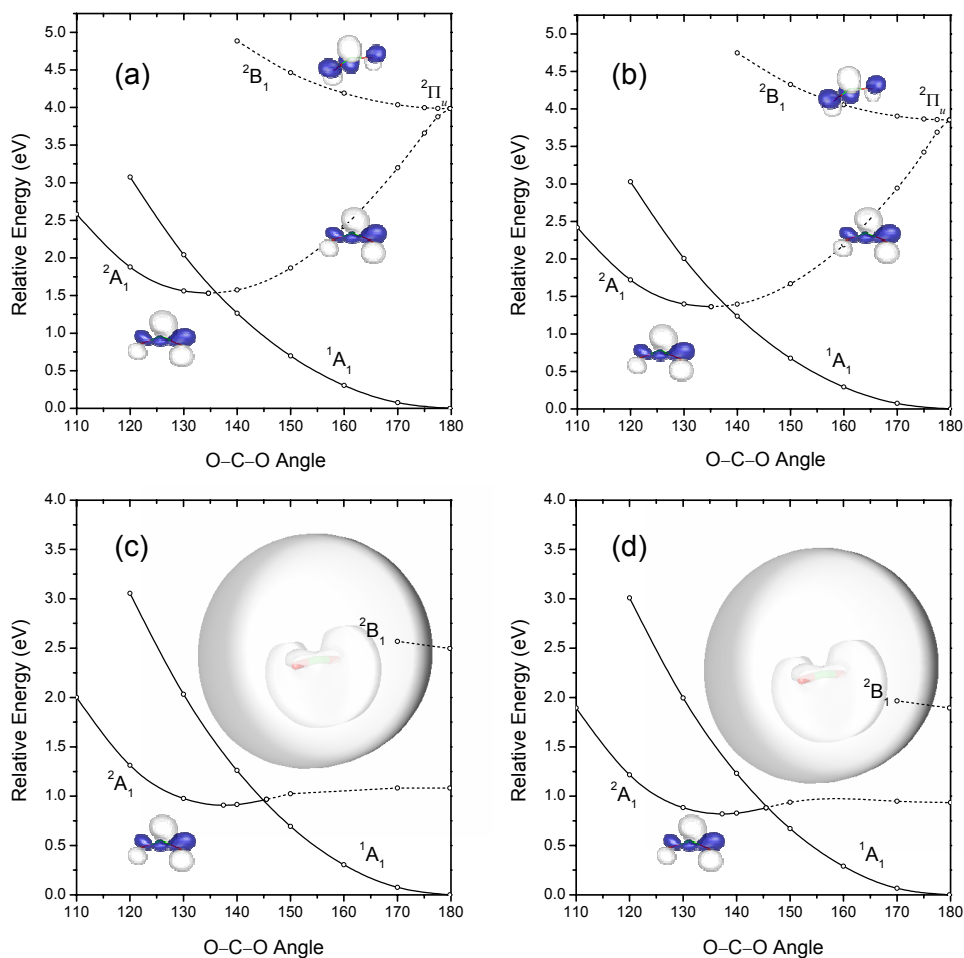


Figure 3.2: The MP2 potential energy curves calculated as a function of the O-C-O bending angle (degrees) for different basis sets. (a): 6-311G(3df); (b): cc-pVTZ; (c) 6-311+G(3df); and (d) aug-cc-pVTZ. The isosurfaces show a representation of the HOMO for a specific region of the curves. The results for the unbound region are shown with dashed lines and are included only to show the effect of the basis set. When no diffuse functions are included as shown in (a) and (b), the electron remains on the LUMO of CO₂ and one can qualitatively reproduce the Renner-Teller coupling. The addition of one set of diffuse functions gives better results in the bound region, however it converges to a free *s*-electron and a neutral CO₂ as we approach the linear geometries. The upper 2B_1 state in (c) and (d) gives a diffuse electron wave of *p* character (not shown) and does not correlate to the component from the $^2\Pi_u$ shape resonance. A much better potential for the Renner-Teller pair is calculated by McCurdy et al. [48] and the correct adiabatic potential surface of the ground state (including a diffuse bound state) is given by Sommerfeld [44].)

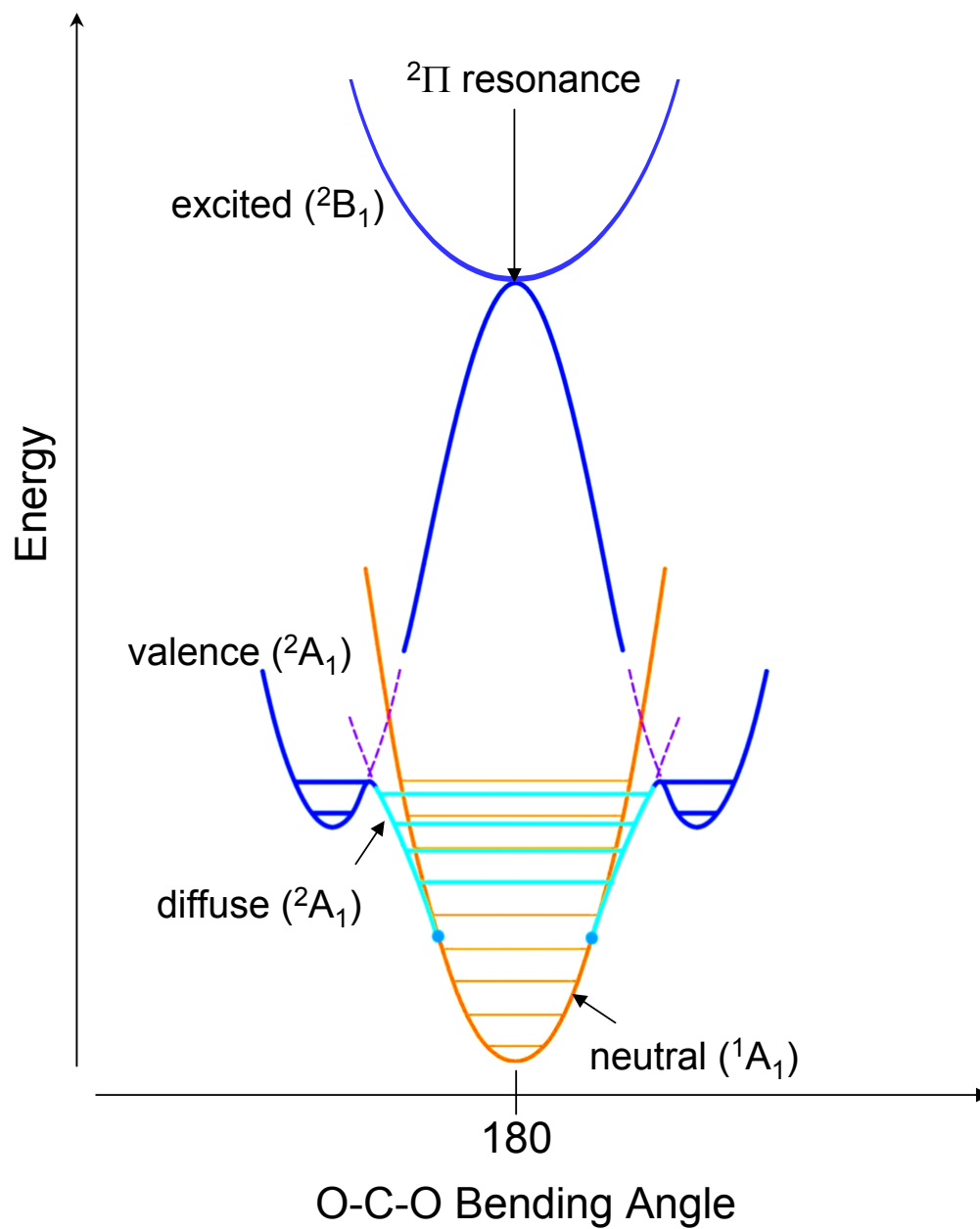


Figure 3.3: Qualitative curves for CO_2^- showing the diffuse state and non-adiabatic couplings. Based on the description given by Allan [68].

away by evaporation of neutral monomers.

Stamatovic et al. [70] found a less dissociative production mechanism by attachment of electrons close to zero kinetic energy (compared to the previous work in the 2.5–4.5 eV range). Using a high resolution laser photoelectron attachment (LPA) method, Hotop and co-workers [71] observed narrow vibrational Feshbach resonances of the type $[(\text{CO}_2)_{n-1}\text{CO}_2(v_i)]^-$ in the electron attachment spectra close to threshold. This process involves a vibrationally excited monomer ($v_i > 1$) that attaches a diffuse electron weakly bound to the cluster by long range forces [71, 72, 73]. Evolution into the long-lived valence anionic clusters involves redistribution of this vibrational excitation among the soft modes of the cluster, resulting in evaporation of a small number of CO_2 solvent molecules (most likely just one). The minimum cluster size generated by this method was $n = 4$ [71].

The $(\text{CO}_2)_n^-$ cluster series can be reproducibly generated by low energy secondary electron attachment to van der Waals clusters formed on the supersonic expansion of carbon dioxide gas [3, 74]. A representative mass spectrum of the medium size range $(\text{CO}_2)_n^-$ cluster anions formed on our experimental apparatus is shown in Figure 3.4. The clusters are generated by expansion of undried CO_2 into vacuum through a pulsed (50 Hz) nozzle with a stagnation pressure of 20–40 psi. A continuous electron beam of 1 keV intersects the expansion and resulting slow secondary electrons are responsible for anion formation (see Chapter 2). The discontinuities in cluster ion intensity that are observed at $n = 10, 14,$ and 16 in Figure 3.4 are consistent with the magic numbers $n = 4, 7, 10, 14,$ and 16 reported by Alexander et al. [74], and are attributed to structures of special stability.

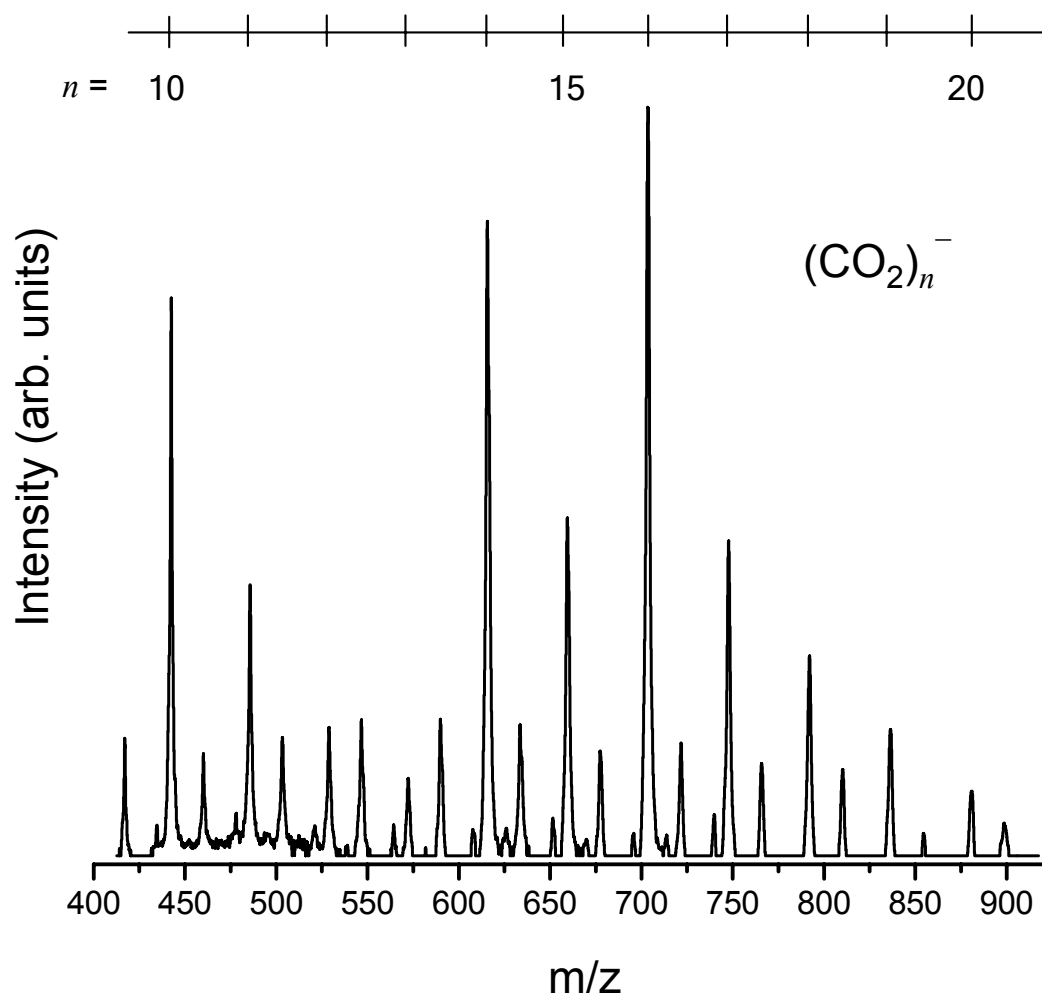


Figure 3.4: Mass spectrum of parent $(\text{CO}_2)_n$ cluster anions optimized for high-masses. The peaks in between the labeled clusters correspond to monohydrated clusters $(\text{CO}_2)_n^- \cdot \text{H}_2\text{O}$. Compare to the spectrum in Alexander et al. [74].

Negatively charged clusters of carbon dioxide have attracted some attention in the realm of electron transfer reactions using supercritical fluids as solvents. Shkrob et al. [75, 76] performed experiments where they have observed $(\text{CO}_2)_n^-$ as a transient reducing species in supercritical (sc)- CO_2 . Cluster anions of carbon dioxide have also been observed in condensed environments following electron capture by thin film of condensed CO_2 . The attachment cross section for these thin films showed a peak at energies corresponding to the $^2\Pi_u$ resonance as well as in the low energy peak assigned to the formation of Feshbach resonances in $(\text{CO}_2)_n^-$ cluster anions [77].

3.2.2 Cluster Geometries and Electronic Isomers

A fundamental question that follows the attachment of an extra electron to a cluster is whether the excess electron is delocalized or, if localized, what is the nature of the molecular ion (cluster core) that is embedded in the remaining “neutral” shell. Photoelectron spectroscopy has been the tool of choice for characterizing the electronic structure of such systems. Bowen and co-workers [60] noticed a jump of over an electronvolt for the VDE in the photoelectron spectrum of the dimer $(\text{CO}_2)_2^-$ compared that of bare CO_2^- . This observation was inconsistent with the formation of an ion-neutral complex, typically showing increments of 0.2–0.3 eV in VDE due to the stabilizing electrostatic interactions of a neutral CO_2 molecule on a typical anion. This led Fleischman and Jordan [78] to explain the observed photoelectron spectra in terms of a dimer anion of D_{2d} symmetry containing a C–C covalent bond (order of 1/2) where the excess electron is equally shared between two (bent) CO_2 components. They reported that this dimer structure possessed a small, but positive, adiabatic electron affinity. Our

calculations on the dimer anion at the MP2/aug-cc-pVDZ level of theory are shown in Figure 3.8. This covalent O_2CCO_2^- anion is considered as the singly ionized analogue of the oxalate $(\text{C}_2\text{O}_4)^{2-}$ anion. Fleischman and Jordan [78] also obtained a dimer of D_{2h} symmetry and an ion-neutral complex of C_s symmetry that were close in energy, however the proposed D_{2d} dimer that explained the observed VDE has also been confirmed by infrared spectroscopy (see for example [58, 59]).

Johnson and co-workers [79] greatly expanded the photoelectron spectroscopy experiments initiated by Bowen and Eaton [60] for larger clusters. They observed a steady increase in VDE from $n = 2$ to 5 consistent with a stepwise stabilization by neutral solvents, but for $n = 7$ however, the observed VDE dropped abruptly to a value ~ 0.7 eV lower than that for $n = 5$. They attributed this effect to a switch in the identity of the anionic cluster core (electronic isomerization). For $(\text{CO}_2)_6^-$ two different VDE values were reported, suggesting coexistence of two different electronic isomers possibly undergoing interconversions. Their data suggested that clusters with $2 \leq n \leq 5$ had a dimer-based cluster core $(\text{CO}_2)_2^-(\text{CO}_2)_{n-2}$ (type-II) and that it switched to a monomer-based ionic core $(\text{CO}_2)^-(\text{CO}_2)_{n-1}$ (type-I) starting at $n = 7$. The $(\text{CO}_2)_6^-$ cluster being a mixture of type-I and type-II isomers. A later experiment [80] showed again a steady increase in VDE from $n = 7$ to 13 and surprisingly, another discontinuity showed up between $n = 13$ and $n = 14$ attributed to a come back of the dimer-based structures for clusters with $n > 13$.

The coincidence of these abrupt jumps with the magic numbers 7 and 14 observed in the mass spectrum suggested that the switch to type-I at $n = 7$ and back to to type-II at $n = 14$, was dictated by the formation of "closed-shell" structures, and perhaps the CO_2^-

monomer core was symmetrically surrounded by a cage of six CO₂ solvents at $n = 7$ and the O₂CCO₂⁻ core symmetrically surrounded by twelve CO₂ solvents at $n = 14$ in a somewhat deformed icosahedral arrangement [81]. Icosahedral shell-closing structures obtained by the packing of twelve spheres have been studied in detail (see for example [82]). Such reasoning brought Johnson and co-workers to study the effects of solvation asymmetry on the charge delocalization for the dimer anion based its high polarizability [83]. They concluded that the dimer, preferentially stabilized by a charge-resonance effect, collapsed to monomer-based for clusters possessing an incomplete *asymmetric* solvation shell in the $n = 6$ –13 range, where one of the monomer becomes preferentially stabilized by virtue of the asymmetric interactions (the two CO₂ moieties are no longer degenerate). With the first solvation shell around the dimer core effectively being completed at $n = 14$, a symmetrical icosahedral environment of twelve CO₂ molecules around the dimer supported their hypothesis that the intrinsic stabilization of the excess electron on a dimer anion remains in a symmetric environment. Mid-infrared spectroscopy studies on $2 \leq n \leq 17$ confirmed that the cluster core for the size range was indeed either dimer- or monomer-based. However, the core-switching process seemed to be a smooth progressive transition with a range of coexistence of three or four clusters rather than a prompt change [83].

3.3 Cluster Photochemistry and Photoelectron Dynamics

3.3.1 Cluster Photofragmentation

Interaction of (CO₂)_{*n*}⁻ cluster anions with a photon promotes, besides photodetachment, cluster photofragmentation. For clusters in the $n > 13$ range (where the cluster are

dimer-based) the fragmentation process yields $(\text{CO}_2)_k^-$ fragment anions with $k < n$ [74]. The experimental photofragment mass spectrum of $(\text{CO}_2)_{16}^-$ acquired in our apparatus by excitation at 355 nm is shown in Figure 3.5. A resulting value of $\langle k \rangle = 4.98$ was extracted by integrating the individual peaks, indicating that an average of eleven CO_2 's were evaporated. Although the mechanisms by which this photofragmentation pattern occurs remains unknown, we can predict that it is triggered either by the photodissociation of the $(\text{O}_2\text{CCO}_2)^-$ cluster core into $\text{CO}_2^- + \text{CO}_2$, vibrational predissociation, or by a photoinduced electron transfer to the solvent shell followed by an evaporative cooling process. The D_{2d} dimer is bound by about 0.6 eV relative to $\text{CO}_2^- + \text{CO}_2$ and by 0.25 eV with respect to $2\text{CO}_2 + e^-$. Fragmentation of $n > 13$ clusters happens efficiently over a broad range of wavelengths in the near-UV to the visible range [74]. Interestingly a minor $\text{CO}_3^-(\text{CO}_2)_k$ fragmentation channel was observed for excitation with near-UV/UV light, but only for clusters in the $n = 6-13$ range [74, 84]. It was initially suggested that this channel was originated by a photoinitiated ion-molecule reaction. Coincidentally these clusters possess mainly monomer cores, and now we can certainly attribute this fragmentation channel to dissociation of the CO_2^- core into $\text{O}^- + \text{CO}$ followed by an $\text{O}^- + \text{CO}_2$ intracluster ion-molecule reaction (see Chapter 5). The fact that these products were observed only with high energy photons is consistent with the >3 eV necessary for the dissociation of CO_2^- into $\text{O}^- + \text{CO}$ [85]. For clusters with $n < 6$ no fragmentation has been observed so far. For these small dimer-based clusters, competition between photodetachment and photofragmentation strongly disfavors the fragmentation channels against the removal of the excess electron. The opposite holds for the larger ($n > 13$) clusters.

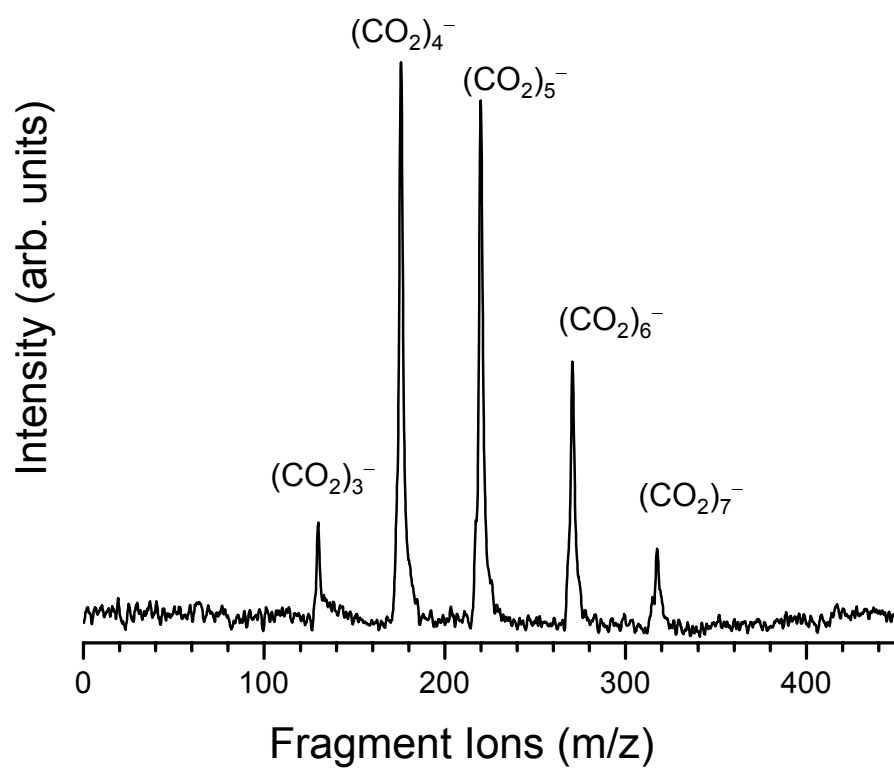


Figure 3.5: Photofragment mass spectrum of $(\text{CO}_2)_{16}$ with 355 nm. Compare to the results of Alexander et al. [74].

3.3.2 Photoelectron Imaging of $(\text{CO}_2)_n^-$

The raw photoelectron images for the $(\text{CO}_2)_n^-$ clusters, $n = 4-9$, obtained with linearly polarized 400 nm light are shown in Figure 3.6 (also found in Mabbs et al. [86, 87]). The 400 nm laser beam (120 $\mu\text{J}/\text{pulse}$) is generated as the second harmonic of the 800 nm fundamental (1 mJ, ~ 100 fs pulses) of a Ti:Sapphire laser (Spectra Physics, Inc.) using a BBO crystal. The Basis-Set EXpansion (BASEX) inverse-Abel transform algorithm is used to extract the energy spectra and angular distributions from the images.

Energy Spectra

The photoelectron kinetic energy spectra obtained from the reconstructed images were fitted by a sum of two Gaussian functions. Each Gaussian is used to describe the Franck-Condon profiles corresponding to the type-I or type-II individual photoelectron bands that account for the detachment transitions originating from these two different electronic isomers. Mathematically:

$$P(e\text{KE}) = e\text{KE}^{1/2} \{ A_{\text{I}} \exp[-(e\text{BE} - \text{VDE}_{\text{I}})^2 / w_{\text{I}}^2] + A_{\text{II}} \exp[-(e\text{BE} - \text{VDE}_{\text{II}})^2 / w_{\text{II}}^2] \}, \quad (3.2)$$

where $e\text{BE} = h\nu - e\text{KE}$ is the electron binding energy and w_{I} and w_{II} are the half-width parameters of the Gaussian functions. These parameters are related to the full widths at half-maxima (FWHM) by $\text{FWHM} = 2(\ln 2)^{1/2} w$. The pre-exponential factors A_{I} and A_{II} are proportional to the populations of the corresponding isomer, as well as the cross-sections for their detachment transitions. Photoelectron imaging allows for efficient detection of low energy electrons, therefore accounting for threshold effects becomes

crucial for these low energies. The approximate scaling factor $eKE^{1/2}$ is then included in Equation 3.2, manifesting a Wigner-like near-threshold behavior [30] for partial waves with the orbital angular momentum quantum number $\ell = 0$. Near-threshold scaling of higher-order waves is neglected in the model described by Equation 3.2, although it is estimated that their contributions would be much smaller.

The energetic parameters obtained from the images are summarized in Table 3.1. The VDE and FWHM fitting parameters for bands I and II are compared with the values reported by DeLuca et al. [79]. These two sets of values are in good agreement, with the only difference between our analysis and the previous work being the use of the $eKE^{1/2}$ scaling factor in Equation 3.2, affecting mostly the images with slower photoelectrons. The core-switching behavior and major structural trends involved in our measurements are also similar to the previously reported observations, including isomer coexistence at $n = 6$.

At a qualitative level, the evidence for core switching can be easily observed from the size of the images. The imaging conditions (including the electron lens voltages) are the same for all images shown in Figure 3.6. Moving from $n = 4$ to $n = 5$, the detector area that is covered by the images is somewhat reduced, corresponding to the expected increase in VDE caused by an extra solvent molecule—resulting in slower photoelectrons. The image for $n = 6$ however, is noticeably larger than that for $n = 5$. The presence of these faster electrons in the $n = 6$ image suggests a different isomer with lower VDE, consistent with the core-switching effect discussed above. The relative abundance of a particular electronic isomer (especially in the case of mixed clusters) depends upon the ion source conditions.

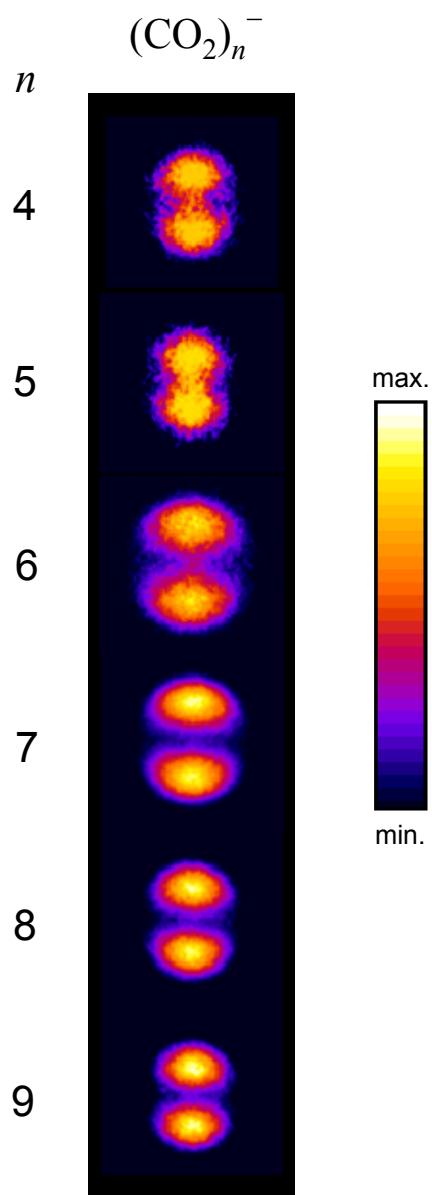


Figure 3.6: Photoelectron imaging of $(\text{CO}_2)_n^-$ clusters, $4 \leq n \leq 9$ at 400 nm. The laser polarization is vertical. See [86, 87]

Table 3.1: The VDE and FWHM values (in eV) for bands I and II, corresponding to cluster anions with monomer (type-I) and dimer (type-II) cores, respectively, used to fit the photoelectron energy spectra: (a) Mabbs et al. [87] (spectra obtained from the images in Figure 3.6); (b) from DeLuca et al. [79].

n	Core type	VDE		FWHM	
		(a)	(b)	(a)	(b)
4	II I	2.96	2.96	1.00	0.96
5	II I	3.25	3.25	1.07	1.06
6	II	3.40	3.40	0.73	0.73
	I	2.49	2.49	0.98	0.98
7	I	2.62	2.62	0.97	0.92
8	I	2.80	2.73	0.92	0.92
9	I	2.92	2.80	0.92	0.87

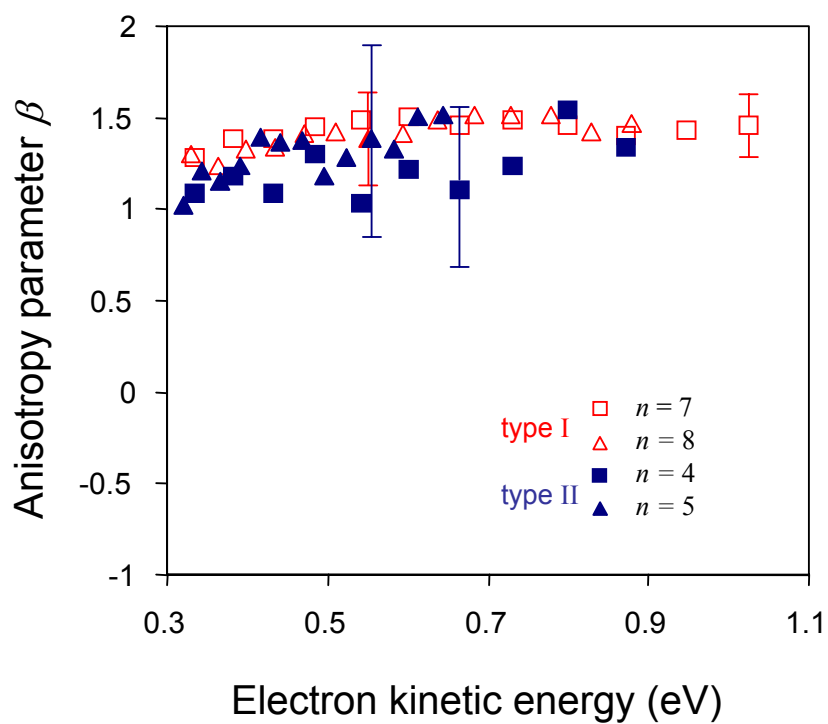


Figure 3.7: Energy dependence of the photoelectron anisotropy for representative monomer-based (empty symbols) and dimer-based (filled symbols) $(\text{CO}_2)_n^-$ cluster anions. See Mabbs et al. [87]

Angular Distributions

Upon visual inspection of Figure 3.6, a strikingly similarity is evident in the angular distributions of all images, with the PADs peaking along the laser polarization axis. The PADs are quantitatively described by the anisotropy parameter β which generally is energy dependent (see Chapter 2, Section 2.7). This dependence may complicate a numerical comparison between different species. However, a systematic evaluation can be achieved by examining the variations in the anisotropy parameter across a chosen (fixed) energy range. Figure 3.7 shows a plot of the energy-dependent β 's for representative monomer and dimer based cluster anions extracted from the images in Figure 3.6. In all cases, the values obtained for the anisotropy parameter are significantly positive and confined within a narrow range.

The *s&p* model for photodetachment [15] can be used to understand the parallel nature of the detachment process for the $(\text{CO}_2)_n^-$ cluster anions having either monomer or dimer-based cluster cores. In brief, this model first determines the molecular frame (MF) symmetry of the photodetached free electron wave (Γ_e) based on the known symmetry of the molecular orbital from which they have been removed (Γ_o) and the symmetry of the transition dipole moment (Γ_μ). Under the electric-dipole approximation, the direct product of the three symmetry species must contain the irreducible, totally symmetric representation (Γ_{TS}), that is

$$\Gamma_o \otimes \Gamma_\mu \otimes \Gamma_e \supseteq \Gamma_{\text{TS}}, \quad (3.3)$$

To obtain the partial wave composition of the free electron wave in the observed laboratory frame (LF), which give PADs averaged over molecular orientations, we make use of the MF symmetry constraints combined with chosen principal orientations of

the anion in the LF defined with respect to the laser polarization vector (z axis). A further approximation neglects the components of the free-electron wave with angular momentum quantum number $\ell > 1$, limiting the discussion to s and p partial waves only. For the monomer-based clusters, the core anion belongs to the C_{2v} point group and the HOMO is of A_1 symmetry. The dimer belongs to the D_{2d} and its HOMO corresponds to the A_1 irreducible representation. As outlined by Mabbs et al. [86], the $s&p$ model for these totally symmetric molecular orbitals gives final PADs peaking only along the z axis. For larger clusters, detachment occurs from a HOMO that is essentially either a monomer or a dimer. Solvation introduces some distortion to the torsional angle between the two CO_2 groups of the dimer core as shown in Figures 3.9 and 3.10, leading to a symmetry change of the core anion from D_{2d} to C_2 (or even D_{2h} !). However, the HOMO still belongs to the totally symmetric representation of the respective point group and the $s&p$ model indicates that PADs should peak along the z axis.

As useful as this analysis can be in predicting the direction in which the PADs are expected to peak for a detachment transition, it does not explain the astonishing quantitative similarity between the β values obtained in the photodetachment from the CO_2^- and covalent $(\text{CO}_2)_2^-$ cluster cores. A new approach is proposed which allows for such comparison. Consider the HOMO of $(\text{CO}_2)_2^-$ shown in Figure 3.8(a). This molecular orbital can be pictured as a combination of two spatially separated molecular orbitals that originate from the monomer-anion HOMOs. This LCMO-MO (linear combination of molecular orbitals to yield molecular orbitals) formalism [88, 89] as applied to the dimer anion is sketched in Figure 3.8(b). The LCMO approach allows the electron detachment to be thought of as a process emanating from two separated centers, each emitting waves

characteristic of the individual monomer units [86]. As it is shown in Figures 3.9 and 3.10, the HOMO for the core anion in larger (dimer-based) clusters can also be approximated in the same manner.

Interference of waves emanating from two centers depends on the differential distance from each center along a given direction in the far-field limit, as well as on the initial phase angle between the partial waves. The latter condition subject to the constraints on the overall symmetry of the photodetached electron wavefunction [86]. In the dimer-core anion, the separation between the two monomer groups ($\leq 2 \text{ \AA}$) is small compared to the de Broglie wavelength of the emitted electrons calculated in the far field. The wavelength for the photoelectron waves can be easily estimated using de Broglie's relation $\lambda = h/p$, where p is the linear momentum of the photoelectrons—for example, at $e\text{KE} = 0.7 \text{ eV}$ (corresponding to the middle of the relevant $e\text{KE}$ range) we obtain $\lambda_{dB} = 14.6 \text{ \AA}$.

Thus, the measured PADs come as the result of interfering electron waves being emitted from two almost overlapping (on the electron-wavelength scale) centers. Under these conditions, the experimental observations are dominated by waves emitted with similar initial phases (constructive interference), while the waves interfering destructively are suppressed. In this framework, the PADs for CO_2^- and $(\text{CO}_2)_2^-$ can be compared directly and are expected to be similar as the free-electron wavefunction is roughly a sum of the in-phase components emitted from two monomer units.

Insensitivity of the PADs to the presence of additional neutral CO_2 monomers around the dimer core-anion is supported by *ab initio* calculations of the cluster HOMO under differing solvation conditions. In previous work, Saeki et al. [90] extended their theoretical (MP2) study to $(\text{CO}_2)_n^-$, $n = 3\text{--}6$ clusters by employing a smaller 6-31G basis

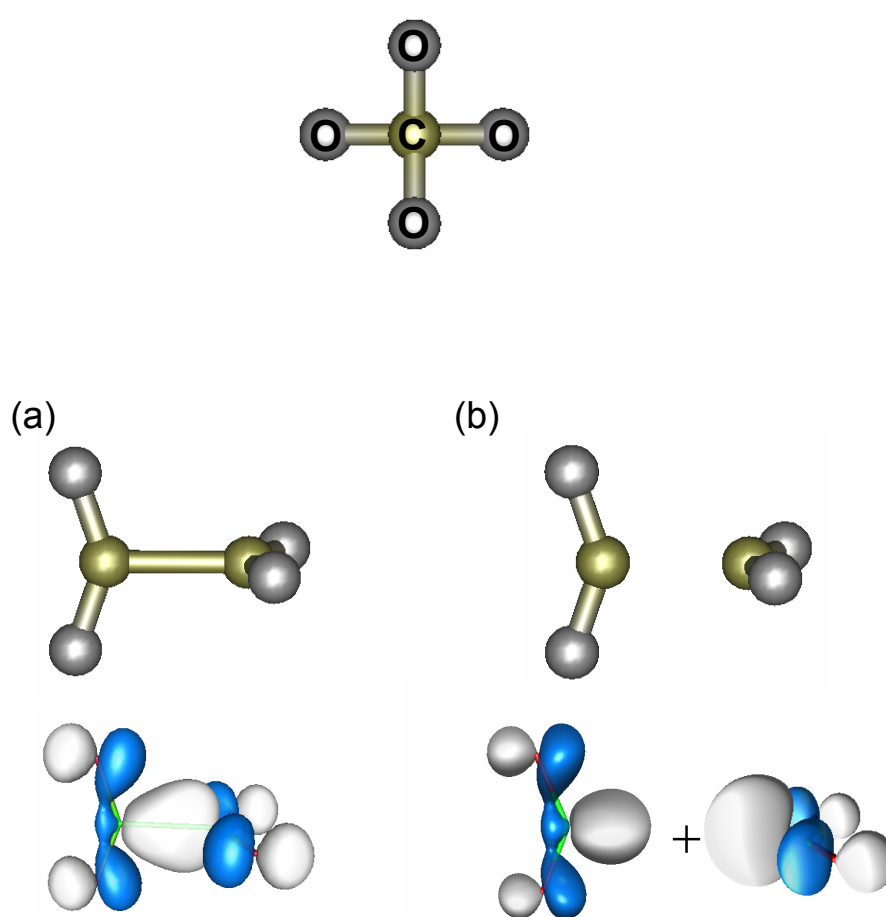


Figure 3.8: Optimized structures for the $(\text{CO}_2)_2^-$ dimer anion and its HOMO. Structural parameters give a C–C distance of 1.8 Å, C–O bond lengths of 1.23 Å, and an angle $\angle\text{OCO}$ of 124° at the MP2/aug-cc-pVDZ level of theory (a) a covalent bond between the two carbon atoms is formed; (b) the HOMO of the dimer as a linear combination of the monomer HOMOs.

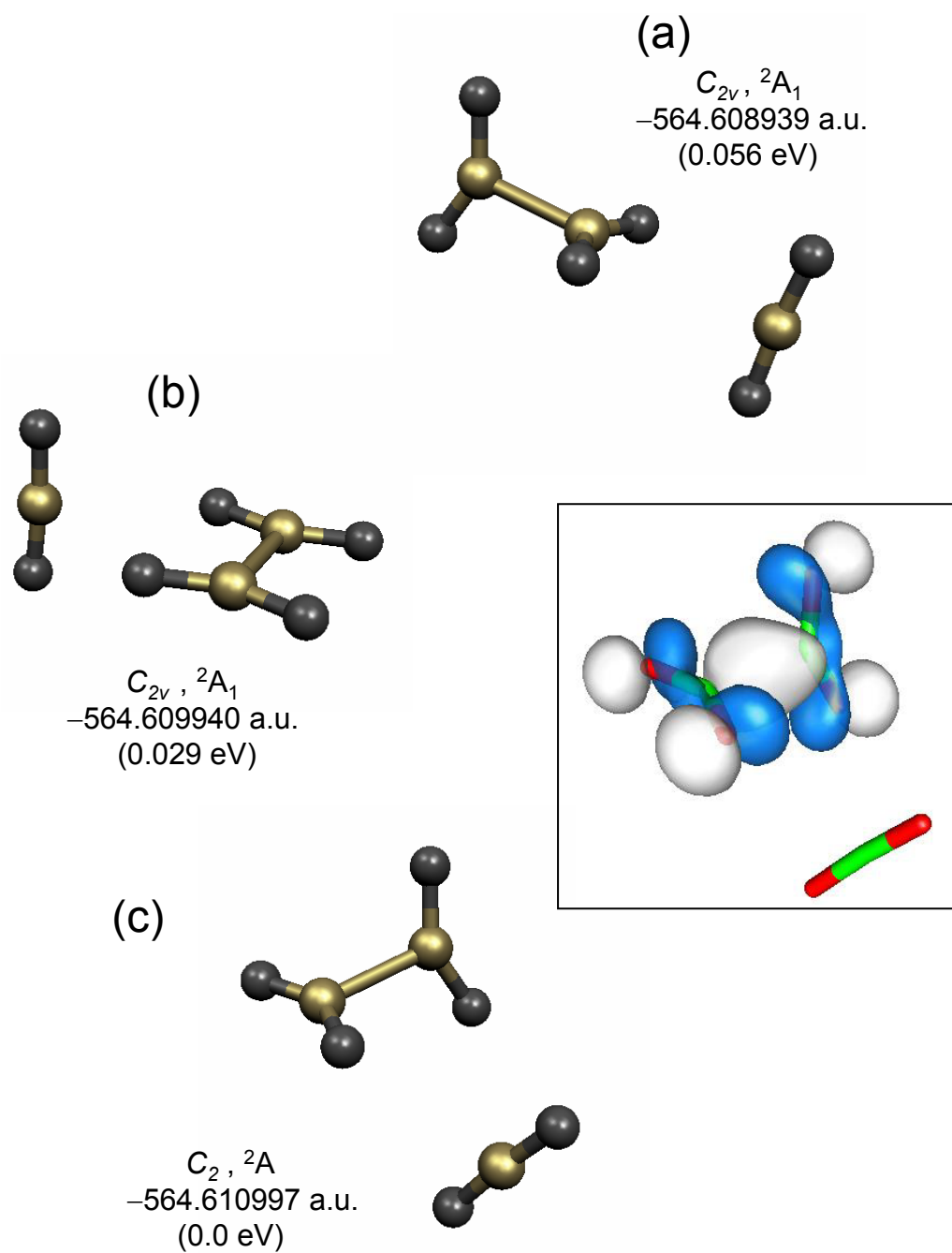


Figure 3.9: Optimized structures for dimer-based structures of the $(CO_2)_3^-$ cluster anions obtained at the MP2/6-311+G* level of theory. The insert shows the HOMO of (c) and it is representative of all HOMOs obtained for the structures shown above.

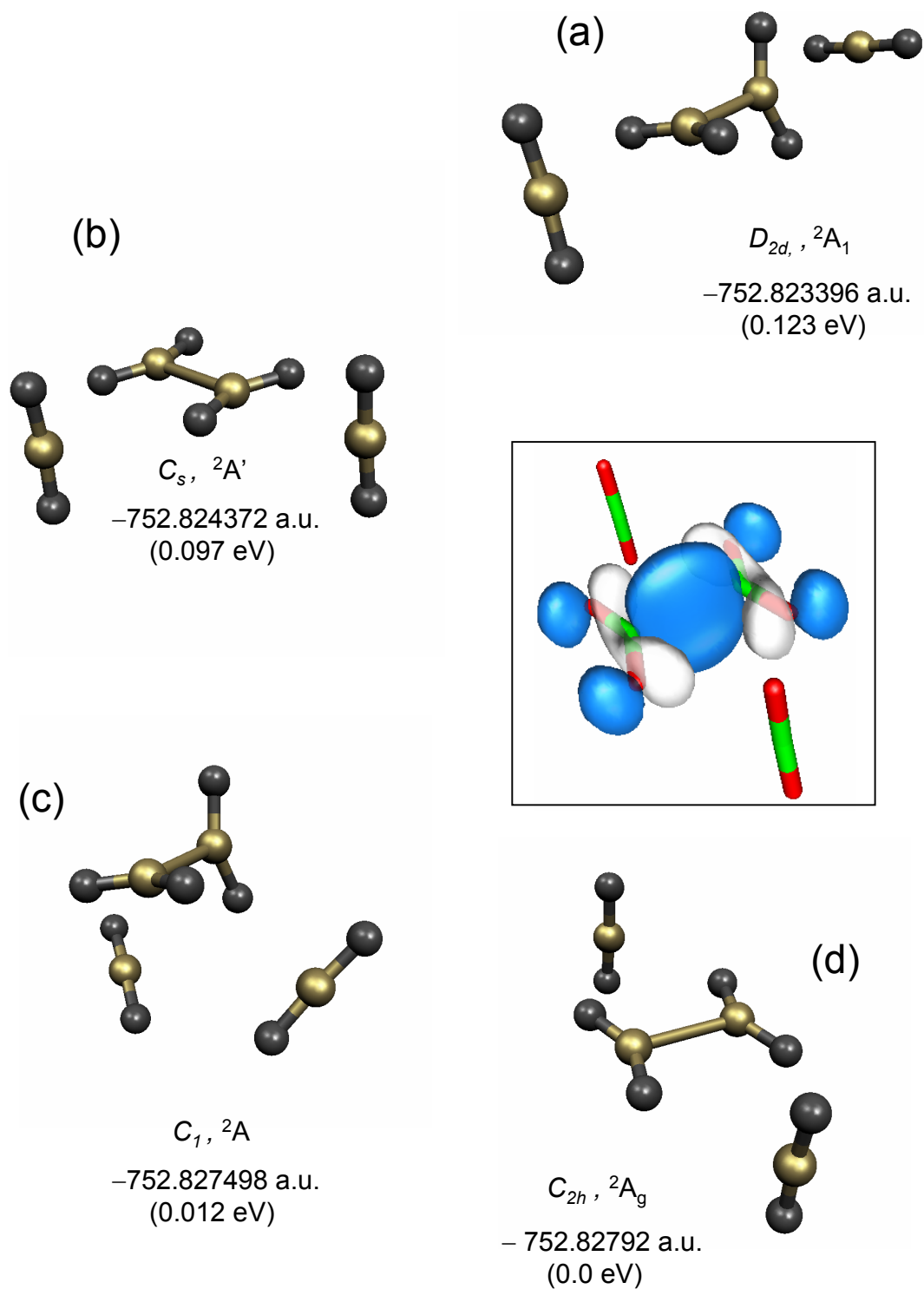


Figure 3.10: Optimized structures for dimer-based structures of the $(\text{CO}_2)_4^-$ cluster anions obtained at the MP2/6-311+G* level of theory. The insert shows the HOMO of (d) and it is representative of all HOMOs obtained for the structures shown above.

set (compared to the 6-31+G* basis used by the authors for the dimer anion [91]). In these calculations, the dimer core geometry changed to a planar, (approximately) D_{2h} structure solvated by the remaining $n - 2$ molecules. Intrigued by the change of core-anion symmetry from D_{2d} to D_{2h} , they re-optimized the geometry for $n = 3$ using the 6-31+G* basis set and commented that the inclusion of diffuse functions “restored” the predicted dimer-core structure similar to the D_{2d} symmetry characteristic of the unsolvated dimer anion. Since the size of the basis set appears to be critical in determining the core anion symmetry, we investigated the structures and the HOMOs for $(\text{CO}_2)_n^-$, $n = 2-4$ after geometry re-optimization [67] at the MP2/6-311+G* level, using the structures determined by Saeki et al. [90] as starting points for our calculations. We find that the dimer core anion in the most stable $(\text{CO}_2)_3^-$ cluster retains a D_{2d} -like geometry (formally C_2 symmetry since its dihedral angle is somewhat distorted by solvation) when the larger basis set is used (see Figure 3.9). Yet $(\text{CO}_2)_4^-$, in agreement with Saeki’s results, has an approximately D_{2h} lowest-energy core structure as shown in Figure 3.10. A new isomer with a D_{2d} core-anion was obtained in our calculations, lying only 0.012 eV above from the minimum D_{2h} structure. Nonetheless, the conclusions derived in the previous part of this Section using the LCMO dual-source interference approach are unaffected by the ambiguity between the D_{2h} , D_{2d} or C_2 geometries of the core anion since the HOMO of either dimer-anion can be represented as a combination of two monomer-anion orbitals.

3.4 Summary

In this Chapter, a review of the current understanding on the trapping of an excess electron by CO_2 is presented. Several mechanisms for the formation of the metastable CO_2^- radical

anion and its clusters are discussed. This long-lived anion is explained in terms of a valence state with a bent equilibrium geometry where the system is stable with respect to vertical electron loss but adiabatically unstable.

A short-lived negative ion of ${}^2\Pi_u$ symmetry is obtained when the excess electron is captured by the LUMO of CO_2 and retained momentarily by means of a centrifugal barrier (shape resonance). This transient anion has a lifetime of only a few femtoseconds with respect to autodetachment. A virtual state of ${}^2\Sigma_g^+$ symmetry is implicated in the interaction of very slow electrons with CO_2 . When the molecule is sufficiently stretched or bent, the virtual state becomes electronically bound by multi-pole and polarization forces in a diffuse, totally symmetric orbital. This weakly-bound diffuse state couples to the valence metastable state resulting in a small barrier that regulates the change in character from valence to diffuse (and viceversa) and therefore, the lifetime of the anion. Due to the large geometry difference between the neutral and the anion, combined with the transient nature of this resonances, the bent, long-lived, CO_2^- radical anion is better produced by electron attachment to precursors containing a bent O–C–O subunit or to van der Waals clusters where the excess electronic energy can be redistributed among the cluster degrees of freedom and cooled down by evaporation of monomers.

Cluster anions of carbon dioxide $(\text{CO}_2)_n^-$ are found to bind the excess electron either in a single monomeric component $\text{CO}_2^-(\text{CO}_2)_{n-1}$ (type-I) or delocalized over a symmetric dimer $(\text{CO}_2)_2^-(\text{CO}_2)_{n-2}$ (type-II), with the rest of the cluster components acting as neutral solvents around this ionic cluster core. Photoelectron spectroscopic studies have demonstrated that transitions between these two electronic isomers occur as a function of cluster size. For $n = 2-5$, type-II structures are found to be the predominant. The $n = 6$

case shows strong contributions from both electronic isomers, and then for the $n = 7-13$ range, type-I anionic cores become the dominant species (core-switching). Clusters with $n > 13$ switch back to a type-II structure. Asymmetric solvent interactions are postulated as the reason for localization of the excess electron into a monomer cluster core.

The photofragmentation pathways of the $(\text{CO}_2)_n^-$ cluster anions are briefly illustrated and the different fragmentation channels are discussed in light of the different nature of the cluster cores. Lastly, we report photoelectron images that are consistent with the core-switching phenomenon described above based on the energetics of the detachment process. The PADs originating from either monomer- or dimer-based clusters show a striking similarity besides their different HOMOs. We attribute this similarities in the angular distributions to an interference effect between the electron waves emitted from each of the CO_2 units forming the dimer. When the waves are in phase, constructive interference reproduces the PAD of the monomer, whereas out of phase waves cancel out by destructive interference. This argument is justified in terms of the LCMO model and the fact that the C–C internuclear distance is small compared to the de Broglie wavelength of the detached photoelectrons. *Ab initio* calculations in larger clusters indicate that the perturbation of extra solvent molecules to the HOMO is minimal, justifying therefore the application of the LCMO model as an explanation of the observed PADs.

CHAPTER 4

PHOTODISSOCIATION OF CO_2^- IN WATER CLUSTERS

4.1 Introduction

Of especial interest to this Chapter is the solvent-enabled chemistry that occurs in heterogeneous cluster anions. In other words, the reaction pathways for an anionic solute that are made possible (or enabled) by the presence of solvent molecules of a different species. It is well known that the outcomes of chemical reactions are affected by interactions with the surrounding environment. Hydration, in particular, is responsible for many important chemical processes. We therefore examine the photochemistry of the CO_2^- radical anion (discussed in detail in Chapter 3) in a cluster environment containing up to 20 water molecules. Both experiment and theory show that the excess electron in these clusters is in fact localized on the CO_2 moiety [81, 92, 93, 94]. The clusters can therefore be appropriately described as $\text{CO}_2^-(\text{H}_2\text{O})_m$.

In the gas phase, the CO_2^- radical anion has been observed as a metastable species (see for example [38, 39] and references therein). Regardless of the distinctly negative adiabatic electron affinity of the CO_2 molecule (-0.60 ± 0.2 eV [54]), a lifetime of 90 ± 20 μs with respect to autodetachment was reported for the CO_2^- anion [54, 55]. This long lifetime is understood in terms of the large geometry difference between the anion and neutral equilibria—i.e. at the bent equilibrium geometry of CO_2^- , the energy of the anion is lower than that of its corresponding neutral (positive vertical electron affinity) [43, 53].

The metastable CO_2^- ions can be further stabilized by solvation as discussed in Chapter 3. Intriguingly, Klots [95] reported that even one water molecule is sufficient to prevent autodetachment of the excess electron in the $\text{CO}_2^-(\text{H}_2\text{O})_m$ cluster series. Therefore, it is not surprising that the CO_2^- radical anion is stable in solution as the conjugate base of the acidic carboxyl radical CO_2H [96, 97, 98, 99].

Excited states in molecules and ions regularly serve as gateways into chemical transformations. For negative ions however, their relatively low electron detachment energies often make excited electronic configurations short-lived resonances that are embedded in the free-electron continuum. Anionic resonances are of key importance for the interactions of low-energy electrons and neutral molecules and clusters, playing also important roles in the dissociation and electron detachment dynamics of negative ions. In a cluster environment, such resonances can be stabilized by interactions with the solvent molecules, increasing their lifetimes and in some cases bringing them into the realm of bound stable states, opening new “solvent-enabled” reaction pathways for excited anions. We therefore report a solvation-induced shift from electron photodetachment towards the breaking of covalent bonds for the photoexcited CO_2^- anion embedded in water clusters.

The fragmentation studies presented in this chapter complement the previous photoelectron imaging studies of the $[(\text{CO}_2)_n(\text{H}_2\text{O})_m]^-$, $n = 1-12$, $m = 0-6$ cluster anions [8,9]. The experiment performed at 400 nm revealed that photoinduced autodetachment preceded over direct photodetachment for the case when four or more water molecules were present [94]. To understand the nature of the autodetaching states involved on the photoelectron imaging observations, we need to study the accessible excited states (or resonances) and their decay via different competing pathways, including

electron loss, charge transfer to solvent (CTTS), and anionic fragmentation. Therefore, in this chapter we explore the possible fragmentation channels of size-selected $\text{CO}_2^- (\text{H}_2\text{O})_m$, $m = 3\text{--}20$ cluster ions using 355 nm light. The reported photodissociation of the CO_2^- cluster core sheds light on the role of solvent-stabilized anionic excited states.

Some questions to be answered in this chapter are: a) what is the nature of the excited states and how are they affected by solvation? b) what is the bond strength of the CO_2^- anion and how is it affected by the presence of the solvent? c) how are solvent molecules ejected from the energized clusters? and d) can the electron be transferred to the water network? (see also the work by Habteyes [100] for further studies on these cluster series).

4.2 Experimental Details

The experiments were carried out on the experimental apparatus described in Chapter 2. The $\text{CO}_2^- (\text{H}_2\text{O})_m$ cluster anions are prepared by expansion of undried CO_2 at a stagnation pressure of 2 atm through a pulsed supersonic nozzle into vacuum. CO_2 tank impurities and trace amounts of water within the gas delivery lines serve as sources of H_2O . A continuous 1 keV electron beam crosses the supersonic expansion, and cluster anions are formed by secondary-electron attachment to neutral clusters. A transverse, pulsed electric field extracts the ions into a Wiley-McLaren type mass-spectrometer where the ions are brought to a temporal and spatial focus and detected with an in-line microchannel plate (MCP) detector. The mass-selected cluster anions of interest are interrogated with a pulsed laser beam. The ionic photofragments are analyzed with a single-field reflectron mass-spectrometer, where the parent and assorted fragment ions are separated according to their mass. The reflected fragments are detected by an off-axis MCP detector mounted

at the spatial focus of the reflectron.

The third harmonic of a Nd:YAG laser (Spectra Physics, Inc., model Lab 130–50) used in the experiment gives 355 nm, 15 mJ nanosecond pulses at a repetition rate of 50 Hz. The laser beam is brought to a 5 mm diameter spot size inside the vacuum chamber. The ionic photofragments arising from the mass-selected parent anions are detected and analyzed as described in Chapter 2. The mass-spectra obtained by focusing the reflectron on the different fragments arising from the same parent ions are averaged for ~ 500 laser shots. They are then assembled into a combined mass-spectrum representing all observed fragmentation channels of the parent ion studied.

4.3 Results

A typical mass-spectrum for the $\text{CO}_2^-(\text{H}_2\text{O})_m$ parent-ions is shown in Figure 4.1. The observed intensity pattern is consistent with the previous report by Tsukuda and Nagata [101]. No $(\text{H}_2\text{O})_n^-$ clusters were observed simultaneously in the mass spectra, being consistent with results of Bondybey and co-workers who reported that $(\text{H}_2\text{O})_n^-$ clusters anions react quickly with a CO_2 molecule to form $\text{CO}_2^-(\text{H}_2\text{O})_{n-x}$ anions, where $x = 2-3$ is the number of evaporated water molecules. Our $\text{CO}_2^-(\text{H}_2\text{O})_m$ cluster anions could be formed by this mechanism in combination with electron attachment to $[\text{CO}_2(\text{H}_2\text{O})_p]$ neutral clusters with $p > m$. Theoretical results show that the bent CO_2^- core prefers a surface solvation arrangement as shown in the insert in Figure 4.1.

The photofragment-ion mass-spectra obtained from mass-selected $\text{CO}_2^-(\text{H}_2\text{O})_m$, $m = 3-20$ clusters at 355 nm are shown in Figure 4.2. These spectra are normalized to the same maximum intensity, therefore the peak heights are not representative of

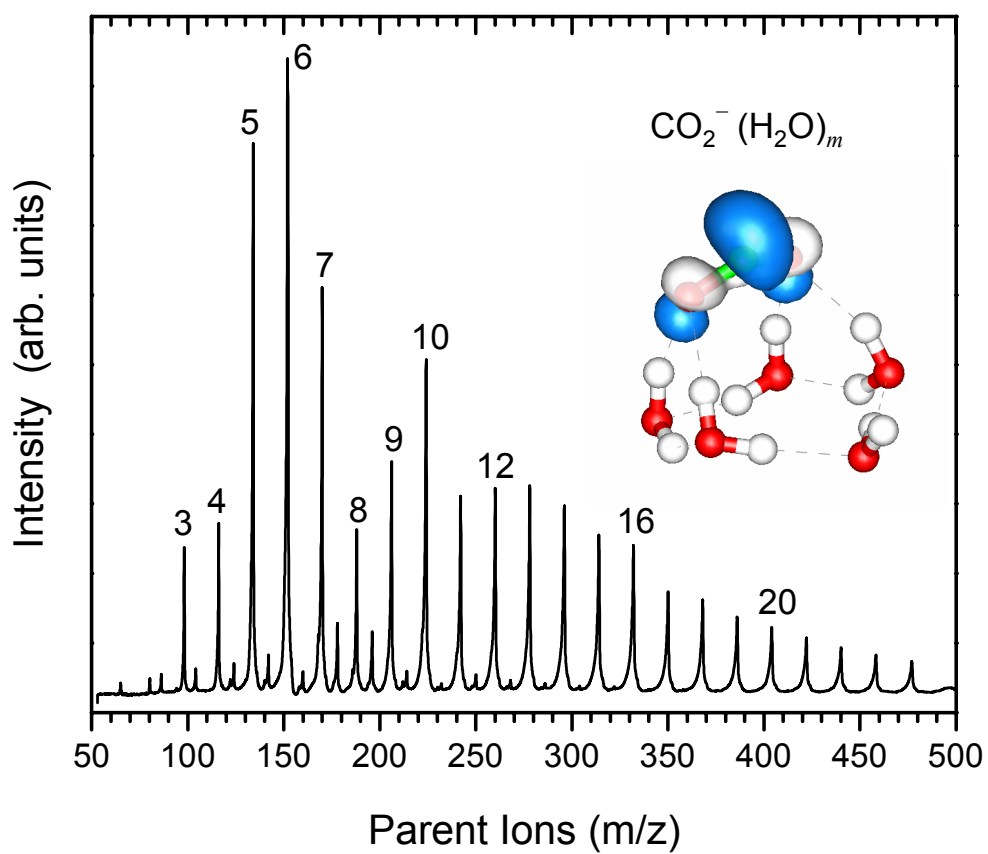
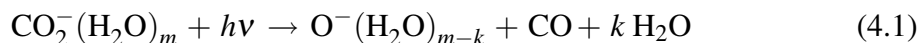


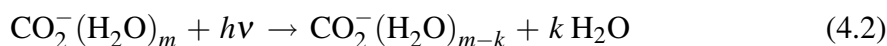
Figure 4.1: Mass spectrum of parent $\text{CO}_2^- (\text{H}_2\text{O})_m$ cluster anions. The insert shows the $\text{CO}_2^- (\text{H}_2\text{O})_5$ anion and its HOMO based on the structures given by Balaj et al. [93].

the corresponding absolute cross-sections. However, relative yields for the different channels can be obtained by comparing the integrated intensities of the various peaks for a particular m as shown in Figure 4.3. We verified that the integrated peak intensities for selected fragment ions scale linearly with laser power, confirming the one-photon nature of the transitions. No anionic fragmentation of $\text{CO}_2^-(\text{H}_2\text{O})_m$ was observed at 532 nm and our photofragmentation results at 266 nm are reported elsewhere [85, 100].

The 355 nm spectra displayed in Figure 4.2 reveal two types of fragment anions: (1) $\text{O}^-(\text{H}_2\text{O})_{m-k}$, $1 \leq k \leq 3$, and (2) $\text{CO}_2^-(\text{H}_2\text{O})_{m-k}$, $4 \leq k \leq 9$. No fragments of the $(\text{H}_2\text{O})_{m-k}^-$ form were observed. The appearance of $\text{O}^-(\text{H}_2\text{O})_{m-k}$ implies the dissociation of the CO_2^- core of the cluster, followed by the escape of CO and evaporation of k H_2O molecules. Namely,



We refer to the reaction pathways defined by Equation 4.1 as the core-dissociation channel. The $\text{CO}_2^-(\text{H}_2\text{O})_{m-k}$ fragments will be assigned as the water-evaporation channel, described as:



From Figure 4.2, it can be seen that fragmentation of the $\text{CO}_2^-(\text{H}_2\text{O})_m$, $m = 3-5$ cluster anions yields only core-dissociation products. As the parent cluster size is increased, the water-evaporation fragments make their first appearance at $m = 6$, with the smallest fragment of this type being $\text{CO}_2^- \cdot \text{H}_2\text{O}$ (no bare CO_2^- fragments are observed). With a further increase in m , the evaporation channel gradually becomes the dominant fragmentation pathway for $m = 8$. The branching ratio between channels 4.1 and 4.2 is summarized in Figure 4.3 as a function of the parent cluster size.

The average loss of water molecules in channel 4.1 is $\langle k \rangle = 1.0\text{--}2.5$, depending on the parent size. Channel 4.2 involves the average loss of $\langle k \rangle = 4.4$ to 7.5 water molecules. In both channels, $\langle k \rangle$ increases with m . In the large m asymptote, the number of evaporated water molecules plateaus at $\langle k \rangle = 2.47$ for the core-dissociation channel and at $\langle k \rangle = 7.45$ for the water evaporation channel (see also [85]). Assuming that the H₂O loss in the channel 4.2 accounts for the dissipation of the 355 nm photon energy, the average binding energy of one H₂O is calculated as 0.47 eV (45.35 kJ/mol), which agrees well with the 0.456 eV (43.98 kJ/mol) value corresponding to the heat of evaporation of bulk water [102]. The bond dissociation energy for hydrated CO₂⁻ can also be estimated by subtracting the average energy that is dissipated by evaporation of water molecules (for the core-dissociation channel) from the photon energy, resulting in a value of $\sim 2.4 \pm 0.2$ eV. In a later study (see Habteyes et al. [85]) we explored the photofragmentation of these clusters using 266 nm light up to 40 water molecules, where we obtained an enthalpy of evaporation for a water molecule of 0.466 ± 0.001 eV and a bond dissociation energy of 2.49 eV for the hydrated CO₂⁻ anion.

4.4 Discussion

Absorption of a near-UV photon by the negative CO₂⁻(H₂O)_{*m*} clusters can either lead to electron detachment or to the promotion to an excited anionic state. The core-dissociation channel 4.1 must involve the electronic excitation of the CO₂⁻ cluster core (chromophore). The water-evaporation channel, however, could be explained by three distinct mechanisms:

- (i) A photoevaporation process where the electronic excitation of the CO₂⁻ core is

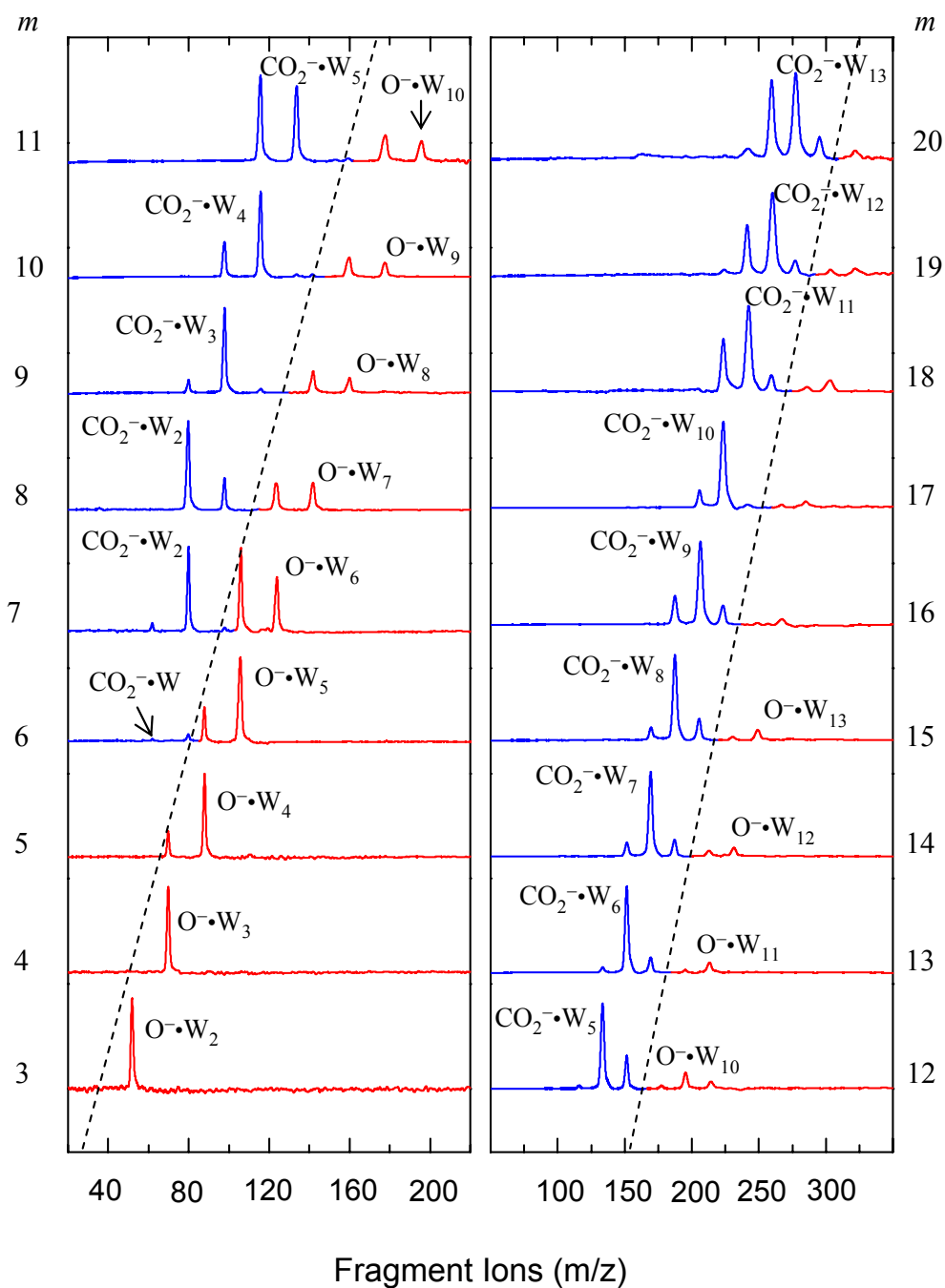


Figure 4.2: 355 nm photofragment mass spectrum for the $\text{CO}_2^-(\text{H}_2\text{O})_m$ cluster anions.

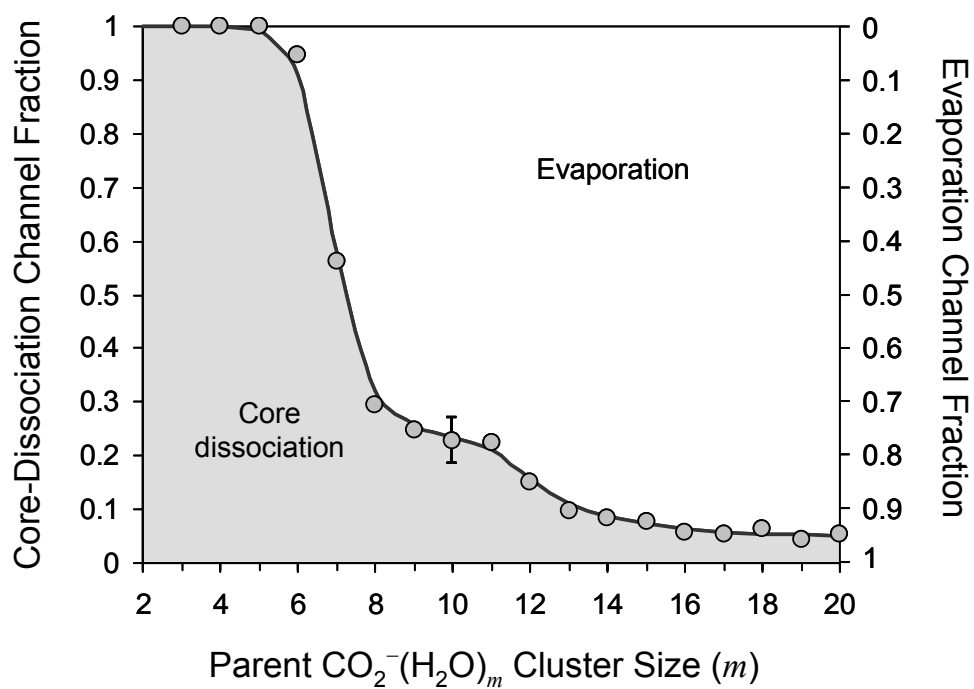


Figure 4.3: Branching ratio of the core-dissociation and water-evaporation fragments as a function of the parent cluster size.

followed by an energy transfer to inter-molecular degrees of freedom of the cluster. This excess energy is then dissipated via a sequential ejection of monomer solvents that persists until the cluster gets rid of the excess energy or of all its removable moieties.

- (ii) A strong interaction with the solvent causes the photodissociation of CO_2^- to be halted, forcing the O^- fragment to recombine with the CO fragment within the cluster (caging and recombination). The evaporation of solvent molecules from the cluster removes the excess energy generated by the recombination reaction, allowing the relaxation of the cluster core.
- (iii) A CTTS transition followed by the evaporation of several H_2O molecules. Since no $(\text{H}_2\text{O})_{m-k}^-$ fragments, corresponding to the loss of neutral CO_2 , are observed, a CTTS process is likely to be reversed by electron recapture by the CO_2 , possibly followed by further evaporation of solvent monomers.

The decrease in the fraction of core-dissociation fragments with increasing parent cluster size, seen in Figure 4.3, it is consistent with all of the above mechanisms.

4.4.1 Trapping of the excess electron on CO_2 : Stabilization by Hydration

In Chapter 3, we discussed the shallow potential well that traps the electron on a bent CO_2 host ($\angle\text{OCO} \approx 138^\circ$). The bending potential energy curves show that starting from the bent equilibrium position in the ground state and approaching linearity, there is a small barrier connected with a change in character of the anionic state from valence to diffuse. The diffuse bound state merges with the neutral curve at small bending angles providing

an open channel for electron autodetachment [44]. This results on the metastability of the CO_2^- anion, giving a lifetime on the order of $\sim 100 \mu\text{s}$ [54, 56, 44].

Klots [95] reported that the addition of a single water molecule was enough to prevent autodetachment in the TOF tube, giving a lifetime of at least 1 ms. An estimated lifetime of several milliseconds was given for the case of two water molecules solvating the CO_2^- anion. Photoelectron spectroscopic studies in the $\text{CO}_2^-(\text{H}_2\text{O})_m$ cluster series show that the anion is greatly stabilized by stepwise hydration [101, 94]. Increasing VDEs ranging from 1.4 eV for $m = 0$ to 3.46 eV for $m = 5$ have been reported [101]. Theoretical results (see Habteyes et al. [85]) show that the potential well that traps the CO_2^- anion state gets progressively stabilized by pushing down the energy of the anion relative to the neutral potential minimum (as evident from the VDEs). The height of the trapping barrier gets progressively increased as well and the bending angle of intersection with the neutral curve -if any- becomes closer to the linear geometry. The question of whether there is still an intersection with the diffuse state for larger hydrates remains, although this diffuse state also is expected to be somewhat stabilized by hydration as shown in the increasing VDEs obtained for hydrated electrons [60]. Another consequence of the stabilization by hydration is that excited electronic configurations may get stabilized too, bringing them from the realm of short-lived resonances to actual states opening new reaction pathways.

4.4.2 Core Dissociation Mechanism for the $\text{CO}_2^-(\text{H}_2\text{O})_m$ Clusters

Formation of O^- has long been observed by dissociative electron attachment to CO_2 both in the gas phase [103, 104, 105] and in condensed environments [106]. The process is understood in terms of a short-lived anion intermediate that undergoes dissociation into

stable $O^- + CO$ products. Of special interest to this work is the peak in the $e^- + CO_2$ dissociative attachment cross-section in the 4 eV range [104, 105]. In this energy range, the dissociative attachment occurs via the repulsive wall of the ${}^2\Pi_u$ shape resonance. For this ${}^2\Pi_u$ short-lived anion, the electron is temporarily trapped in the LUMO of CO_2 , and electron scattering studies locate its position at 3.8 eV over the neutral with an autodetachment lifetime of only a few femtoseconds (in the gas phase) [104, 63]. Its degeneracy is lifted when the molecule bends, splitting the ${}^2\Pi_u$ state into the 2A_1 and 2B_1 Renner-Teller components [43, 48]. A qualitative representation of these potential energy curves is shown in Chapter 3.

We have postulated that the excited states of CO_2^- are responsible for the photofragmentation of the $CO_2^-(H_2O)_m$ cluster anions via channel 4.1, with their participation in channel 4.2 being also possible. We will now focus on understanding the nature of the relevant states and the excited state dynamics leading to the dissociation of the CO_2^- core.

The UV absorption spectrum of CO_2^- in a crystalline matrix consists of three bands with maxima at 340, 280 and 250 nm [107]. The 340 nm band was also seen by Hartman and Hisatsune [108], slightly redshifted and peaking at 365 nm with a similar molar extinction coefficient ($\sim 100 \text{ L mol}^{-1} \text{ cm}^{-1}$). In aqueous solution, a strong band peaking at 250 nm was observed [96, 98], with a smaller low energy tail at about 340 nm attributed to a different transition [98]. The 340/365 nm band is attributed to a ${}^2B_1 \leftarrow X^2A_1$ transition. The 2B_1 corresponds to the upper branch of the Renner-Teller pair and is therefore of foremost importance for this study. The higher-energy absorption band corresponds to a ${}^2A_1 \leftarrow X^2A_1$ transition and photodissociation at this energy range has

also been observed and discussed in our later work (see Habteyes et al. [85]). From published thermochemistry data [109], the bond dissociation energy of CO_2^- in the gas phase is calculated as 3.46 ± 0.20 eV. From experimental values, a dissociation energy of 3.39 eV is obtained from the 5.453 eV corresponding to the value for $\text{CO}_2 \rightarrow \text{CO} + \text{O}(^3P)$ [110, 111], and the adiabatic electron affinities of 1.461 eV for $\text{O}(^3P)$ [112] and -0.6 eV for CO_2 [54]. The smaller dissociation value of 2.49 eV that we have obtained for the hydrated anion results from the difference between the water binding energies to the O^- core of the fragments compared to that of the CO_2^- parents. A similar “bond softening” effect was proposed for the dissociation of the ozonide anion O_3^- in water clusters [113].

Although the reaction dynamics of the solvated molecular ions cannot be understood exclusively in terms of the potential curves of the isolated core anion, these curves provide a starting point for discussion. Two possible mechanisms are suggested for the dissociation of CO_2^- in water clusters with 355 nm light:

- (i) Upon $[\text{CO-O}]^-$ stretching, the 2B_1 transforms as $^2A''$ for these lower (C_s) symmetry. Its potential energy curve correlates with a $\text{CO}^- + \text{O}$ channel that is much higher than the available energy. However, the $^2B_1 \leftarrow X^2A_1$ transition leaves CO_2^- with a high degree of bending excitation with the potential gradient directing the system towards linearity, where some of the population internally converts to the 2A_1 state by means of the Renner-Teller coupling. The $\text{O}^-(^2P) + \text{CO}$ dissociation products can therefore be formed on the $^2A_1/2A'$ state. Similar Renner-Teller mediated predissociation mechanisms have been implicated in other bent triatomic radicals, with HCO being the classical example [114, 115]. Some degree of competition with autodetachment is expected, especially for regions

where the bending angle is closer to the linear geometry for clusters with smaller number of water molecules.

- (ii) Recent calculations by Habteyes et al. [85] (see also [100]) suggest the presence of a higher repulsive state of ${}^2A_2/{}^2A''$ symmetry that intersects the ${}^2B_1/{}^2A''$ at a stretched, bent $[O-CO]^-$ geometry, leading directly into the $O^- + CO$ dissociative channel. The avoided crossing of the two ${}^2A''$ curves may produce a conical intersection where a barrier is formed separating the prepared ${}^2B_1/{}^2A''$ state from the dissociative part arising from the higher ${}^2A_2/{}^2A''$ excited state.

Finally, we now need to compare the fragmentation of the $CO_2^-(H_2O)_m$ anions to that of the homogeneous $(CO_2)_n^-$ cluster series. Lineberger and co-workers found that UV fragmentation of $(CO_2)_n^-$, $n = 13$ occurs via the sequential ejection of CO_2 monomers [74]. Intriguingly, the onset of this channel coincides, approximately, with the reverse core-switching from the monomer-based $CO_2^-(CO_2)_n$, $7 \leq n \leq 13$ clusters to dimer-based $(O_2CCO_2)^-(CO_2)_n$, $n > 13$ [80]. The $(CO_2)_{13}^-$ is believed to be a mix of the monomer and dimer-based structures. The dominant mechanism of $(CO_2)_n^-$, $n \leq 13$ dissociation likely involves the dissociation of the order-of-1/2 C-C bond in the covalently bound $(O_2CCO_2)^-$ dimer-anion [78], yielding $CO_2^- + CO_2$ (followed by the evaporation of some solvent CO_2 and perhaps recombination). Hence, even though the dissociation of the anionic core of the cluster does occur, the fragments are not distinguishable from the mere solvent evaporation. For $(CO_2)_n^-$, $6 \leq n \leq 13$ only a minor CO_3^- channel was observed [74, 84]. The CO_3^- products can be attributed to $CO_2^- \rightarrow O + CO$ dissociation followed by a bimolecular association reaction $O^- + CO_2 \rightarrow CO_3^-$. This channel is most relevant for comparison with $CO_2^-(H_2O)_m$. The ion-molecule association reaction is further explored

in the next Chapter, where a second CO₂ molecule is added to the CO₂⁻(H₂O)_m clusters.

4.5 Summary

In summary, the fragmentation of mass-selected CO₂⁻(H₂O)_m, $m = 3-20$ cluster anions at 355 nm yields two types of anionic products: O⁻(H₂O)_{m-k}, $1 \leq k \leq 3$, and CO₂⁻(H₂O)_{m-k}, $4 \leq k \leq 9$. The former dominate the fragmentation in the $m = 3-7$ range, while the latter take precedence for $m = 8-20$. The dissociation of CO₂⁻, responsible for the observed O⁻(H₂O)_{m-k} fragments, is proposed to proceed via a hydration-stabilized excited state, originating from a low-lying ²B₁ resonance in CO₂⁻. The ²B₁ state is vibrationally coupled to the lower ²A₁ state (where the dissociation is proposed to occur) by means of the Renner-Teller interaction. Hence, predissociation via the Renner-Teller interaction is proposed as the mechanism for the formation of the O⁻(H₂O)_{m-k} fragment anions. A second possible mechanism includes a conical intersection between the ²B₁/²A'' state and a higher ²A₂/²A'' state. Electronic excitation of CO₂⁻, followed by either a photoevaporation process, caging and recombination, or photoinduced electron transfer to solvent are suggested as possible triggers for the water evaporation channel.

CHAPTER 5

PHOTODETACHMENT AND PHOTOFRAGMENTATION PATHWAYS IN THE
[[CO₂]₂(H₂O)_m]⁻ CLUSTER ANIONS

5.1 Introduction

Many ionic clusters can be viewed as a charged core embedded in a “microsolution” consisting of a relatively small number of solvent molecules. This arrangement is helpful for studying reactions under well-defined microscopic conditions and understanding the structural motifs responsible for chemical reactivity. In this Chapter we focus on the [(CO₂)_n(H₂O)_m]⁻ cluster series, which has attracted much deserved attention due to its interesting structural and electronic properties as well as for its rich photochemistry. In particular, we look at the case of the (CO₂)₂⁻ dimer anion and its fate when placed in a water cluster.

5.1.1 The [(CO₂)_n(H₂O)_m]⁻ Cluster Series

Homogeneous and heterogeneous anionic clusters of carbon dioxide have long been known to exhibit interesting structural properties [116, 16, 74, 78, 79, 80, 81, 92, 83, 87, 86, 117]. The homogeneous cluster anions (CO₂)_n⁻ are discussed in detail in Chapter 3. In brief, for these clusters the excess electron either localizes on a single CO₂ monomeric component (type-I) or forms a covalent bond between two CO₂ monomers (type-II clusters) while the remaining molecules solvate the respective CO₂⁻ or (O₂CCO₂)⁻ core

anion [78, 79, 80, 83]. Stepwise solvation normally results in a gradual increase of the cluster vertical detachment energy (VDE). To the contrary, the well-documented case of $(\text{CO}_2)_n^-$ is characterized by sharp discontinuities in $\text{VDE}(n)$ between $n = 6$ and 7 and again between $n = 13$ and 14 [79, 80]. These discontinuities are attributed to “core switching” from $(\text{O}_2\text{CCO}_2)^-$ for $n < 6$ to CO_2^- for $6 < n < 13$ [79]. A reverse switch of the core anion structure back to $(\text{O}_2\text{CCO}_2)^-$ is observed for $n > 13$ [80]. Johnson and co-workers traced the origin of this phenomenon to the effect of solvent asymmetry [83]. Even though the most stable form of $(\text{CO}_2)_2^-$ corresponds to $(\text{O}_2\text{CCO}_2)^-$ rather than $\text{CO}_2^- \cdot \text{CO}_2$, an incomplete (asymmetric) solvation shell in the $n = 6$ –13 range causes one of the monomeric constituents of the dimer anion to be preferentially stabilized [79, 80, 83].

Heterogeneous clusters $[(\text{CO}_2)_n(\text{H}_2\text{O})_m]^-$ present a more complex scenario, where the distinct molecular constituents, CO_2 and H_2O , may in principle compete for the excess electron. Photoelectron spectroscopy and theory suggest that the charge remains localized on the carbon dioxide part of the cluster, either in a monomer or dimer anion configuration [81, 92, 94, 117]. However, in the presence of H_2O , the core switching follows a different trend compared to $(\text{CO}_2)_n^-$ [94]. A key feature of $[(\text{CO}_2)_n(\text{H}_2\text{O})_m]^-$ observed in our group’s imaging experiments is the loss of photodetachment anisotropy with increasing hydration (in the 400 nm photodetachment [94]). This observation was attributed to autodetachment, but the exact nature of the excited states involved remained unclear.

5.1.2 Decay Channels for Excited Clusters

In addition to photodetachment, or autodetachment, cluster fragmentation is an alternative route for excited-state dynamics. Hence, the fragmentation studies are as important for understanding the cluster structure, particularly the nature of the excited states.

Photofragmentation of $(\text{CO}_2)_n^-$ was observed mainly in the $n > 13$ range, yielding $(\text{CO}_2)_k$, $k < n$ fragment anions. These fragmentation channels are presumably triggered either by the photodissociation of the $(\text{O}_2\text{CCO}_2)^-$ cluster core to $\text{CO}_2^- + \text{CO}_2$ or by photoinduced electron transfer to the solvent shell.

The recent photofragmentation results for $\text{CO}_2^-(\text{H}_2\text{O})_m$ contrasted the homogeneous anionic clusters of CO_2 in that one of the dominant pathways involved the dissociation of hydrated CO_2^- to $\text{O}^- + \text{CO}$ [118]. The dissociation process can be understood in connection with the $^2\Pi_u$ shape resonance seen in dissociative electron attachment to CO_2 near 4.4 eV [104, 105, 119, 120, 121, 122, 123]. According to the proposed mechanism [118], the 355 nm laser photon is absorbed by the CO_2^- cluster core, for which both the direct and indirect electron detachment are suppressed by the hydration interactions. The solvent-induced stabilization of the excited anion allows the bond dissociation to occur via a nonadiabatic bending process mediated by the Renner-Teller effect.

The nascent O^- radical anion formed in the dissociation of hydrated CO_2^- is expected to be highly reactive and clusters are a perfect environment to investigate its reactivity in detail. This premise motivates, in part, our present experiment, where we introduce an additional CO_2 in the hydrated cluster based on a CO_2^- core and observe its exothermic and barrierless reaction with nascent O^- . There have been few reports of reactions of nascent photofragments within anionic clusters [74, 84, 124]. The $\text{O}^- + \text{CO}_2 \rightarrow \text{CO}_3^-$

reaction was first observed in electron bombardment of van der Waals clusters of CO_2 [16, 70, 125]. The CO_3^- peak in the electron attachment spectrum appears at 4.4 eV [70], indicating that the attachment proceeds via a dissociative capture by the $^2\Pi_u$ resonance of CO_2 . Alexander et al. [74] ascribed a similar process to the minor CO_3^- channel in the fragmentation of $(\text{CO}_2)_n^-$, $6 < n < 13$. Johnson and coworkers investigated the reaction of O^- with H_2O following the photodissociation of O_2^- within the $\text{O}_2^- \cdot \text{H}_2\text{O}$ complex at energies sufficient for overcoming the reaction barrier [124].

5.1.3 A Hydrated Dimer Anion?

The addition of another CO_2 to $\text{CO}_2^-(\text{H}_2\text{O})_m$ raises several questions. First, the nature of the ionic core of the $[(\text{CO}_2)_2(\text{H}_2\text{O})_m]^-$ clusters must be determined. From the previous work, we anticipate the excess electron to reside on the CO_2 domain [94], but whether the core of the cluster is a monomer or a dimer anion of CO_2 remains to be seen. Assuming the electron is on a single CO_2 , the competition of H_2O and the second (neutral) CO_2 for the binding sites in the proximity of the charged cluster core must be addressed.

In this chapter we utilize a combination of photoelectron imaging and photofragment mass-spectroscopy to investigate the structure and reactivity of $[(\text{CO}_2)_n(\text{H}_2\text{O})_m]^-$. The imaging experiments on $m = 2-6$ clusters expand the previous work on selected $[(\text{CO}_2)_n(\text{H}_2\text{O})_m]^-$ cluster anions [94], in which only one of the species covered here, $m = 2$, was studied. The analysis of the photoelectron images sheds light on the coexistence of the CO_2^- and $(\text{O}_2\text{CCO}_2)^-$ based clusters. The anionic fragmentation pathways observed by tandem time-of-flight mass-spectroscopy for $m = 3-11$ illuminate the reactivity of the clusters and provide further insights into the structure of their anionic

cores. Most importantly, the heterogeneous $[(\text{CO}_2)_2(\text{H}_2\text{O})_m]^-$ cluster anions allow the study of two types of photoinitiated reactions: the dissociation of a solvation-stabilized core anion and the secondary ion-molecule reaction of nascent photofragments with the solvent molecules.

5.2 Experiment

The details of the experimental apparatus are presented in Chapter 2. Preparation of the $[(\text{CO}_2)_n(\text{H}_2\text{O})_m]^-$ clusters involves expansion of undried CO_2 into the ion source chamber (base pressure of 2×10^{-7} Torr) through a pulsed supersonic nozzle (General Valve Series 99) operated at 3.5-4 atm stagnation pressure and a 50 Hz repetition rate. In addition to the CO_2 gas impurities, water trapped within the gas delivery lines serves as a source of H_2O . A continuous 1 keV electron beam crosses the free jet a few millimeters downstream from the 800 μm diameter valve orifice. The cluster anions are formed by slow secondary electron attachment to neutral clusters and pulse-extracted into a ~ 2.3 m long flight tube of a Wiley-McLaren [126] type TOF mass-spectrometer.

The third harmonic of a nanosecond Nd:YAG laser (Spectra Physics, Inc., model Lab 130-50) is used in these experiments, providing 355 nm, 15 mJ pulses at a repetition rate of 50 Hz. The laser beam is brought to a 5 mm diameter spot at the intersection with the mass-selected ions.

Photoelectron images are recorded by collecting the electrons in a direction perpendicular to both the ion and the laser beams. A 40 mm diameter microchannel plate with a P47 phosphor screen (Burle, Inc.) is mounted at the end of the electron flight tube shielded with μ -metal. Images are collected by a CCD camera (Dalsa, Inc.) in an event

counting mode for 10,000 to 30,000 experimental cycles. To discriminate against noise, the MCPs are operated in a pulsed-bias mode. The procedure for obtaining photofragment mass spectra is described in Chapter 2. The signals from each photofragment are recorded and averaged by the digitizing oscilloscope for about 512 laser shots, transferred to a computer, and integrated afterward for relative yield determination.

5.3 Results and Analysis

A typical parent-ion mass spectrum observed in this work is shown in Figure 5.1. The most intense peak progression corresponds to the $\text{CO}_2^-(\text{H}_2\text{O})_m$ cluster anions [118], interspersed with less intense $[(\text{CO}_2)_2(\text{H}_2\text{O})_m]^-$ peaks. Detectable but poorly resolved contributions of the $[(\text{CO}_2)_n(\text{H}_2\text{O})_m]^-$, $n = 3$ and 4 clusters are also seen. The formation of the $n = 2$ cluster anions was optimized by adjusting the precursor gas backing pressure.

5.3.1 Photoelectron Images and Cluster Structure

Figure 5.2 (left column) shows the photoelectron images of the $[(\text{CO}_2)_2(\text{H}_2\text{O})_m]^-$, $m = 2-6$ cluster anions collected at 355 nm. All images shown were recorded under the same velocity-mapping conditions. Similar to the $\text{CO}_2^-(\text{H}_2\text{O})_m$, $m = 2-6$ clusters [94], the $[(\text{CO}_2)_2(\text{H}_2\text{O})_m]^-$, $m = 2-6$ photoelectron images are anisotropic in the limit of small m , gradually becoming more isotropic as the number of H_2O 's in the cluster increases. In this work, we focus mainly on the photoelectron energy spectra, extracted from the images using the Basis Set EXpansion (BASEX) Abel-inversion algorithm of Dribinski et al. [26]. The spectra are shown in the right column in Figure 5.2. The $m = 4-6$ spectra contain one broad photoelectron band, while the $m = 2$ spectrum includes two overlapping

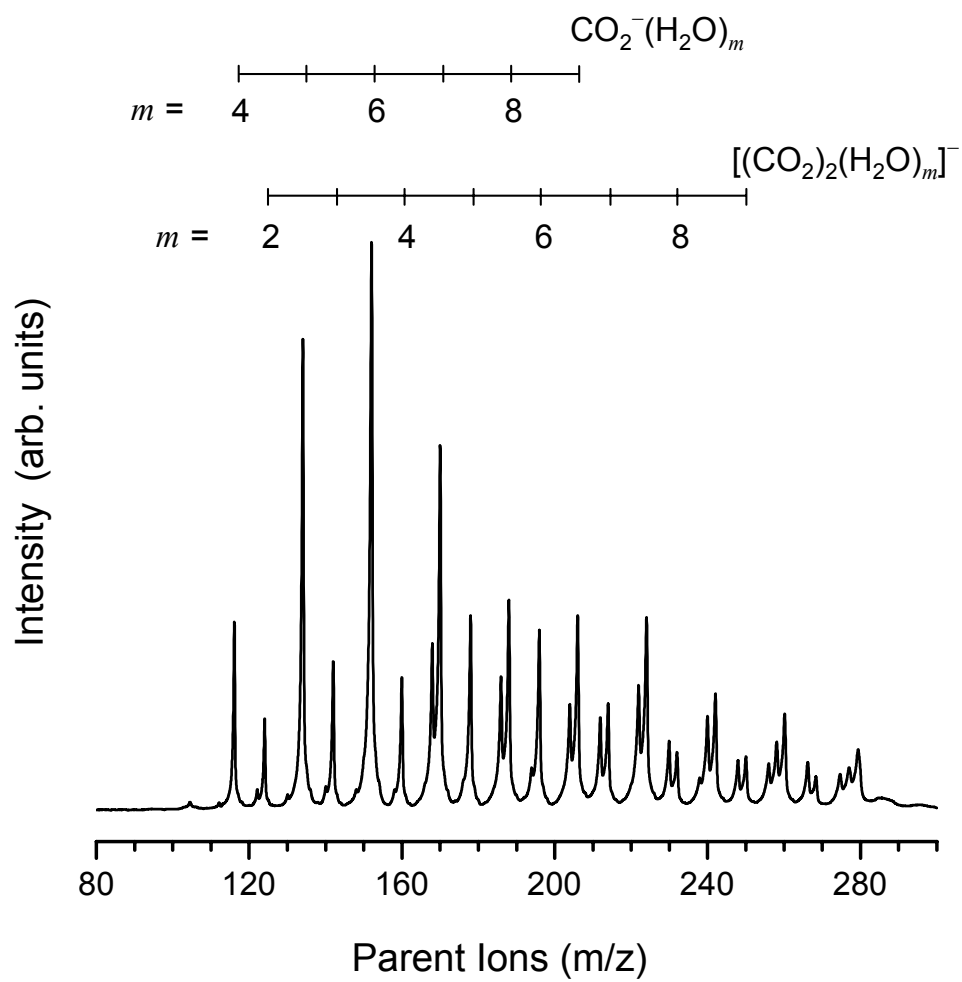


Figure 5.1: Representative mass spectrum of parent $[(\text{CO}_2)_2(\text{H}_2\text{O})_m]^-$ cluster anions.

transitions. The $m = 3$ spectrum exhibits a single maximum; nonetheless, the low-eKE shoulder is suggestive of a second transition close to $eKE = 0$.

We choose to characterize the photoelectron spectra in terms of the electron binding energy parameter, eBE_{max} , which corresponds to the eBE value for each observed band's maximum. For accurate determination of the peak positions, the photoelectron bands are modeled using the following modified Gaussian profiles:

$$P(eKE) = A eKE^{1/2} \exp[-(h\nu - eKE - VDE)^2/w^2]. \quad (5.1)$$

Here, $h\nu$ is the 355 nm photon energy (3.49 eV), VDE and w are the adjustable parameters corresponding to the vertical detachment energy and the Franck-Condon width of the bands, and A is a normalization factor. The model function in Equation 5.1 reflects the assumptions of the Franck-Condon model, within which the photodetachment cross-section is given by: $\sigma = Ch\nu v_e |\mathbf{M}_{\mathbf{q}}|^2$, where v_e is the asymptotic electron velocity, $\mathbf{M}_{\mathbf{q}}$ is the transition dipole moment as a function of nuclear coordinates \mathbf{q} (its absolute value squared corresponds to the Franck-Condon factor), and C is a combination of fundamental constants [127, 128]. The Gaussian function in Equation 5.1 models the Franck-Condon envelope of the photodetachment transition, while $eKE^{1/2}$ corresponds to the photoelectron velocity (speed).

At the fundamental level, the velocity factor in Equation 5.1 reflects the phase-space scaling of the number of the free-electron final states. This factor is often disregarded in Franck-Condon modeling of photoelectron spectra, when $eKE^{1/2}$ varies little in the spectral range of interest. Imaging, contrary to traditional photoelectron spectroscopy, emphasizes the low-eKE regime, where the variation in the final electron velocity is important. In a more general sense, the $eKE^{1/2}$ factor in Equation 5.1 corresponds to the

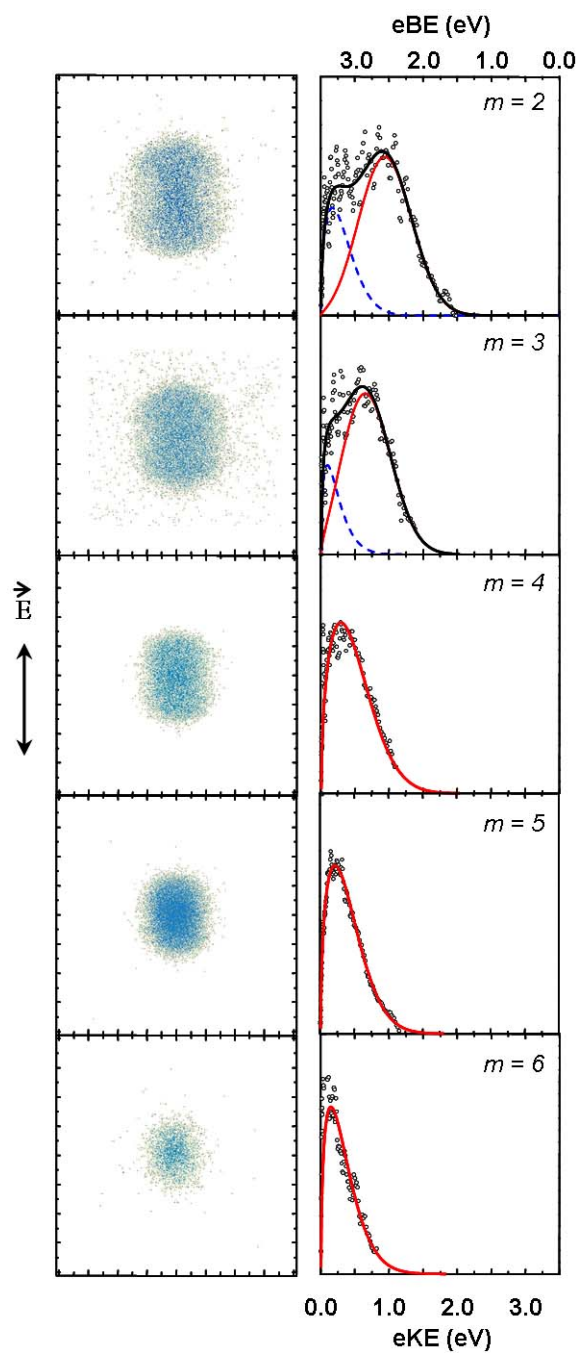


Figure 5.2: Photoelectron images (left) and corresponding photoelectron spectra (right) of the $[(\text{CO}_2)_2(\text{H}_2\text{O})_m]^-$, $m = 2-6$, cluster anions recorded at 355 nm. All photoelectron images are obtained under similar experimental conditions and shown to scale. The laser polarization is indicated by the double arrow in the left. In the right column, the experimental spectra are fitted by a sum (bold line) of contribution from type-I (solid) and type-II (dashed) parent clusters.

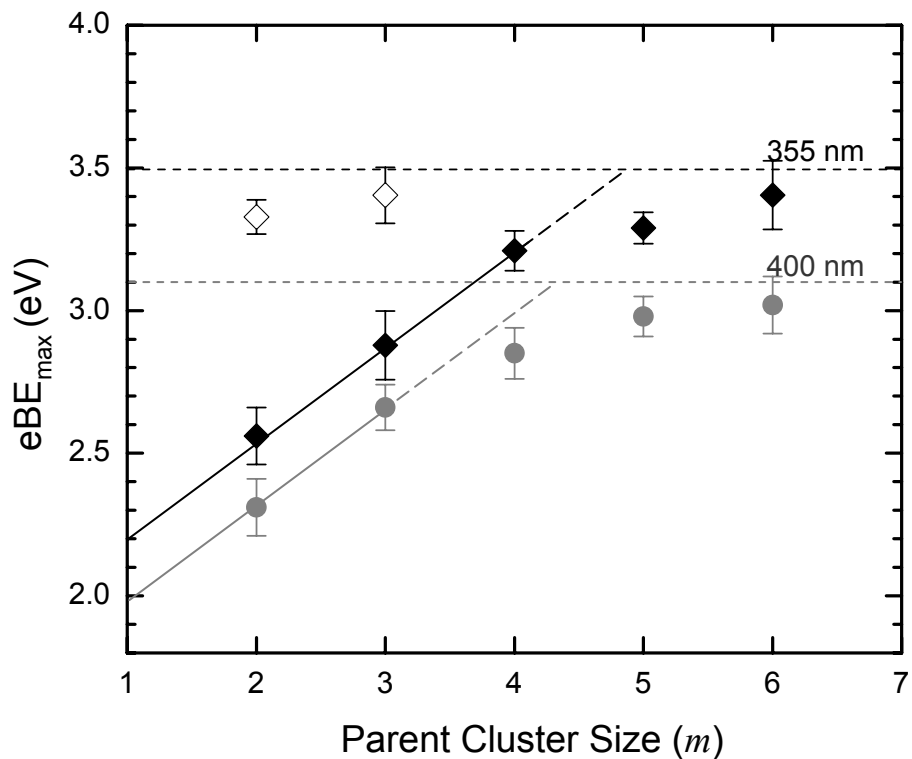


Figure 5.3: The eBE_{\max} values (defined in the text) for photoelectron bands arising from the dimer-based (open diamonds) and monomer-based (solid diamonds) $[(CO_2)_2(H_2O)_m]^-$ clusters at 355 nm. The corresponding values for $CO_2^-(H_2O)_m$ obtained at 400 nm [94] are also shown for comparison (gray circles). Linear trends for $eBE_{\max}(m)$ are indicated in the small m limit, where $eBE_{\max} \approx VDE$. The dashed horizontal lines indicate the 355 and 400 nm photon energies.

$\ell = 0$ limit of the Wigner law for the photodetachment of negative ions [30]. This limit corresponds to the lack of a centrifugal barrier to electron detachment, while inclusion of the angular momentum effects gives rise to the more general $eKE^{\ell+1/2}$ scaling of the cross-section. In the photodetachment processes considered here, we expect contributions from partial waves with different ℓ values. The importance of the $\ell > 0$ waves is particularly clear from the anisotropic nature of the photoelectron images in Figure 5.2. Hence, the $eKE^{1/2}$ factor in Equation 5.1 is an approximation. Nonetheless, it suffices our goals, because the determination of eBE_{\max} is not sensitive to the exact functional form of the model spectra, provided they yield a good agreement with the data.

The fits to the experimental spectra using Equation 5.1 are shown in Figure 5.2. For $m = 2$ and 3, superpositions of two modified Gaussians with independently adjustable A , VDE and w were used to achieve adequate agreement with the experiment. For $m = 4-6$, one model function was used in each case. The values of eBE_{\max} are determined at the maximum of each individual model band and the results are plotted as a function of m in Figure 5.3.

The eBE_{\max} values are generally distinct from the corresponding VDEs: the former indicate the peak positions, while the latter correspond to the maximum of the Franck-Condon envelope. Although the VDEs are often more relevant, their determination by modeling experimental spectra may be strongly dependent on the assumed scaling of the pre-Gaussian factor in Equation 5.1, especially for bands with $VDE > h\nu$. For this reason, we use peak positions (eBE_{\max}) as a more robust way to characterize the photoelectron spectra.

The eBE_{\max} values represent the lower bounds for the corresponding VDEs. In

the limit of $h\nu \gg \text{VDE}$, the spectral bands peak near the corresponding VDE and therefore $e\text{BE}_{\text{max}} \approx \text{VDE}$. When VDE nears the photon energy and particularly when $h\nu \leq \text{VDE}$, the observed spectral maximum lies necessarily below the vertical transition energy, yielding $e\text{BE}_{\text{max}} < \text{VDE}$. In Figure 5.3, linear slopes of the $e\text{BE}_{\text{max}}(m)$ data are shown in the small m limit, where they reflect the stabilizing effect of hydration. As m increases, the corresponding $e\text{BE}_{\text{max}}$ values level off, asymptotically approaching the photon energy. The two different 355 nm $e\text{BE}_{\text{max}}$ values for $m = 1$ and 2 correspond to two different modified-Gaussian bands used to model the corresponding photoelectron spectra in Figure 5.2. Following the previous studies of carbon dioxide based cluster anions [79, 80, 81, 87], these bands are assigned to two different core anion structures.

5.3.2 Photofragment-Ion Mass Spectra

The 355 nm photofragment mass-spectra obtained for the mass-selected $[(\text{CO}_2)_2(\text{H}_2\text{O})_m]^-$, $m = 3-11$ parent ions are shown in Figure 5.4 along with the assignment of the fragment-ion peaks. Only a very small CO_3^- signal was observed for the $m = 2$ cluster, whose photodestruction is dominated by electron detachment. The fragmentation of $[(\text{CO}_2)_2(\text{H}_2\text{O})_3]^-$ at 355 nm also occurs in acute competition with photodetachment, as evidenced by the relatively small yield of the anionic photofragments compared to total photodepletion. This is reflected in the poor signal-to-noise ratio of the $m = 3$ spectrum in Figure 5.4, compared to larger parent clusters. As the parent cluster size increases, the photodetachment becomes less energetically favorable, gradually giving way to the anionic fragmentation.

The spectra in Figure 5.4 reveal three types of photofragments: (i) $\text{CO}_2^-(\text{H}_2\text{O})_k$;

(ii) $\text{O}^-(\text{H}_2\text{O})_k$; (iii) $\text{CO}_3^-(\text{H}_2\text{O})_k$. Analogues of channels (i) and (ii), described as the evaporation and core-dissociation channels, respectively, were seen previously in $\text{CO}_2^-(\text{H}_2\text{O})_m$ [118]. Channel (iii) is new compared to $\text{CO}_2^-(\text{H}_2\text{O})_m$ and attributed to a sequential process: the dissociation of the CO_2^- cluster core to $\text{O}^- + \text{CO}$, followed by the association of nascent O^- with neutral CO_2 in the presence of H_2O . It is intriguing that type (iii) fragments appear only from the $m = 3-6$ parent clusters. For comparison, only minor signatures of a similar process were seen previously in $(\text{CO}_2)_n^-$, $6 \leq n \leq 13$ [74, 129, 84]. The anionic photofragments resulting from the mass-selected parent clusters are summarized in Table 5.1. The parent size-dependent fragmentation patterns are analyzed in terms of the relative (fractional) yields of individual photofragments. The yields were calculated by integrating the corresponding peak areas in the fragment mass-spectra and normalizing the combined signal for a given parent size (m) to unity. The resulting fractions are given in Table 5.1 in italics and in parentheses.

5.4 Discussion

5.4.1 Charge Localization in $[(\text{CO}_2)_2(\text{H}_2\text{O})_m]^-$, $m = 2-11$

The previous photoelectron imaging study of selected $[(\text{CO}_2)_n(\text{H}_2\text{O})_m]^-$, $n = 1-12$, $m = 0-6$ cluster anions, supported by theoretical calculations, indicated that the excess electron in these clusters is localized on carbon dioxide [94]. The parent mass spectrum obtained in the present work is consistent with this conclusion. Indeed, the most intense progression in Figure 5.1 corresponds to $[\text{CO}_2(\text{H}_2\text{O})_m]^-$, followed by $[(\text{CO}_2)_2(\text{H}_2\text{O})_m]^-$, while no hydrated electron clusters $(\text{H}_2\text{O})_m^-$ are formed under the same experimental conditions. Hence, CO_2 appears to act as an electron binding site in the observed clusters.

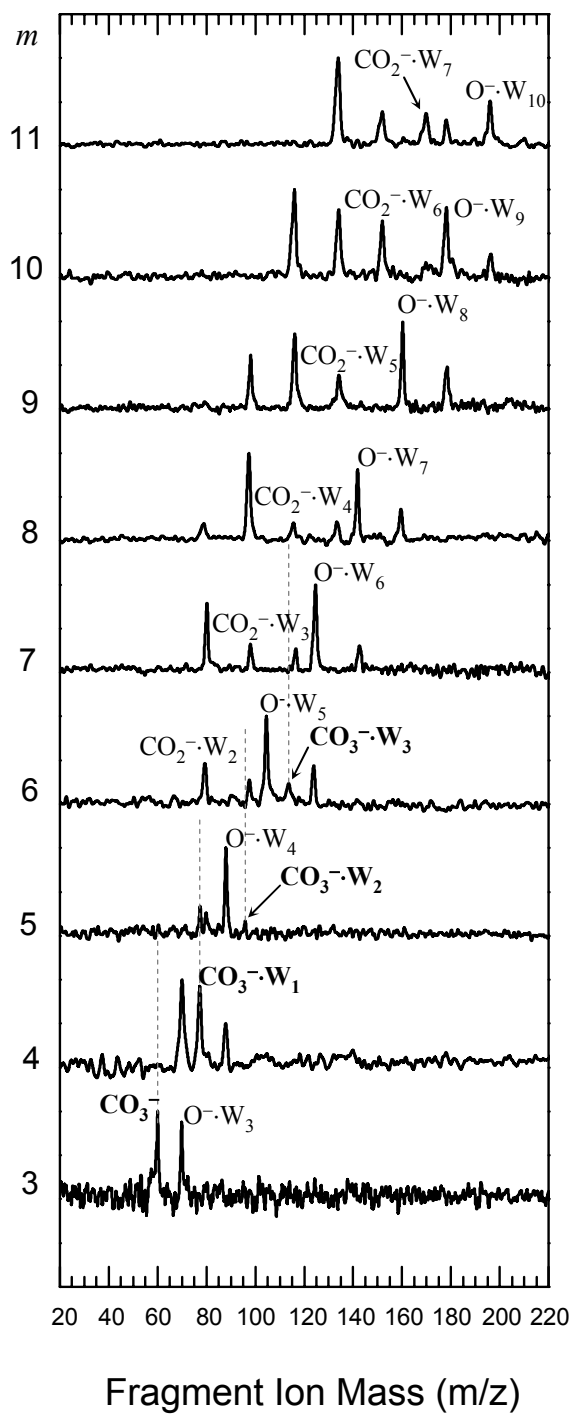


Figure 5.4: Photofragment mass spectra obtained from $[(\text{CO}_2)_2(\text{H}_2\text{O})_m]^-$, $m = 3$ – 11 , cluster anions at 355 nm. $\text{W} \equiv \text{H}_2\text{O}$.

Table 5.1: Anionic photofragments of mass-selected $[(\text{CO}_2)_2(\text{H}_2\text{O})_m]^-$, $m = 3-11$ parent clusters observed at 355 nm. The italicized values in parenthesis represent the fractional yields of the corresponding fragments.

Parent size (m)	Photofragments		
	Type (i)	Type (ii)	Type (iii)
3	...	$\text{O}^-(\text{H}_2\text{O})_3$ (0.47)	CO_3^- (0.53)
4	...	$\text{O}^-(\text{H}_2\text{O})_3$ (0.52) $\text{O}^-(\text{H}_2\text{O})_4$ (0.13)	$\text{CO}_3^-(\text{H}_2\text{O})$ (0.35)
5	$\text{CO}_2^-(\text{H}_2\text{O})_2$ (0.15)	$\text{O}^-(\text{H}_2\text{O})_4$ (0.64)	$\text{CO}_3^-(\text{H}_2\text{O})$ (0.15) $\text{CO}_3^-(\text{H}_2\text{O})_2$ (0.06)
6	$\text{CO}_2^-(\text{H}_2\text{O})_2$ (0.18) $\text{CO}_2^-(\text{H}_2\text{O})_3$ (0.10)	$\text{O}^-(\text{H}_2\text{O})_5$ (0.45) $\text{O}^-(\text{H}_2\text{O})_6$ (0.16)	$\text{CO}_3^-(\text{H}_2\text{O})_3$ (0.11)
7	$\text{CO}_2^-(\text{H}_2\text{O})_2$ (0.24) $\text{CO}_2^-(\text{H}_2\text{O})_3$ (0.11) $\text{CO}_2^-(\text{H}_2\text{O})_4$ (0.09)	$\text{O}^-(\text{H}_2\text{O})_6$ (0.43) $\text{O}^-(\text{H}_2\text{O})_7$ (0.14)	...
8	$\text{CO}_2^-(\text{H}_2\text{O})_2$ (0.09) $\text{CO}_2^-(\text{H}_2\text{O})_3$ (0.05) $\text{CO}_2^-(\text{H}_2\text{O})_4$ (0.05) $\text{CO}_2^-(\text{H}_2\text{O})_5$ (0.07)	$\text{O}^-(\text{H}_2\text{O})_7$ (0.26) $\text{O}^-(\text{H}_2\text{O})_8$ (0.15)	...
9	$\text{CO}_2^-(\text{H}_2\text{O})_3$ (0.16) $\text{CO}_2^-(\text{H}_2\text{O})_4$ (0.30) $\text{CO}_2^-(\text{H}_2\text{O})_5$ (0.14)	$\text{O}^-(\text{H}_2\text{O})_7$ (0.02) $\text{O}^-(\text{H}_2\text{O})_8$ (0.24) $\text{O}^-(\text{H}_2\text{O})_9$ (0.15)	...
10	$\text{CO}_2^-(\text{H}_2\text{O})_4$ (0.29) $\text{CO}_2^-(\text{H}_2\text{O})_5$ (0.21) $\text{CO}_2^-(\text{H}_2\text{O})_6$ (0.17) $\text{CO}_2^-(\text{H}_2\text{O})_7$ (0.04)	$\text{O}^-(\text{H}_2\text{O})_9$ (0.22) $\text{O}^-(\text{H}_2\text{O})_{10}$ (0.08)	...
11	$\text{CO}_2^-(\text{H}_2\text{O})_5$ (0.41) $\text{CO}_2^-(\text{H}_2\text{O})_6$ (0.13) $\text{CO}_2^-(\text{H}_2\text{O})_7$ (0.16)	$\text{O}^-(\text{H}_2\text{O})_9$ (0.09) $\text{O}^-(\text{H}_2\text{O})_{10}$ (0.21)	...

This still leaves open two possibilities for charge localization in $[(\text{CO}_2)_2(\text{H}_2\text{O})_m]^-$: the excess electron may be bound to a single CO_2 (type-I clusters) or shared between two CO_2 moieties (type-II clusters). It is well established both experimentally and theoretically that the most stable form of $(\text{CO}_2)_2^-$ is a type-II covalent dimer anion $(\text{O}_2\text{CCO}_2)^-$ [78, 79]. However, the core anion structure in clusters containing at least two CO_2 moieties varies from type-I to type-II depending on the balance between the stability of the core and solvation energetics. A prime example of such structural variation is the core switching phenomenon in $(\text{CO}_2)_n^-$ [79, 80, 83].

Of the $[(\text{CO}_2)_2(\text{H}_2\text{O})_m]^-$ cluster anions, only the $m = 2$ and 3 clusters were examined previously by photoelectron imaging at 400 nm [94]. The experiments indicated that the $m = 2$ clusters have a major contribution from the $(\text{O}_2\text{CCO}_2)^-$ core type, which is followed by a switch to predominantly CO_2^- core structures for $m = 3$. In the experiments reported here, the higher-energy 355 nm photons enabled us to image higher binding energy electrons and expand the measurements to larger clusters, containing up to 6 water molecules. The binding energies corresponding to the observed transition maxima, $e\text{BE}_{\text{max}}$, are plotted in Figure 5.3. For $m = 2$ and 3, two different $e\text{BE}_{\text{max}}$ values are obtained, corresponding to two different photodetachment bands. These are attributed to the type-I (solid diamonds) and type-II (open diamonds) parent clusters, described as $\text{CO}_2^-(\text{H}_2\text{O})_m\text{CO}_2$ and $(\text{O}_2\text{CCO}_2)^-(\text{H}_2\text{O})_m$, respectively.

The assignment of the lower- $e\text{BE}_{\text{max}}$ curve in Figure 5.3 (solid diamonds) to type-I $\text{CO}_2^-(\text{H}_2\text{O})_m\text{CO}_2$ cluster anions is helped by comparison with the corresponding values obtained previously for $\text{CO}_2^-(\text{H}_2\text{O})_m$, $m = 2-6$ at 400 nm shown by grey solid circles [94]. Provided the $e\text{BE}_{\text{max}}$ values are significantly smaller than the respective 355

or 400 nm photon energies, the type-I $[(\text{CO}_2)_2(\text{H}_2\text{O})_m]^-$ and $\text{CO}_2^-(\text{H}_2\text{O})_m$ trends are similar, shifted by approximately 0.2 eV, which corresponds to the stabilization by an extra CO_2 in the $[(\text{CO}_2)_2(\text{H}_2\text{O})_m]^-$ case. The similar slopes of the two curves correspond to the stabilization energy of additional water molecules. We therefore interpret the $[(\text{CO}_2)_2(\text{H}_2\text{O})_m]^-$ data indicated by solid diamonds as corresponding to $\text{CO}_2^-(\text{H}_2\text{O})_m\text{CO}_2$ structures, where the additional CO_2 solvates the mostly unchanged $\text{CO}_2^-(\text{H}_2\text{O})$ sub-structure.

The higher $e\text{BE}_{\text{max}}$ values for the type-II $[(\text{CO}_2)_2(\text{H}_2\text{O})_m]^-$, $m = 2$ and 3 clusters are so close to the 3.49 eV photon energy that the corresponding VDEs are likely to be in excess of $h\nu$. With increasing m , the photodetachment of these clusters becomes energetically inaccessible at the laser wavelength used. Therefore, even though no type-II bands were used in modeling the $m \geq 4$ photoelectron spectra in Figure 5.2, we cannot completely rule out the presence of the type-II component in the parent cluster ion beam based on the photoelectron data alone.

Considering the fragmentation results in Section 5.3.2, we note that two of the three types of photofragment anions, namely, type (ii) $\text{O}^-(\text{H}_2\text{O})_k$ and type (iii) $\text{CO}_3^-(\text{H}_2\text{O})_k$, are inconsistent with type-II $(\text{O}_2\text{CCO}_2)^-(\text{H}_2\text{O})_m$ parent structures. The $\text{O}^-(\text{H}_2\text{O})_k$ channel in $(\text{O}_2\text{CCO}_2)^-(\text{H}_2\text{O})_m$ is ruled out, because the dissociation of $(\text{O}_2\text{CCO}_2)^-$ is expected to first cleave its weakest (order-of-1/2) C–C bond, yielding the CO_2^- rather than O^- fragment anions. The CO_3^- channel in type-II clusters is even less plausible, as it would have to involve double dissociation of the $(\text{O}_2\text{CCO}_2)^-$ core to $\text{O}^- + \text{CO} + \text{CO}_2$, followed by an $\text{O}^- + \text{CO}_2 \rightarrow \text{CO}_3^-$ association. CO_3^- based products were previously seen in the photofragmentation of $(\text{CO}_2)_n^-$ cluster anions, in the $6 \leq n \leq 13$ size range only [74, 129,

84]. Later it was established that it is in this size-range that the $(\text{CO}_2)_n^-$ cluster anions have CO_2^- cores (with the dimer and monomer core coexistence at $n = 6, 13$ [79, 80, 83]). This parallel between the homogeneous and hydrated cluster results is another confirmation that the CO_3^- based fragments (in both cases) do indeed originate from parent clusters with CO_2^- cores.

Therefore, of all photofragments observed in this work, only the type (i) $\text{CO}_2^-(\text{H}_2\text{O})_k$ photofragments can potentially arise from the type-II $(\text{O}_2\text{CCO}_2)^-(\text{H}_2\text{O})_m$ parents. On the other hand, all three photofragment types are consistent with the type-I $\text{CO}_2^-(\text{H}_2\text{O})_m\text{CO}_2$ clusters. Most notably, none of the photofragments for $m = 3$ and 4 (see Table 5.1) can be attributed to the type-II parents and hence the fragmentation of these clusters must be attributed to a type-I CO_2^- core.

In summary, the photofragmentation results overall point towards the type-I cluster anion structures described as $\text{CO}_2^-(\text{H}_2\text{O})_m\text{CO}_2$, $m \geq 3$. This formula reflects the localization of the excess electron on a single CO_2 group, while the second, neutral CO_2 acts as a solvent. From the point of view of the energetics, the water molecules are expected to have priority in occupying the favorable binding sites in the first solvation shell around the core anion, which is reflected by placing the neutral CO_2 after the H_2O 's. The preferential stabilization of the CO_2^- core by solvation of polar molecules was observed previously by Tsukuda et al. [81].

Photoelectron imaging, on the other hand, suggests the coexistence of type-I and type-II clusters for $m = 3$ and 4. However, only the type-I clusters appear active in the photofragmentation, as no CO_2^- based fragments expected from the type-II clusters are seen. For $m > 3$, the coexistence of the $\text{CO}_2^-(\text{H}_2\text{O})_m\text{CO}_2$ and $(\text{O}_2\text{CCO}_2)^-(\text{H}_2\text{O})_m$

structures still remains possible and both may contribute to channel (i), yielding $\text{CO}_2^-(\text{H}_2\text{O})_k$ products. However, just the CO_2^- based parent clusters are both required and sufficient to explain all the observed fragmentation pathways.

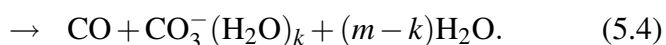
5.4.2 Solvent-Evaporation and Core-Dissociation Pathways in $[(\text{CO}_2)_2(\text{H}_2\text{O})_m]^-$, $m = 3-11$

As discussed in Section 5.4.1, the type (i) fragments, $\text{CO}_2^-(\text{H}_2\text{O})_k$, can be formed from either the type-I $\text{CO}_2^-(\text{H}_2\text{O})_m\text{CO}_2$ or type-II $(\text{O}_2\text{CCO}_2)^-(\text{H}_2\text{O})_m$ parent clusters. In the former case, these fragments should be described as solvent-evaporation products. In the latter, they result from the dissociation of the dimer-anion core.

The type (ii) $\text{O}^-(\text{H}_2\text{O})_k$ fragment ions originate from type-I clusters described as $\text{CO}_2^-(\text{H}_2\text{O})_m\text{CO}_2$. The dissociation of the CO_2^- core has been proposed [118] to proceed via a solvent-enabled, Renner-Teller mediated mechanism and is followed by the ejection of CO from the cluster and evaporation of the solvent CO_2 molecule. The process may also involve the loss of one or in rare cases two H_2O molecules (see Figure 5.4). For example, $\text{CO}_2^-(\text{H}_2\text{O})_3\text{CO}_2$ yields only one type (ii) fragment, $\text{O}^-(\text{H}_2\text{O})_3$, which corresponds to the loss of zero water molecules. On the other hand, the most intense $\text{O}^-(\text{H}_2\text{O})_k$ fragments arising from $m = 4-11$ reflect the loss of one H_2O .

5.4.3 Photoinduced Ion-Molecule Reaction in $\text{CO}_2^-(\text{H}_2\text{O})_m\text{CO}_2$, $m = 3-6$ Cluster Anions

The appearance of the type (iii) $\text{CO}_3^-(\text{H}_2\text{O})_k$, $k = 0-3$ fragments for $m = 3-6$ can be interpreted in terms of the following scheme:



Here, the fragmentation process is initiated by the dissociation of the CO_2^- cluster core [Equation 5.2] via the Renner-Teller mediated mechanism discussed previously [118] and described Section 5.4.2. Considering the relatively small parent cluster size ($m = 3-6$), the CO fragment is likely to be ejected from the cluster before the loss of any solvent molecules can occur. The O^- fragment, on the other hand, is bound to the remainder of the cluster by stronger ion-neutral interactions and may trigger a fast, barrierless, ion-molecule association reaction with the solvent CO_2 [Equation 5.3]. The water molecules act as an energy-absorbing bath, stabilizing the CO_3^- product at the expense of evaporation of several H_2O 's [Equation 5.4].

The dissociation energy of CO_3^- to $\text{O}^- + \text{CO}_2$ in the absence of a solvent was recently determined to be 2.79 eV (64.34 kcal/mol) [130]. This provides the upper bond for the bulk of the total energy that is dissipated by water evaporation in Equation 5.4. In addition, the kinetic energy of nascent O^- arising from the dissociation of CO_2 should be considered, but is expected to be comparatively small. This is specially true since a significant fraction of the CO_2^- dissociation excess energy is deposited into the

CO counterfragment, as indicated by the studies of dissociative electron attachment to CO₂ [119, 121]. Yet another factor affecting the reaction energetics is the effect of hydration, particularly the difference in the hydration energies of the parent, intermediate, and product ions: CO₂⁻, O⁻, and CO₃⁻, respectively. Viggiano et al. [131] reported $\Delta H \leq -25$ kcal/mol for the reaction of monohydrated O⁻ with CO₂. Without providing a lower bound for the ΔH , this estimate differs significantly from the isolated-reaction exothermicity quoted above. Later, Bowers and co-workers [132] assigned a value of 1.58 eV (36.4 kcal/mol) to the energy difference between the O⁻(H₂O) + CO₂ products and the CO₃⁻(H₂O) parent ion. In the absence of thermodynamic data for the reaction of O⁻(H₂O)_{*m*} with CO₂, Yang and Castleman [133] made use of the expected similarities with reactions of OH⁻(H₂O)_{*n*} with CO₂ to predict that the enthalpy change approaches nearly a constant value as the cluster size increases.

These uncertainties make evaluating the intracluster O⁻ + CO₂ → CO₃⁻ reaction energetics rather difficult. From the above ΔH values [131, 132, 133, 134], we estimate that the energy dissipated by water evaporation in Equation 5.4 should be in the range of 30–40 kcal/mol (1.3–1.7 eV). Keese et al. [135] reported enthalpies corresponding to the CO₃⁻(H₂O)_{*m*} → CO₃⁻(H₂O)_{*m*-1} + H₂O reactions to range from 14.1 kcal/mol (0.61 eV) for *m* = 1 to 13.1 kcal/mol (0.57 eV) for *m* = 3. Hence, in the *m* = 3–6 range, where the CO₃⁻(H₂O)_{*k*} fragments are seen, the assumed reaction exothermicity is expected to be sufficient for evaporating three water molecules. This estimate agrees with the experimental results, as most CO₃⁻(H₂O)_{*k*} fragments correspond to the loss of three H₂O's. Should these products be interpreted as electrostatically bound O⁻ · CO₂ or O⁻(H₂O)_{*k*}CO₂ complexes, the energy required for the observed water loss would

be lacking. Hence, the observed evaporation is a signature of the formation of a new chemical bond in the CO_3^- based products.

The critical step of the above mechanism, the association of O^- with CO_2 in the presence of water molecules, has been studied separately [131, 133]. Viggiano et al. [131] examined the reactions of $\text{O}^-(\text{H}_2\text{O})_{1,2}$ with CO_2 and observed CO_3^- as the only ionic product. Yang and Castleman [133] studied the reactions of larger hydrated clusters of O^- with CO_2 and proposed a mechanism, according to which the $\text{O}^-(\text{H}_2\text{O})_m$ clusters react with CO_2 via ligand substitution. In this process, the thermodynamically favored association yields a new cluster core, while the immediate evaporation of a ligand (solvent) removes some of the reaction exothermicity.

Finally, the possibility of intracluster reaction of the nascent O^- fragments with H_2O giving $\text{OH}^- + \text{OH}$ needs to be addressed. Johnson and co-workers [124] characterized this reaction following the photodissociation of O_2^- within the $\text{O}_2^- \cdot \text{H}_2\text{O}$ complex. In the present work, we observe no sign of this reaction, which is not surprising considering that the process is endothermic by 0.36 eV [136]. Without accounting for the hydration effects, only an estimated 0.1 eV is released in 355 nm dissociation of CO_2^- . This value is obtained as the difference between $h\nu$ and the bond dissociation energy (3.39 eV), calculated as:

$$D_0(\text{CO} - \text{O}^-) = D_0(\text{CO} - \text{O}) - \text{AEA}(\text{O}) + \text{AEA}(\text{CO}_2) \quad (5.5)$$

where $D_0(\text{CO} - \text{O}^-) = 5.453$ eV is the corresponding value for $\text{CO}_2 \rightarrow \text{CO} + \text{O}(^3P)$ [110, 111], and $\text{AEA}(\text{O})=1.461$ eV and $\text{AEA}(\text{CO}_2)=-0.6$ eV are the adiabatic electron affinities of $\text{O}(^3P)$ [112] and CO_2 [54], respectively. For comparison, in the Johnson $\text{O}_2^- \cdot \text{H}_2\text{O}$ experiment the nascent O^- fragments carried recoil energies of up to 0.75 eV

[124]. Another candidate for possible reactivity with the water solvent molecules is the bicarbonate HCO_3^- anion, which was not observed. One may wonder whether the $\text{O}^-(\text{H}_2\text{O})_m$ clusters could be described as $\text{OH}^-(\text{OH})(\text{H}_2\text{O})_{m-1}$ [137, 138], and therefore the OH^- could react with CO_2 to form HCO_3^- . The fact that no HCO_3^- based fragments were observed may be an indication that the reaction of nascent O^- with CO_2 happens faster than the nuclear rearrangements in the cluster geometry (the possibility of not being able to resolve one mass unit difference with CO_3^- in our reflectron, although not very likely, cannot be completely discarded).

5.4.4 Channel Competition

Both the $\text{O}^-(\text{H}_2\text{O})_k$ and $\text{CO}_3^-(\text{H}_2\text{O})_k$ fragment channels are triggered by the photodissociation of the CO_2^- core of the parent $\text{CO}_2^-(\text{H}_2\text{O})_m\text{CO}_2$ cluster. It is therefore intriguing that the relative yield of the ion-molecule reaction products, $\text{CO}_3^-(\text{H}_2\text{O})_k$, decreases steadily with m in the $m = 3-6$ range and no fragments of this type are observed at all for $m > 6$. As evident in Figure 5.4, in the $m = 7-11$ clusters the second, neutral CO_2 molecule is always lost in the fragmentation process.

To quantify this observation, we define the probability for a core-dissociation event [Equation 5.2] to lead to a successful ion-molecule association reaction of nascent O^- with the solvent CO_2 [Equations 5.3 and 5.4] as follows:

$$\phi_{IM}(m) = \frac{I(\text{CO}_3^-)}{I(\text{O}^- + I(\text{CO}_3^-))}. \quad (5.6)$$

Here, $I(\text{CO}_3^-)$ and $I(\text{O}^-)$ represent the integrated intensities of all $\text{O}^-(\text{H}_2\text{O})_k$ and $\text{CO}_3^-(\text{H}_2\text{O})_k$ fragments, respectively, observed for a given m . Hence, the denominator accounts for all channels involving the dissociation of the CO_2^- cluster core, while the

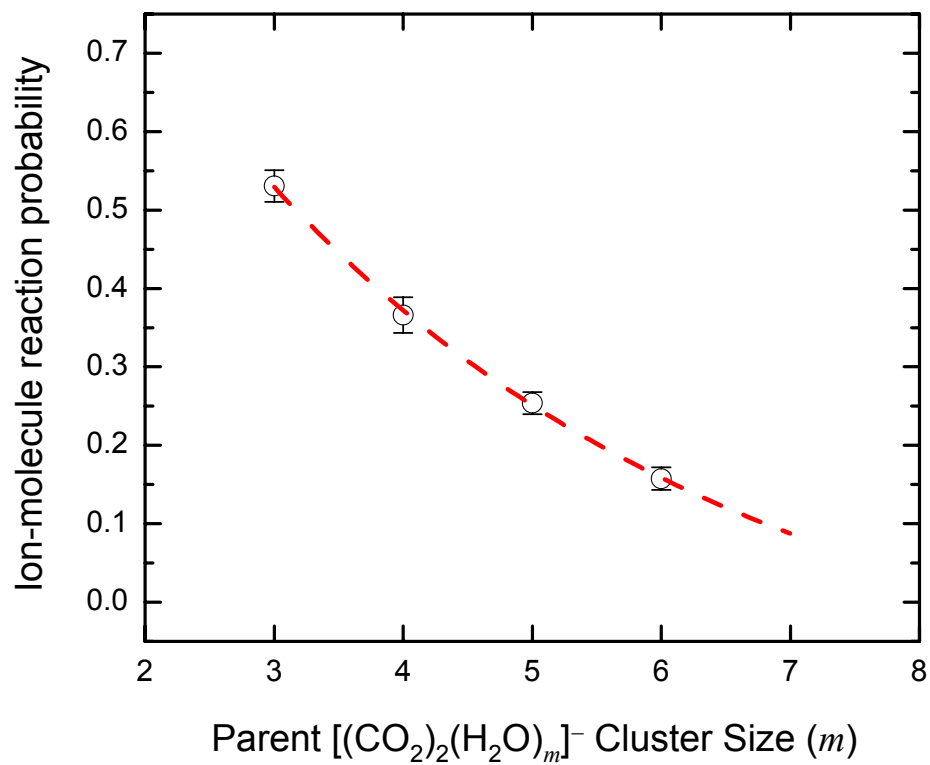


Figure 5.5: Probability for the nascent O^- fragment to undergo an intracuster ion-molecule association reaction with CO_2 .

numerator represents the secondary ion-molecule reaction events. The fraction $\phi_{IM}(m)$ is plotted in Figure 5.5, indicating that the probability of the nascent O^- reaction with CO_2 decreases rapidly with increasing hydration. Previously, Viggiano et al. [131], independently followed by Yang and Castleman [133], also found a reduction in reactivity with increasing hydration.

This decrease in the secondary ion-molecule reaction probability may be indicative of the neutral CO_2 being physically separated from the CO_2^- cluster core (and therefore the nascent O^-) by the water molecules—solvent obstructed reaction. This hypothesis is consistent with the expectation that the water molecules will tend to have priority (over CO_2) in occupying the binding sites in the immediate proximity of the ionic core. Another possibility for the observed diminishing reactivity may involve the formation of carbonic acid in the solvent shell by the reaction of the neutral CO_2 with an H_2O solvent molecule, the new solvent H_2CO_3 molecule is not expected to efficiently react with O^- .

5.5 Summary

The fragmentation of mass-selected $[(CO_2)_n(H_2O)_m]^-$, $m = 3-11$ cluster anions points towards predominantly CO_2^- based parent structures, described as $CO_2^-(H_2O)_mCO_2$. Photoelectron spectroscopy, however, suggests the coexistence of the $CO_2^-(H_2O)_mCO_2$ and $(O_2CCO_2)^-(H_2O)_m$ structures for $m = 3-4$ and some presence of the $(O_2CCO_2)^-$ based clusters cannot be ruled out for larger clusters ($m > 4$) as well. Nonetheless, just the CO_2^- based structures are required and sufficient to explain all the observed photofragmentation pathways.

Three types of anionic photofragments are observed at 355 nm: $CO_2^-(H_2O)_k$;

$\text{O}^-(\text{H}_2\text{O})_k$, and $\text{CO}_3^-(\text{H}_2\text{O})_k$, $k \leq m$. The $\text{O}^-(\text{H}_2\text{O})_k$ and $\text{CO}_3^-(\text{H}_2\text{O})_k$ channels are believed to be triggered by the dissociation of the CO_2^- cluster core. In the $\text{CO}_3^-(\text{H}_2\text{O})_k$ channel, the dissociation is followed by an intracluster ion-molecule reaction of nascent O^- with the solvent CO_2 , yielding a CO_3^- anion, which is stabilized by interactions with the water molecules. This channel is seen only in the parent cluster size range of $m = 3-6$, where its relative yield decreases rapidly with increasing m . This behavior is attributed to a decrease in the probability of the secondary ion-molecule reaction of nascent O^- with CO_2 due to hindrance from H_2O . Some ambiguity remains regarding the mechanism for the $\text{CO}_2^-(\text{H}_2\text{O})_k$ channel. The possibilities include the dissociation of the CO_2^- cluster core followed by its recombination, as well as the dissociation of the $(\text{O}_2\text{CCO}_2)^-$ core to $\text{CO}_2^- + \text{CO}_2$.

CHAPTER 6

SOLVENT RESONANCE EFFECT ON THE ANISOTROPY OF $\text{NO}^-(\text{N}_2\text{O})_n$
CLUSTER ANION PHOTODETACHMENT

6.1 Introduction

Studies of negatively charged clusters provide molecular-level views of chemical interactions relevant to anions in condensed environments [4, 5]. Recent advances in photoelectron imaging [6, 24, 9] have renewed interest in solvation effects on cluster anion photodetachment, emphasizing the photoelectron angular distributions (PADs) measured simultaneously with the photoelectron spectra. Disappointingly, however, it is becoming a rather prevailing view that despite some notable exceptions [87] the PADs merely tend to become more isotropic with increasing cluster size. This leads to a perception that the information content of photoelectron images is limited for larger clusters.

To counter this perception, consider the loss of photodetachment anisotropy when the departing electron's kinetic energy (eKE) falls within the range of anionic resonances associated with the solvent network. As a general explanation, a resonance temporarily captures the photodetached electron before it is released into the continuum, scrambling its phase and angular momentum. Considering the complex electronic structures and aggregate properties of many solvents, it is not surprising that the solvent-induced, scattering-mediated loss of photoelectron anisotropy is a frequent occurrence in cluster

chemistry. The diminished anisotropy, therefore, illuminates the role of photoelectron scattering on the solvent, complementing the information commonly derived from electron attachment and scattering spectra [139].

For example, the photodetachment of the $\text{I}^- \cdot \text{CH}_3\text{I}$ cluster anion at 267 nm yields a PAD with a markedly low anisotropy magnitude, compared to other mono-solvated iodide species, such as $\text{I}^- \cdot \text{Ar}$, $\text{I}^- \cdot \text{H}_2\text{O}$, and $\text{I}^- \cdot \text{CH}_3\text{CN}$ [140]. The anisotropy loss has been attributed, among other possibilities, to scattering of the departing electron by the CH_3I solvent molecule. This mechanism has been argued on the basis of the high scattering cross-section associated with a CH_3I^- shape resonance found close to the detached electron energy. More recently, Nakanishi et al. [141] observed a similar effect in the detachment of acetone (Acn) cluster anions, $(\text{Acn})_n^-$, where the PADs are found to be nearly isotropic for $n \geq 5$. Analogous to the $\text{I}^- \cdot \text{CH}_3\text{I}$ case, the acetone molecules possess an anionic resonance in the photoelectron energy range.

In this Chapter, we discuss the solvent-induced photoelectron anisotropy effects in the photodetachment of the $\text{NO}^-(\text{N}_2\text{O})_n$ cluster anions, with n ranging from 0 up to 7, depending on the laser wavelength. The photodetachment of some of these clusters has been studied previously without angular resolution, using traditional photoelectron spectroscopy [142, 143] and photofragment-photoelectron coincidence techniques [144]. Unsolvated NO^- is adiabatically stable with respect to autodetachment only in its ground vibrational state [145, 146]. Although it is an important anion in itself, the main focus of the present work is on the solvent role in electron photoemission from the NO^- cluster core. As the photoelectrons with specific eKE profiles propagate across the N_2O solvent shell, both elastic and inelastic scattering could, in general, lead to the reduction in the

PAD anisotropy. It is expected that large-angle scattering, contributing the most to the momentum-transfer cross-section [17], should have the greatest effect on the measured PADs.

Previous electron-scattering studies of N_2O are extensive (see, for example, Refs. [147] and [148] and references therein) providing evidence for two shape resonances in the low-eKE range: a Π symmetry resonance around 2.4 eV and a Σ resonance around 8 eV [149]. Vibrational Feshbach resonances near zero-eKE have also been observed [150, 151]. In the present work, the photoelectron imaging results for $\text{NO}^-(\text{N}_2\text{O})_n$ are reported alongside the corresponding $\text{NO}^-(\text{H}_2\text{O})_n$ data, highlighting the differences between the N_2O and H_2O solvents in their effects on the photodetachment anisotropies of the respective cluster anions. Highlights of this work have been published in [152].

6.2 Experimental

The experiments are performed on a negative-ion spectrometer described in Chapter 2. The cluster anions of interest are prepared starting with a pulsed supersonic expansion of a 20–50% $\text{N}_2\text{O}/\text{Ar}$ mixture into vacuum, with water contamination within the gas delivery lines as the source of H_2O . Anions are formed by secondary electron attachment to neutrals after ionizing the supersonic expansion with a 1 keV electron gun. The core NO^- anions are formed via the $\text{N}_2\text{O} + e^- \rightarrow \text{O}^- + \text{N}_2$, $\text{O}^- + \text{N}_2\text{O} \rightarrow \text{NO}^- + \text{NO}$ reaction sequence [153, 154]. The resultant anions are pulse-extracted into a mass-spectrometer flight tube, at the end of which the ions of selected mass are intercepted with a linearly polarized laser pulse. Pulses of 786 nm (100 fs, < 1 mJ) and 400 nm are derived from a Ti:Sapphire laser system (Spectra Physics, Inc.). The harmonics of a nanosecond

Nd:YAG laser (Spectra Physics, Inc., Quanta-Ray Lab 130-50) provide 532, 355, and 266 nm pulses (approximately 30, 20, and 10 mJ/pulse, respectively). The photoelectrons are projected on our imaging detector in the direction perpendicular to the ion and laser beams. To discriminate against background, the detector is pulsed on for a 200 ns window coinciding with the arrival of the photoelectrons. The photoelectron images are recorded by a computer-controlled CCD camera for $(1 - 5) \times 10^4$ experimental cycles. The known vibrational lines of the bare NO^- photoelectron spectrum [155, 156] are used for energy calibration. The photoelectron angular distributions (PADs) are analyzed using the Basis Set EXpansion (BASEX) program obtained from Dribinski et al. [26].

6.3 Results and Data analysis

6.3.1 Photoelectron images and energy spectra

Figure 6.1 shows the raw and Abel-inverted photoelectron images of unsolvated NO^- , collected at 786, 532, and 355 nm, along with the corresponding eKE spectra. The perceptible rings in the images correspond to the well-characterized [142, 153, 156, 155] progression of transitions to the $X^2\Pi, v' = 0 - 5$ vibrational states of NO from the ground $X^3\Sigma^-, v'' = 0$ state of NO^- . The rings appear congested at 355 nm, but the vibrational structure remains resolved, as emphasized in the magnified part of the image in Figure 6.1(c). The outermost rings in all images correspond to the $0 \leftarrow 0$ transition, peaking at an electron binding energy (eBE = $h\nu - \text{eKE}$) of 0.04 ± 0.01 eV. Subject to rotational and spin-orbit corrections, this determination is consistent with the literature value of 0.026 ± 0.005 eV for the adiabatic electron affinity of NO [155].

Figure 6.3 shows the 355 nm photoelectron images and the corresponding spectra for

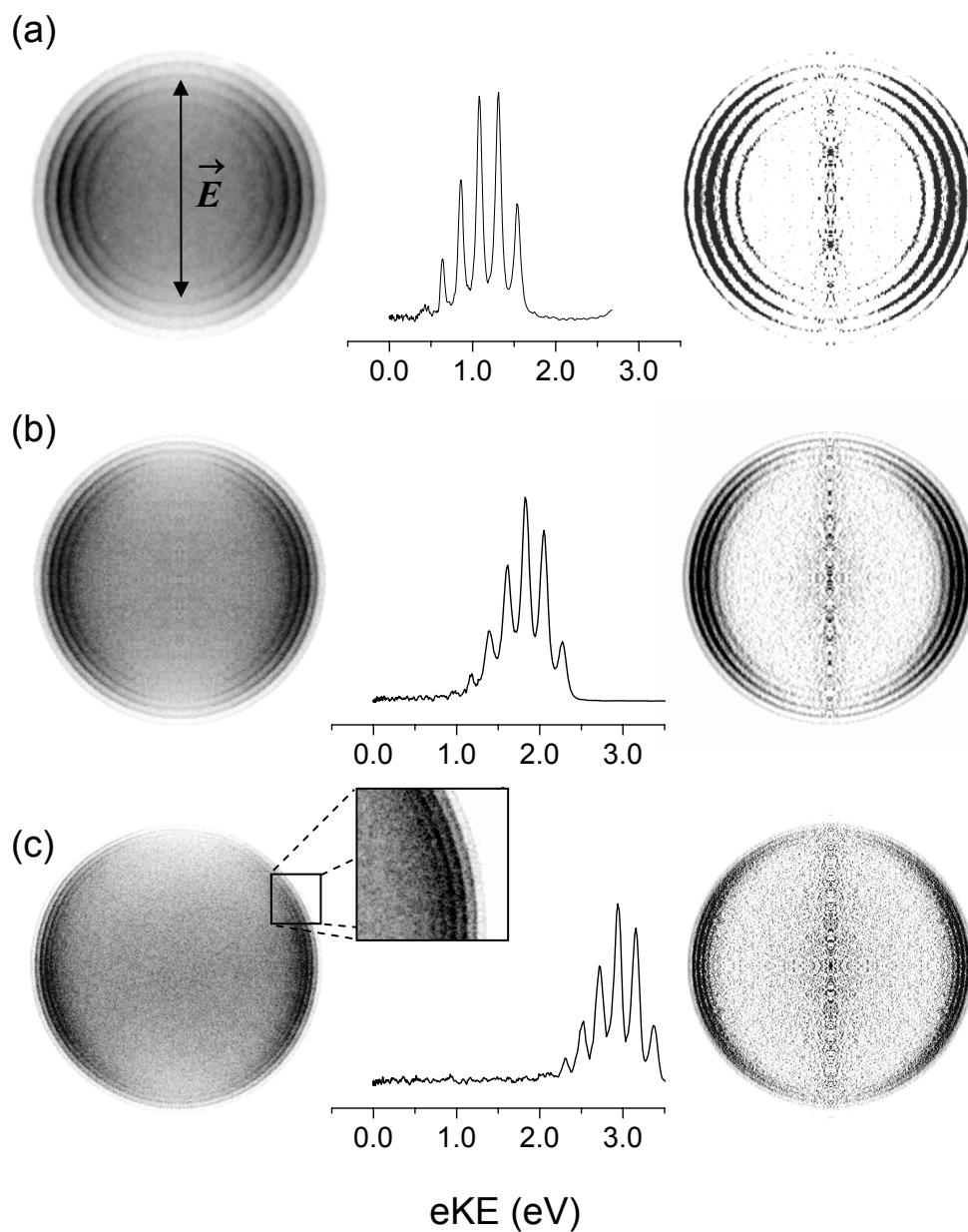


Figure 6.1: Raw (left column) and Abel-inverted (right column) NO^- photoelectron images and the corresponding photoelectron energy spectra obtained at (a) 786 nm, (b) 532 nm, (c) 355 nm. The images were taken under different electrostatic focusing imaging conditions and are shown not to scale. Double arrow in (a) indicates the direction of the laser polarization for all images. Inset in (c) shows a magnified portion of the corresponding image.

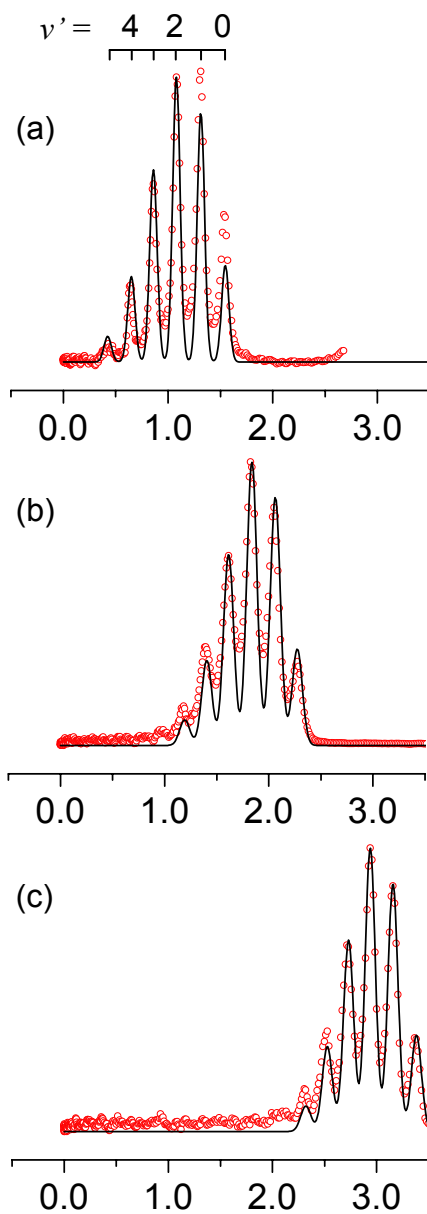


Figure 6.2: Experimental NO^- photoelectron spectra (open circles) and simulated spectra (solid lines) for (a) 786 nm, (b) 532 nm, (c) 355 nm photodetachment. The Franck-Condon factors obtained by Arrington et al. [157] were convoluted with individual Gaussians of equal widths corresponding to each vibrational transition.

the $\text{NO}^-(\text{N}_2\text{O})_n$, $n = 0-5$ cluster anions. In addition to the data shown, the photoelectron images obtained at 355 nm for n up to 7, at 532 nm for $n = 0-5$, and at 786 nm for $n = 0-3$ are included in the foregoing analysis. With the exception of the low-eKE spectral regions (discussed below), the energetic characteristics of the $\text{NO}^-(\text{N}_2\text{O})_n$ photoelectron spectra in Figure 6.3 are consistent with the electrostatically bound ion-neutral complexes studied previously by the Bowen group [142, 143], where the excess electron is localized on the nitric oxide component of the cluster. The addition of each solvent N_2O molecule causes a spectral shift of about 0.2 eV to lower eKEs, accompanied by progressive broadening of the image rings and spectral peaks.

The $\text{NO}^-(\text{N}_2\text{O})_n$, $n = 1$ image includes a central feature corresponding to slow photoelectrons. This feature is absent for unsolvated NO^- (Figure 6.1 and Figure 6.3, $n = 0$), and nearly unobservable for $\text{NO}^-(\text{N}_2\text{O})_n$, $n > 1$ (Figure 6.3). It is attributed to the covalent, w-shaped N_3O_2^- singlet anion, as proposed by Hiraoka et al. [158] and characterized by Resat et al. [144] and Torchia et al. [159]. Further confirmation of the presence of the N_3O_2^- isomer in our experiment comes from a small N_2O^- photofragment signal shown in Figure 6.5, which we observed with our secondary reflectron mass-spectrometer in 532 nm (2.33 eV) dissociation of the $\text{NO}^-(\text{N}_2\text{O})_n$, $n = 1$ cluster. As suggested by Snis and Panas [160], this photofragment arises from a dissociative excitation of the covalent N_3O_2^- anion bound by 1–2 eV with respect to $\text{N}_2\text{O}^- + \text{NO}$. The finding of this anionic photofragment may help to elucidate the N_3O_2^- “paradigm” (see Ref. [161] for a survey of the N_3O_2^- anion complexity). We excluded the low-eKE spectral regions from the anisotropy analysis, which was thus limited to the bands arising from the NO^- cluster core only.

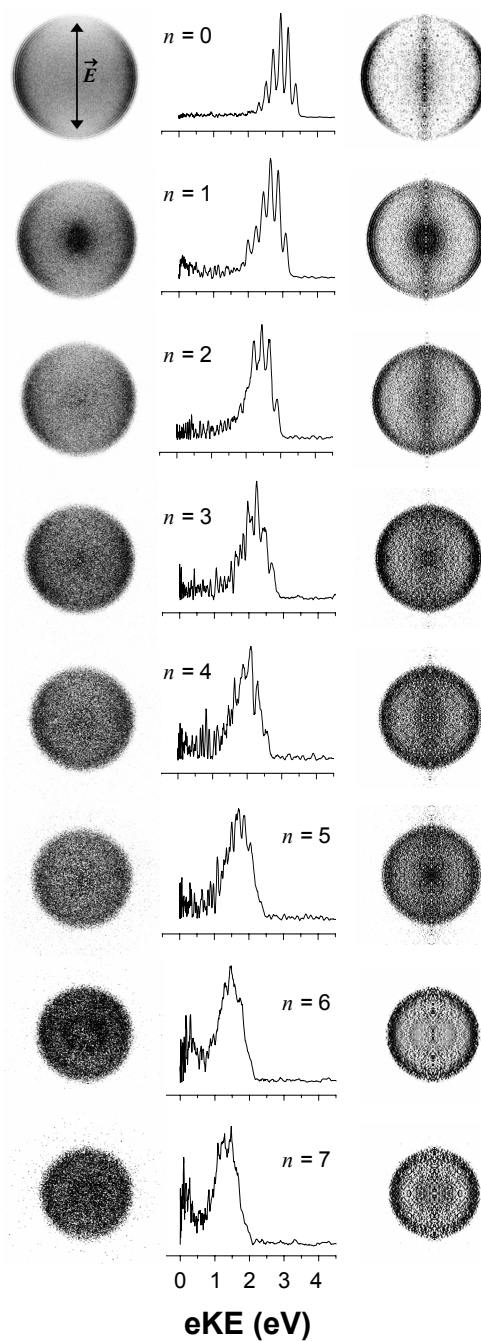


Figure 6.3: Raw (left column) and Abel-inverted (right column) photoelectron images and corresponding photoelectron images and their corresponding spectra obtained at 355 nm for $\text{NO}^-(\text{N}_2\text{O})_n$, $n=0-7$. All images are acquired under similar experimental conditions and are shown not to scale. Double arrow in the $n=0$ image indicates the direction of the laser polarization for all images. The $n=0$ image indicates the direction of the laser polarization for all images. The $n=0$ image is the same as in Figure 6.1.

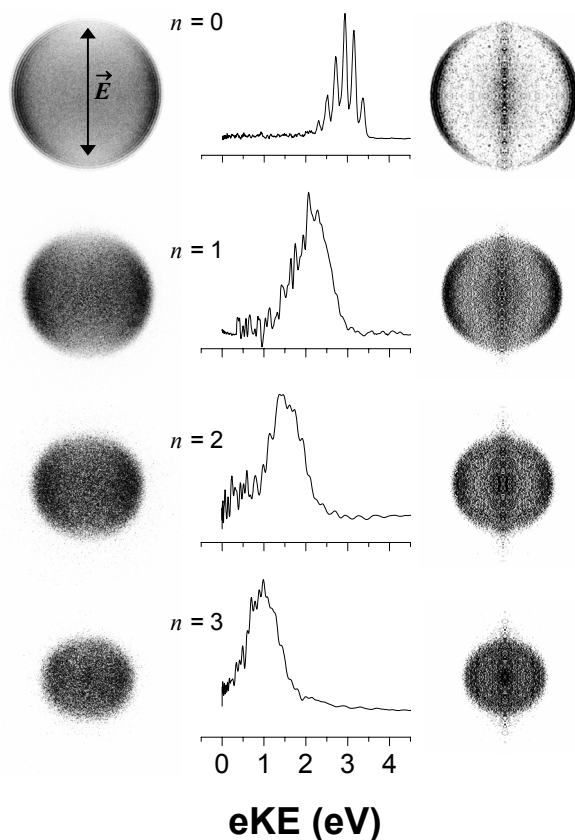


Figure 6.4: Raw (left column) and Abel-inverted (right column) photoelectron images and corresponding photoelectron images and their corresponding spectra obtained at 355 nm for $\text{NO}^-(\text{H}_2\text{O})_n$, $n = 0-3$. All images are acquired under similar experimental conditions and are shown not to scale. Double arrow in the $n = 0$ image indicates the direction of the laser polarization for all images. The $n = 0$ image indicates the direction of the laser polarization for all images. The $n = 0$ image is the same as in Figure 6.1.

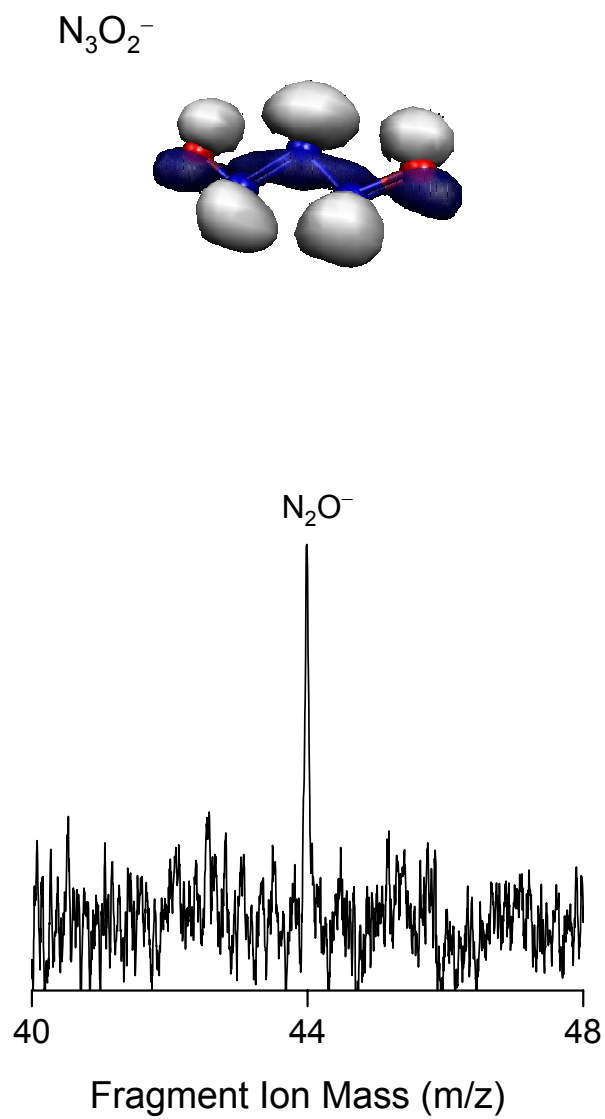


Figure 6.5: N_2O^- photofragment resulting from the 532 nm dissociation of N_3O_2^- .

Figure 6.4 shows 355 nm photoelectron images and the corresponding spectra of $\text{NO}^-(\text{H}_2\text{O})_n$, $n = 0-3$. The spectra are in agreement with the previous measurements by Eaton et al. [162]. The loss of vibrational structure in the $\text{NO}^-(\text{H}_2\text{O})_n$ spectrum is related to the strength of the ion-solvent interaction, where anionic geometries caused by stronger ionic H bonds lead to higher vibrational excitations in the resulting neutral complex. In addition, Myshakin et al. [163] found two isomeric species for $\text{NO}^-(\text{H}_2\text{O})_1$, with the H bonds forming with either the N or O atom of the NO^- core, contributing to additional line broadening.

6.3.2 Photoelectron angular distributions for unsolvated NO^-

The PADs resulting from one-photon detachment with linearly polarized light are generally described as:

$$I(\theta) \propto 1 + P_2(\cos \theta), \quad (6.1)$$

where β is the anisotropy parameter, θ is the angle between the photoelectron velocity and the laser polarization vectors, and P_2 is the second-order Legendre polynomial [12, 13]. Inspection of Figure 6.1 reveals a perpendicular ($\beta < 0$) nature of the NO^- PADs. Negative values are generally expected in the detachment from antibonding π orbitals of diatomic anions, as discussed, for example, in regards to π_g^{-1} photodetachment of O_2^- [164] and S_2^- [15]. Although NO^- lacks inversion symmetry, its $2p\pi^*$ HOMO (shown in the inset in Figure 6.7) is qualitatively similar to O_2^- and the observed negative anisotropy is therefore not surprising.

The β values for the individual vibrationally resolved rings in the 786 nm, 532 nm, and 355 nm NO^- photoelectron images (Figure 6.1) are plotted versus the corresponding

eKE values in Figure 6.7 (grey open circles). The results for each wavelength appear to follow parabolic patterns, consistent between multiple experimental runs on two different instruments in our laboratory. The patterns are indicated by dashed parabolas in Figure 6.7, fitted to the corresponding data. One possible reason for the more isotropic angular distributions of the transitions involving the $v'' = 0$ and $v'' = 1$ of neutral NO (the ones with higher eKEs) resulting in these parabolic shapes, may involve the formation of a temporary vibrationally excited $\text{NO}^-(A^3\Pi)$ state that is followed by autodetachment via:



This $^3\Pi$ state (formally a resonance) has been calculated by Polak and Fiser [165] and its equilibrium geometry falls much closer to that of neutral NO compared to the initial ground state of the anion. Thus, if a transition occurs to the $^3\Pi$ potential curve, autodetachment is expected to leave the remaining neutral on its lowest two vibrational states as indicated in Figure 6.6. The slight deviation from the expected Franck-Condon intensities in the 786 nm spectrum for the $v' = 0, 1$ shown in Figure 6.2 may also be an indication of contributions to the spectra from this autodetachment process. A similar argument was proposed by Johnson and co-workers for the non-Franck-Condon behavior observed in the photodetachment of O_2^- [166].

Averaged β values (corresponding to the PADs integrated over the entire Franck-Condon envelope of the transition) are shown in Figure 6.7 as black filled circles. In addition, the averaged β value from a 266 nm NO^- photoelectron image is included at average eKE = 4.11 eV, as well as the vibrationally resolved 488 nm results of Siegel et al. [156], indicated by crosses. The β values in Figure 6.7 are compared to a solid curve obtained by a non-linear fit (Levenberg-Marquardt) to the data using the Cooper-Zare

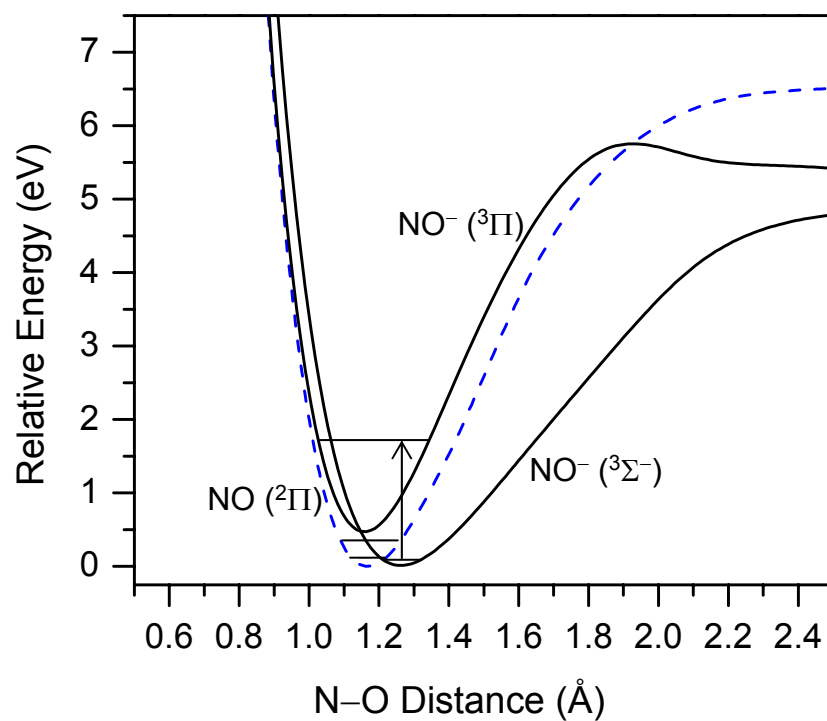


Figure 6.6: Qualitative potential energy curves for NO and NO^- based on the results of Polak and Fiser [165] and McCarthy et al. [146]. This figure shows the formation of a $^3\Pi$ resonance as a plausible mechanism for the loss of anisotropy for the $v' = 0, 1$ levels. The arrow represents a vertical transition initiated by a 786 nm photon. The hypothetically populated excited anionic state is expected to autodetach leaving neutral NO in the $v' = 1$ or $v' = 0$ levels.

central-potential model [12, 13]. We used the simplified version of the model proposed by [29], which assumes no interaction between the departing electron and the neutral residue. This is justified by the small dipole moment (0.16 D) of NO [102]. The simplified expression for the anisotropy parameter β as a function of the electron kinetic energy ($\varepsilon = eKE$) takes the form:

$$\beta = \frac{\ell(\ell - 1) + (\ell + 1)(\ell + 2)A^2\varepsilon^2 - 6\ell(\ell + 1)A\varepsilon \cos \phi}{(2\ell + 1)[\ell + (\ell + 1)A^2\varepsilon^2]}, \quad (6.3)$$

where ϕ is the relative phase of the $\ell' = \ell \pm 1$ partial waves and A is a coefficient related to the spatial extent of the negative ion [140]. The fitting procedure is similar to the studies of S_2^- and O_2^- [15, 164, 167], the $2p\pi^*$ HOMO of NO^- is approximated as a d -like orbital with an effective angular momentum quantum number $\ell = 2$. For consistent comparison with the cluster data, only the average β values, corresponding to the integrated PADs (filled circles in Figure 6.7), were used for the model fit. The resulting Cooper-Zare curve shown in Figure 6.7 corresponds to $\cos \phi = 0.881$ for the relative phase ϕ of the $\ell' = \ell \pm 1$ partial waves and $A = 0.383 \text{ eV}^{-1}$.

6.3.3 Solvation effects on photoelectron anisotropy

The $NO^-(N_2O)_n$ PADs extracted from the images in Figure 6.3 reveal a gradual loss of photodetachment anisotropy with increasing solvation. The trend is particularly notable in comparison with the PADs obtained for the $NO^-(H_2O)_n$ images in Figure 6.4. The latter retain a greater degree of anisotropy upon hydration, despite the much larger spectral shifts induced by sequential addition of H_2O , compared to N_2O . This becomes particularly clear by direct comparison of the anisotropy parameter values obtained for the individual cluster ions by integrating the PADs over the corresponding spectral profiles.

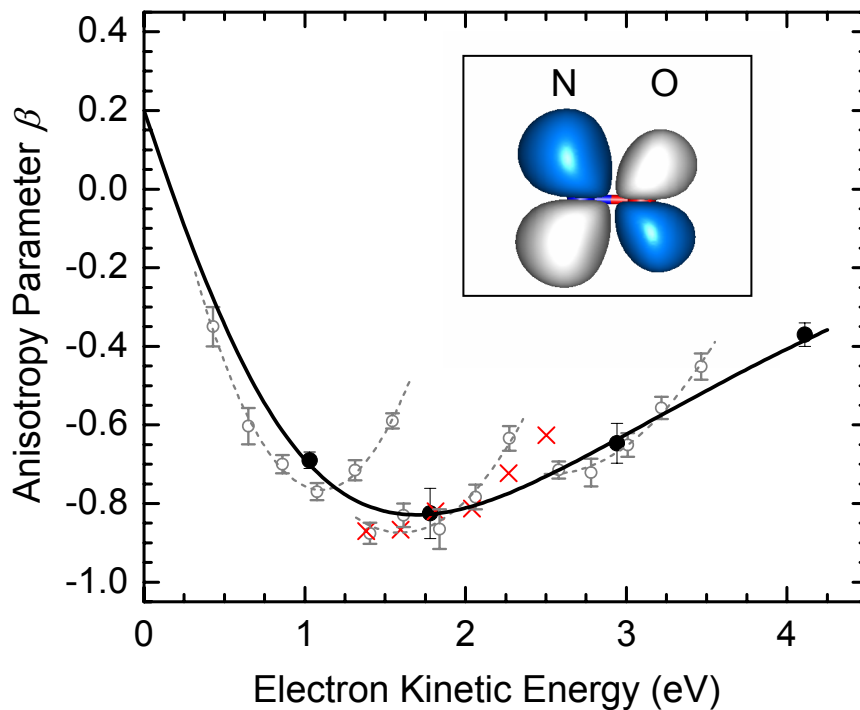


Figure 6.7: Grey open circles: the anisotropy parameter (β) values determined for vibrationaly resolved NO^- photodetachment transitions at 786, 532, and 355 nm, corresponding to the photoelectron images in Figure 6.1(a)–(c), respectively. Dashed grey curves are parabolic fits to the vibrationaly resolved data for each of the above wavelengths. Black filled circles: average β values obtained by integrating the 786, 532, 355, and 266 nm NO^- PAD over the entire Franck-Condon envelopes of the corresponding transitions, plotted as a function of the average eKE. Red crosses: vibrationaly resolved 488 nm β values obtained from Ref. [156]. Solid Curve: the Cooper-Zare model fit to the average β data points (filled circles) obtained as described in the text. Insert shows a calculated isosurface plot of the $2p\pi^*$ orbital of NO^- .

The resulting β values are plotted in Figure 6.8(a) versus average eKE, which is used both as a measure of solvation and as a natural variable for comparison with the Cooper-Zare model. Five separate data sets are shown. Sets 1, 2, 3, and 4, as labeled in Figure 6.8, correspond to the $\text{NO}^-(\text{N}_2\text{O})_n$ cluster anions studied at 355, 400, 532, and 786 nm, respectively. The cluster sizes, indicated in Figure 6.8(a) next to the data points, range from $n = 0$ [unsolvated NO^- , filled black circles in Figure 6.8(a)] to $n = 7, 4, 5,$ and 3 for Sets 1, 2, 3, and 4, respectively. Set 5 corresponds to $\text{NO}^-(\text{H}_2\text{O})_n$, $n = 0-3$ at 355 nm. The $\beta(\text{eKE})$ trends are compared to the Cooper-Zare curve for unsolvated NO^- , determined in Figure 6.7 and reproduced as a dashed curve in Figure 6.8(a). The greatest deviation from the model prediction is exhibited by Set 1, corresponding to $\text{NO}^-(\text{N}_2\text{O})_n$ at 355 nm.

To quantify the deviations in β and account for the varying number of solvent molecules n , we introduce a normalized solvent-induced anisotropy differential D , defined as:

$$D = \frac{\Delta\beta}{n^\alpha}, \quad (6.4)$$

where $\Delta\beta = \beta(\text{eKE}) - \beta_{\text{CZ}}(\text{eKE})$, with $\beta(\text{eKE})$ and $\beta_{\text{CZ}}(\text{eKE})$ being the $n > 0$ data from Figure 6.8(a) and the $n = 0$ Cooper-Zare predicted values, respectively, and α is an empirical exponent. Thus defined, D is not intended as a rigorous measure of solvation effects. It is proposed only for clarifying the observed trends and discriminating between the factors in play, namely the eKE dependence and solvent coordination. Subtracting $\beta_{\text{CZ}}(\text{eKE})$ in $\Delta\beta$ accounts for the expected Cooper-Zare model trend, as applied to the (unperturbed) core NO^- anion photodetachment, with the balance attributed to the solvent effects. These are expected to depend on the solvent nature and the number of solvent

molecules present. Since the scaling of $\Delta\beta$ with n is unlikely to be linear, an empirical n^α normalization is included in Equation 6.4, with α expected to be between 0 and 1.

The five sets of D values, corresponding to Sets 1–5 defined above ($n > 0$), are plotted in Figure 6.8(b) using $\alpha = 0.8$. This empirical value is chosen arbitrarily to match the D values for Sets 1–2, 1–3, and 3–4 within the overlapping eKE ranges; however, reasonable variations in α do not change the foregoing conclusions. The resulting $D(\text{eKE})$ variations for Sets 1–4, on the one hand, and Set 5, on the other, represent the energy-dependent effects on the PADs attributed to the solvation by N_2O and H_2O , respectively, normalized (empirically) to the numbers of solvent molecules in the corresponding clusters.

6.4 Discussion

Viewing cluster photodetachment as electron ejection from the core anion, followed by its scattering on the solvent, the PADs can be affected by the solvent via the following mechanisms. First is the change in the partial-waves balance due to the solvation-induced decrease in eKE. Second is the solvent-induced perturbation of the initial electronic state, including any distortions of the core-anion geometry and/or symmetry, as well as possible delocalization of the excess electron to the solvent. Third is the departing electron scattering on the solvent molecules.

In our analysis, the first of the above effects is accounted for by comparing the observed anisotropy values to the Cooper-Zare model predictions. Regarding the second, only minimal distortion of the core anion structure and/or charge delocalization to the solvent network are indicated in Figures 6.3 and 6.4, where the cluster anion spectra clearly retain the NO^- character. In addition, *ab initio* calculations on $\text{NO}^- \cdot \text{N}_2\text{O}$

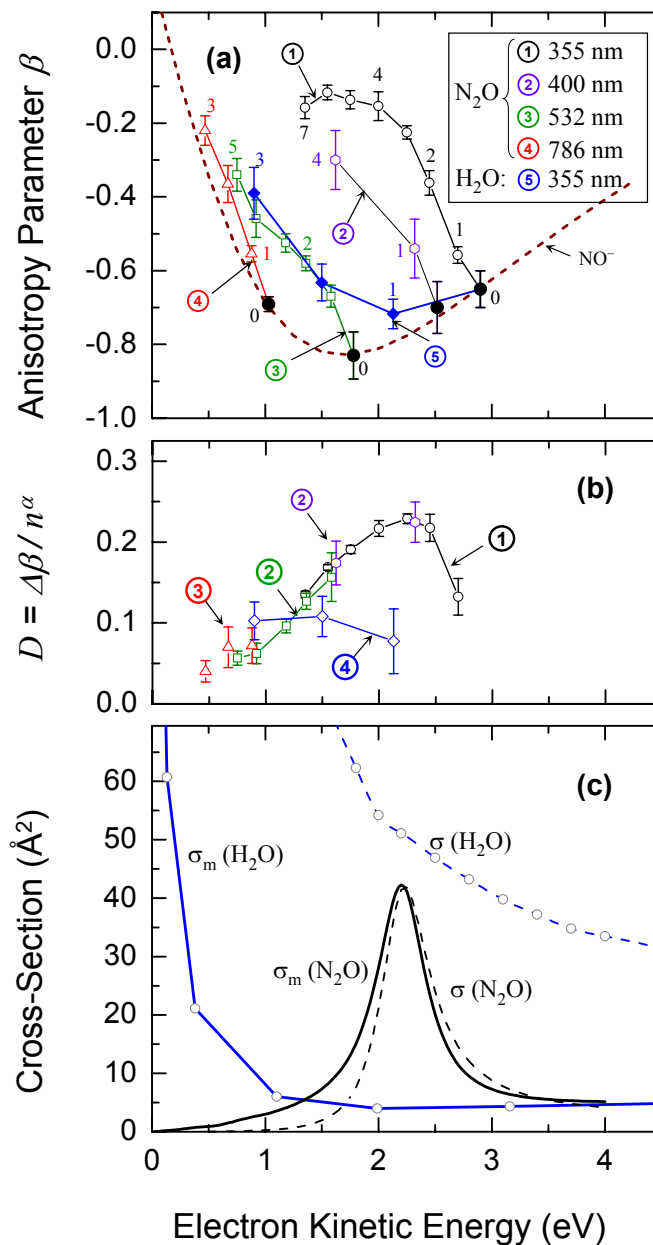


Figure 6.8: (a) Data series 1–5, as indicated in the legend: Photoelectron anisotropy parameters for $\text{NO}^- (\text{N}_2\text{O})_n$ and $\text{NO}^- (\text{H}_2\text{O})_n$ as a function of average eKE. The numbers of solvent molecules (n) are displayed next to data points. The NO^- ($n = 0$) data, shown as filled circles, as well as the Cooper-Zare curve for bare NO^- , shown as dashed lines, are reproduced from Figure 6.7; (b) Normalized anisotropy differential D (defined in the text) for data sets 1–5 from (a); (c) The absolute total cross sections (dashed) and momentum transfer cross section (solid) for electron collisions N_2O (black) and H_2O (blue). The H_2O and N_2O cross section data are from Refs. [168] and [147], respectively

predicted only a 2% charge delocalization to the solvent molecule [169]. This brings our focus to electron scattering on the solvent.

Shown as dashed curves in Figure 6.8(c) are the total electron scattering cross-sections, $\sigma(\text{eKE})$, for N_2O and H_2O , based on the data from Refs. [147] and [170], respectively. The $\text{N}_2\text{O} + e^-$ cross-section reveals a resonance with a maximum at 2.25 eV. In contrast, the $\text{H}_2\text{O} + e^-$ curve reflects a steep decline with increasing eKE in the low-eKE region, with no evidence of resonances in the region of interest. Nonetheless, the total cross-section for H_2O exceeds that for N_2O in the entire range shown. This seemingly contradicts our principal conclusion ascribing the anisotropy decay in cluster-anion photodetachment primarily to electron-solvent scattering.

To reconcile these observations, we consider the qualitatively different electron scattering mechanisms for H_2O and N_2O . The $\text{H}_2\text{O} + e^-$ scattering in the 0–4 eV range is dominated by long-range interaction of the electrons with the molecular dipole moment. Classically speaking, most scattering events occur with large impact parameters and lead to small-angle scattering of the incident electrons. This expectation is confirmed by the dependence of the $\text{H}_2\text{O} + e^-$ differential cross-section $\sigma_{\text{diff}}(\theta_e, \text{eKE})$ on the scattering angle θ_e , which peaks very strongly in the forward direction (i.e. near $\theta_e = 0^\circ$) [170, 168]. Specifically, in the vicinity of 2 eV, the differential cross-section for $\text{H}_2\text{O} + e^-$ forward scattering is estimated to exceed that for backward scattering ($\theta_e = 180^\circ$) by about two orders of magnitude (Fig. 1 in Ref. [168]). In other words, the trajectories of most electrons scattered by H_2O are affected rather little.

In contrast, the $\text{N}_2\text{O} + e^-$ scattering dynamics in the same energy range are dominated by the $^2\Pi$ symmetry N_2O resonance [149]. One might think of the resonance as an

absorber, which reemits the scattered electrons in varying directions, subject to the conservation of energy and angular momentum [148]. Accordingly, the $\text{N}_2\text{O} + e^-$ differential cross-section shows nearly equal probabilities for forward and backward scattering near the resonance maximum [Fig. 3(a) in Ref. [147]]. Hence, the electron trajectories get scrambled by the interaction with N_2O in the vicinity of the anionic resonance.

These scattering features align well with the stronger decay of photodetachment anisotropy observed with N_2O solvation, despite the larger total cross-section of H_2O . Furthermore, we conclude that the total scattering cross-section is not necessarily a good measure for evaluating the solvent effects on the PADs in cluster anion photodetachment. Obtained by integrating the differential cross-section over all scattering angles, $\sigma(\text{eKE})$ does not reflect the most relevant details of the interaction between the emitted electrons and the solvent molecules. A more appropriate measure is the momentum-transfer (or "diffusion") cross-section $\sigma_m(\text{eKE})$, calculated by integrating $\sigma_{\text{diff}}(\theta_e, \text{eKE})$ with a $(1 - \cos \theta_e)$ weight function [17]. The $\sigma_m(\text{eKE})$ cross-section assigns a greater weight to scattering events that significantly alter the electron trajectories (and thus affect the PAD) and discounts small-angle scattering contributions.

The momentum-transfer cross-sections for electron collisions with H_2O and N_2O are plotted as solid curves in Figure 6.8(c), using the results of Refs. [170] and [147], respectively. For N_2O , $\sigma_m(\text{eKE})$ is not very different from the corresponding total cross-section, implicating that most $\text{N}_2\text{O} + e^-$ collisions in the relevant energy range are "momentum-transfer" collisions. For $\text{H}_2\text{O} + e^-$, however, σ_m is reduced by orders of magnitude relative to σ , as most scattering events are long-range electron-dipole

interactions, not causing significant changes to the electron trajectories.

The normalized anisotropy differentials for the N_2O and H_2O solvents, shown in Figure 6.8(b), mirror the main trends of the corresponding momentum-transfer cross-sections in Figure 6.8(c). For N_2O (Sets 1–5), $D(\text{eKE})$ peaks near the ${}^2\Pi$ resonance maximum, while the less significant anisotropy loss in $\text{NO}^-(\text{H}_2\text{O})_n$ is consistent with the smaller $\sigma_m(\text{eKE})$ values for H_2O . While the agreement is by no means quantitative, it does bring out the role of the N_2O resonance.

A major limitation of the above analysis is the empirical nature of Equation 6.4. In addition, one must consider that electron-solvent scattering interactions in cluster anion photodetachment occur in the short range, while the measured eKEs correspond to final (far-field) energies of the detached electrons. Assuming attractive electron-neutral interactions, the effective energy of the outgoing electrons in the solvent-scattering process is greater than the measured eKE, which should result in a red-shift or red-wing broadening of the scattering profile. This effect possibly contributes to the low-eKE slope of $D(\text{eKE})$ in Figure 6.8(b), which extends beyond the unsolvated resonance curve. Resonance broadening by the cluster environment and collective many-body effects are also likely to contribute to the broadening of the $D(\text{eKE})$ curve [16, 171].

The suggested role of the N_2O^- resonance echoes with the past work on solvated iodide cluster anions, in which a marked loss of anisotropy with a single CH_3I solvent molecule implicated a CH_3I^- scattering resonance [140]. In general, we believe that in many cases the solvent-induced reduction of photoelectron anisotropy can be traced to a large electron-solvent momentum-transfer cross-section, such as expected in the case of a resonance found in the outgoing photoelectron energy range. As one more case in point,

a marked loss of photodetachment anisotropy upon solvation was previously observed by our group for the $(\text{OCS})_n^-$ cluster anions. Although we did not explicitly comment on it at the time, the trend is clearly seen in the outer rings of the 400 nm photoelectron images of $(\text{OCS})_n^-$ in Fig. 1 in Ref. [172]. In that case, eKE falls in the vicinity of the $^2\Pi$ shape resonance of OCS peaking at 1.15 eV [173]. This example is particularly relevant here, because of the similarities between OCS and N_2O , including their structures and electron affinities.

6.5 Summary

Photoelectron images of solvated NO^- obtained at several laser wavelengths reveal a greater reduction in the photodetachment anisotropy in the presence of N_2O solvent molecules, compared to H_2O . The effect is attributed to an N_2O solvent anionic resonance that falls within the departing electron kinetic energy range. The momentum-transfer cross-section, rather than the total scattering cross-section, is shown to be a better predictor of the solvent effects on the photoelectron angular distributions in these cluster anions.

CHAPTER 7

OBSERVATION OF THE CH_3SOCH^- AND $\text{CH}_3\text{SOCH}^- \cdot \text{H}_2\text{O}$ ANIONS: A PHOTOELECTRON IMAGING AND PHOTOFRAGMENTATION STUDY

7.1 Introduction

Organosulfur radicals and compounds often appear as reaction intermediates of great importance to synthetic chemistry. For instance, sulfur-substituted carbanions are used on modern synthetic methodologies mediating many C–C bond forming reactions [174]. Gas-phase techniques allow for the direct observation of many of such species on their isolated form while permitting the characterization of their intrinsic properties and aiding the discovery of new radicals and intermediates.

Dimethyl sulfoxide (DMSO, CH_3SOCH_3), like many polar organic molecules, exists in anionic form only as a dipole-bound anion [175, 176, 177, 178], where the excess electron is weakly bound in a diffuse orbital by virtue of the strong dipolar interaction. On the other hand, it is well known that deprotonation of such molecules provides a binding site for the excess electron, producing valence anions of the $[\text{M}-\text{H}]^-$ type (base anions), where M refers to the parent neutral [179]. For instance, proton abstraction from DMSO forms the well-known dimethylsulfinyl carbanion (or dimsyl anion) $\text{CH}_3\text{SOCH}_2^-$. Numerous applications of this anionic species have been reported since its first observation by Corey and Chaykovsky [180] highlighting its great synthetic capabilities.

Theoretical [181, 182] and experimental [183] studies on the dimethyl sulfide anion show that the excess charge is mostly localized on the carbon of the CH_2 fragment. This additional electron is paired with a second valence electron in the hybridized non-bonding orbital of carbon. The anion possesses a pyramidal C-S(O)-C configuration with an electron lone pair localized on the sulfur atom and a highly polarized S^+-O^- bond. Compared to neutral DMSO, where both S-C bonds are 1.80 Å, the S-CH_2 bond length of the anion is slightly compressed (1.72 Å) while the S-CH_3 distance is somewhat stretched (1.84 Å) (see for example [182]). Wolfe et al. [181] attributed this effect to the stabilizing orbital interactions between the non-bonding electrons in the carbon atom and the orbitals of sulfur. More recent work by Streitwieser and co-workers [184, 182] suggests that this effect may arise primarily from the electrostatic stabilization of the anionic carbon center in proximity to the positively charged S atom of the polarized sulfinyl group. As a result of this unique structural arrangement, the potential tridenticity of this anion has been suggested based on possible O, S, and C nucleophilic reactivity [185].

Despite the long interest in this anion, however, to the best of our knowledge no reports have been made for the $[\text{M-2H}]^-$ anions of DMSO. Reactions of the oxide radical anion O^- have proven to be a practical approach to synthesize a variety of radical anions in the gas-phase [179, 186]. In addition to its ability for proton abstraction, O^- is also capable of abstracting H_2^+ from a wide range of molecules due to its high proton and hydrogen affinities [186]. In this study, we make use of this property to generate novel $[\text{M-2H}]^-$ anions of DMSO. Resulting anionic species could either be described as CH_3SOCH^- or $\text{CH}_2\text{SOCH}_2^-$ depending of whether the O^- attack occurs to the hydrogens from a single carbon or from both carbon centers, respectively. The similar CH_3COCH^-

and $\text{CH}_2\text{COCH}_2^-$ anions have been observed upon 1,1 and 1,3 H_2^+ abstraction from neutral acetone by O^- [187, 188]. The photoelectron imaging results presented in this work, in combination with a thorough analysis of the observed photofragments, suggest that anions of the CH_3SOCH^- form are predominantly formed in our experimental setup, with the excess electron residing in the out-of-plane p carbon orbital of the bent SCH segment.

Photodetachment from CH_3SOCH^- reveals the carbene character of the remaining $\text{CH}_3\text{SO}\ddot{\text{C}}\text{H}$ neutral. Carbenes are known reactive intermediates where the divalent carbon leads to low-lying singlet and triplet states. Although close in energy, these states exhibit noticeable differences in their chemical reactivity (see for example [189]). By using photoelectron spectroscopy, in combination with *ab initio* and density-functional calculations, we determine the electronic structure of the CH_3SOCH^- anion and its neutral. Photofragmentation experiments on this anion reveal two types of products, namely HCSO^- and SO^- . Although direct S–C bond cleavage is responsible for the HCSO^- fragments, a photoinitiated intracuster C–C bond formation, mediated by the nucleophilic reactivity of the CH segment with the near by CH_3 group, is proposed as a likely mechanism for the formation of the SO^- products. The effect of monohydration on the CH_3SOCH^- anion is also studied by monitoring the changes induced on the photoelectron spectra as well as on the fragmentation patterns.

7.2 Experimental Setup

The experiments are carried out on a negative ion tandem time-of-flight mass-spectrometer that is equipped with a photoelectron imaging assembly as described in Chapter 2. The anions are formed by bubbling 25 psi of neat N_2O gas through a

reservoir containing liquid dimethyl sulfoxide (Alfa Aesar 99+%). Gas molecules are expanded into vacuum through a 50 Hz pulsed nozzle. Slow secondary electron attachment to neutral nitrous oxide is used as a precursor of atomic O^- radicals via the well-known dissociative electron attachment process to N_2O . We therefore propose a formation mechanism where atomic O^- abstracts an H_2^+ from neutral DMSO to generate the $[M-2H]^-$ anion plus an H_2O molecule. Water trapped within the gas delivery lines serves as additional source of H_2O for the formation of anionic hydrates. The suggested mechanism for cluster ion formation is:



with $k \geq 0$. The anions are pulse-extracted into our Wiley-McLaren type TOF mass-spectrometer and detected using an in-line microchannel plate (MCP) detector mounted at the end of the flight-tube. Mass-selected ions are then intersected by a pulsed laser beam. The harmonics of a nanosecond Nd:YAG laser (Spectra Physics, Inc., Quanta-Ray Lab 130-50) provide 532, 355, and 266 nm pulses of about 30, 15, and 5 mJ/pulse respectively. The laser beam is mildly focused at the intersection with the ion beam using a 2 m. lens located 1.7 m. before the interaction region.

Resulting anionic photofragments are analyzed by our linear reflectron mass spectrometer and refocused on an off-axis MCP detector. The photofragment mass spectra is captured by a digitizing oscilloscope, averaged over 512 laser shots, and transferred to a computer. Photoelectron images are recorded in the direction perpendicular to the ion and laser beams. A 40 mm diameter MCP detector coupled to a P43 phosphor screen is mounted at the end of the μ -metal shielded electron flight tube. To discriminate against background the MCPs are pulsed for a 200 ns window timed with the arrival

of the photoelectrons. Photoelectron images are then recorded by a CCD camera for $\sim 50,000$ experimental cycles and transferred to a computer for storage and analysis. The well-known electron affinity of O^- [112] is used for calibration.

7.3 Results

A representative parent-ion mass spectrum is shown in Figure 7.1. In addition to the anticipated anions formed by expansion of N_2O gas with a small H_2O amount present in the gas line [142, 162, 152], the observed peaks at $m/z = 76, 94$, and 112 suggest a hydration series for the $m/z = 76$ anion, assigned as the $[\text{M}-2\text{H}]^-$ negative ion of DMSO and described throughout this Chapter as CH_3SOCH^- . Other observed anions that are based on the ionization of DMSO are SO^- and small amounts of HCSO^- corresponding to $m/z = 48$ and 61, respectively. Although the peak at $m/z = 94$ may also correspond to the $\text{CH}_3(\text{SO}_2)\text{CH}_3^-$ anion resulting from the addition reaction of the atomic oxygen anion to DMSO, the photoelectron images presented below show no evidence that such compound is being formed.

7.3.1 Photoelectron Imaging of CH_3SOCH^- , CH_3SOCH^- , and HCSO^-

Figure 7.2 (left column) shows the raw photoelectron images taken for the CH_3SOCH^- anion at 355 nm and for the $\text{CH}_3\text{SOCH}^-(\text{H}_2\text{O})$ ionic complex at 266 nm. The images were acquired under the same electrostatic focusing conditions and their corresponding energy spectra are displayed in the right column of Figure 7.2. The photoelectron kinetic energies and angular distributions are extracted from the reconstructed images using the BASEX program developed by Dribinski et al. [26]. Three evident transitions are

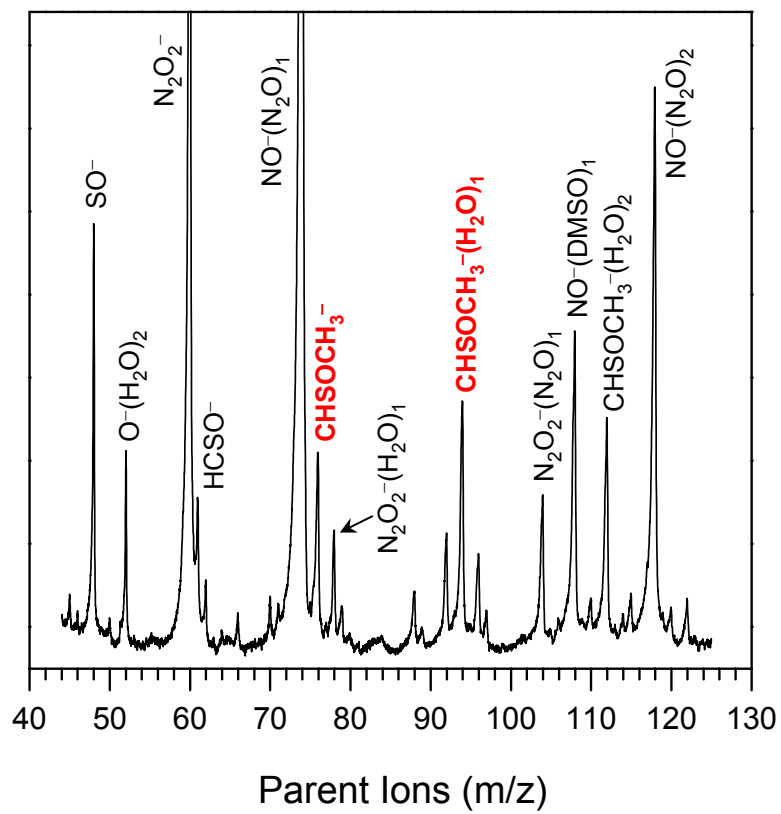


Figure 7.1: Representative mass spectrum displaying the $\text{CH}_3\text{SOCH}^-(\text{H}_2\text{O})_n$ anions.

observed in each case corresponding to the different rings on the displayed images and their corresponding bands on the spectra. The 355 nm photoelectron energy spectrum of CH_3SOCH^- , shown in Figure 7.2(c), includes a resolved band centered at 3.48 eV that is taken from the image acquired at higher photon energy (266 nm). The rest of the 266 nm trace overlaps directly with the one obtained at 355 nm and therefore is not shown. The 355 nm image is selected to visualize the effects of the photon energy and because of its better resolution. The extracted anisotropy parameter values, starting from the outer ring, are 0.15, 0.03, and 0.49 for CH_3SOCH^- and 0.29, 0.26, and 0.95 for $\text{CH}_3\text{SOCH}^-(\text{H}_2\text{O})$.

The CH_3SOCH^- spectrum was fitted to the sum of three Gaussian functions whose peak values correspond to electron binding energies ($e\text{BE}_{\text{max}} \approx \text{VDE}$) of 1.8, 2.48 and 3.48 eV, respectively. Assignment of these bands to the corresponding electronic transitions is given in detail in detail in Section 7.4.1. In brief, under the C_1 symmetry of the parent anion, the lowest eBE band is assigned to the $X^1\text{A}$ state of the neutral, the middle band to the excited triplet state $a^3\text{A}$, and the high eBE band is tentatively assigned to an excited singlet. From the spectrum of the monohydrated anion shown in Figure 7.2(d), we observe that all three bands are equally shifted to higher binding energies by 0.54 ± 0.05 eV with respect to the bare anion. The shift is attributed to the stabilization interaction between the anion and the solvent H_2O molecule. Because of the direct one-to-one correspondence in the transitions observed for the photoelectron spectra of the bare and monohydrated species, we conclude that no $\text{CH}_3\text{SO}_2\text{CH}_3^-$ anions, which have the same mass as $\text{CH}_3\text{SOCH}^-(\text{H}_2\text{O})$, are formed in our experimental setup.

Figure 7.3 shows the 355 nm photoelectron image of the small HCSO^- peak observed in our parent ion mass spectrum at $m/z = 61$. The VDE of this anion, obtained from

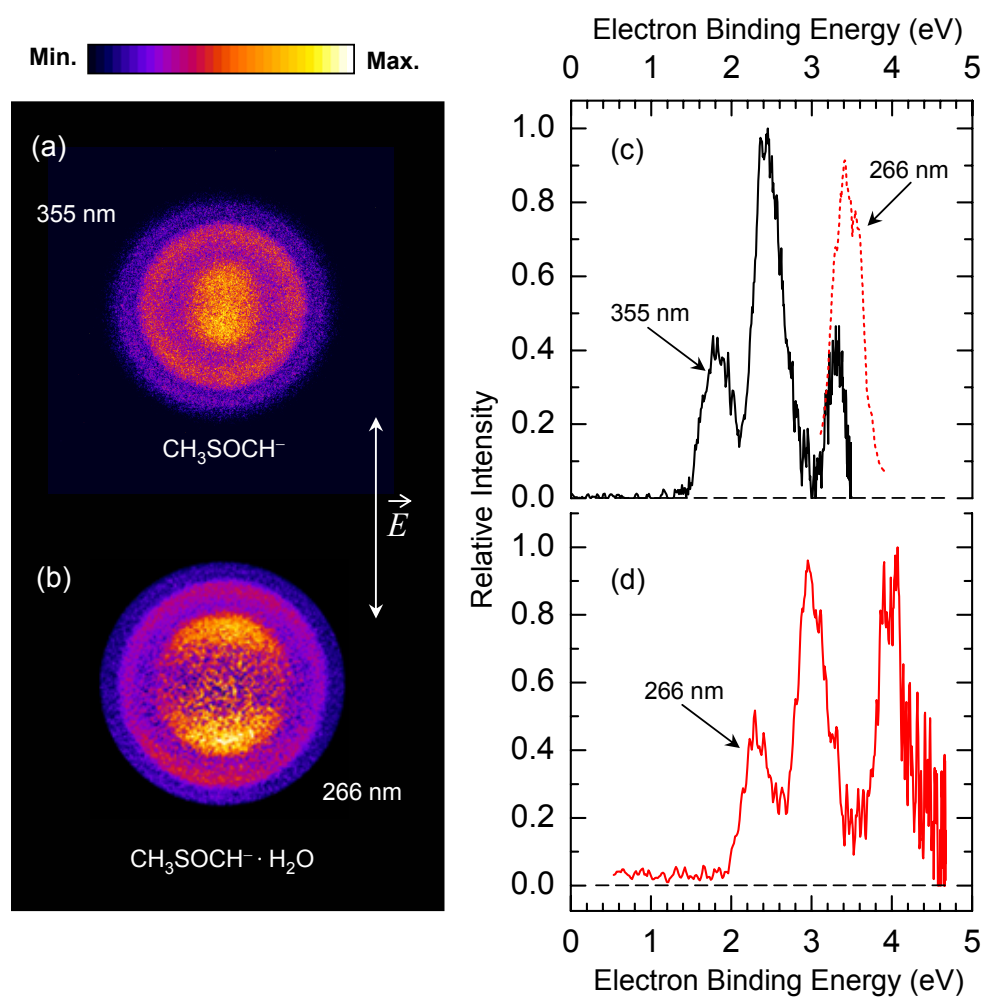


Figure 7.2: Raw photoelectron images (left) and corresponding energy spectra for the CH_3SOCH^- and $\text{CH}_3\text{SOCH}^- \cdot \text{H}_2\text{O}$ anions. The double arrow indicates the laser polarization.

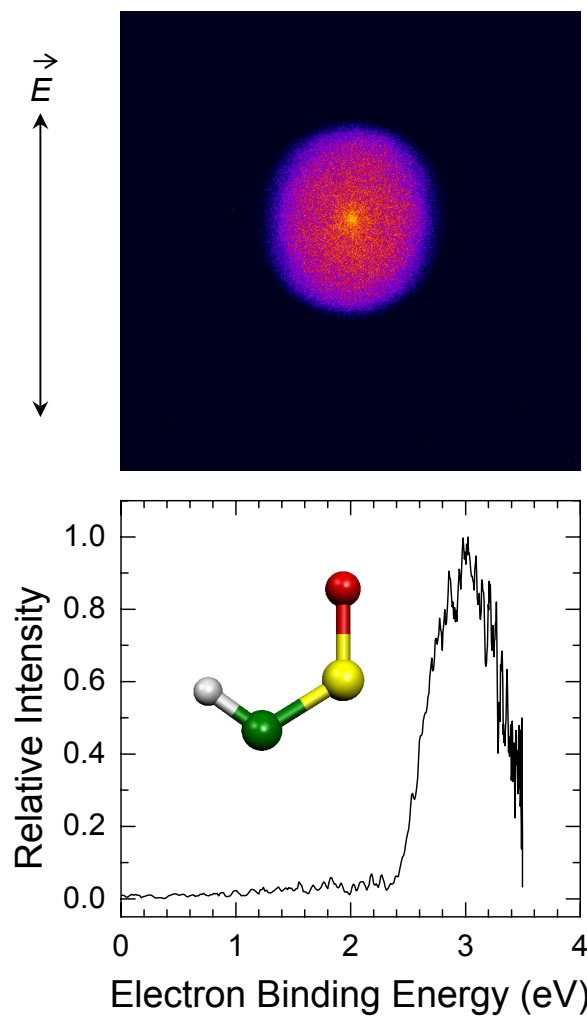


Figure 7.3: Raw photoelectron image (left) and corresponding energy spectrum for the HCSO^- anion acquired at 355 nm. The double arrow indicates the laser polarization. The inset shows the optimized structure for the anion. The calculated VDE at the B3LYP/aug-cc-pVTZ level of theory is 3.19 eV, in good agreement with the experimental value.

the eBE associated with the maximum of a Gaussian fit to the photoelectron band, is 2.97 eV with a FWHM of ~ 0.8 eV. Characterization of this anion becomes relevant to the understanding of the photodissociation channels discussed in the next section, since methyl elimination from CH_3SOCH^- results in the HCSO^- anion. Our calculations suggest that the anion responsible for this spectrum has a *cis*- configuration and a singlet ground state. The calculated VDE at the B3LYP/aug-cc-pVTZ level of theory is 3.19 eV, in good agreement with the experimental value. This spectrum is significantly different than the one reported for the $\text{CH}_3\text{CH}_2\text{S}^-$ anion [190], ruling out this possibility for the assignment of the $m/z = 61$ peak.

7.3.2 Photofragmentation Spectra

Reported in Figure 7.4 are the anionic photofragment mass spectra obtained with 532 nm photoexcitation of the CH_3SOCH^- and $\text{CH}_3\text{SOCH}^-(\text{H}_2\text{O})$ anions. A dominant HCSO^- ($m/z = 61$) photofragment peak is observed for both cases with additional contributions from SO^- based fragments. For the bare CH_3SOCH^- anion, the HCSO^- products account for about 90% of the measured total fragmentation yield, where the minor SO^- photofragments account only for about 10%. No dissociation products were observed by excitation with 355 nm or 266 nm light. It is interesting to compare this result with the CH_3COCH^- anion formed from acetone, where a main HCCO^- fragmentation channel was observed by Lin and Grabowski [187].

Intriguingly, the monohydrated anion presents a much more enhanced yield for the SO^- based channel, including an $\text{SO}^-(\text{H}_2\text{O})$ fragment as shown in Figure 7.4. This last photofragment reveals that the water molecule binds to the sulfoxide group by means of

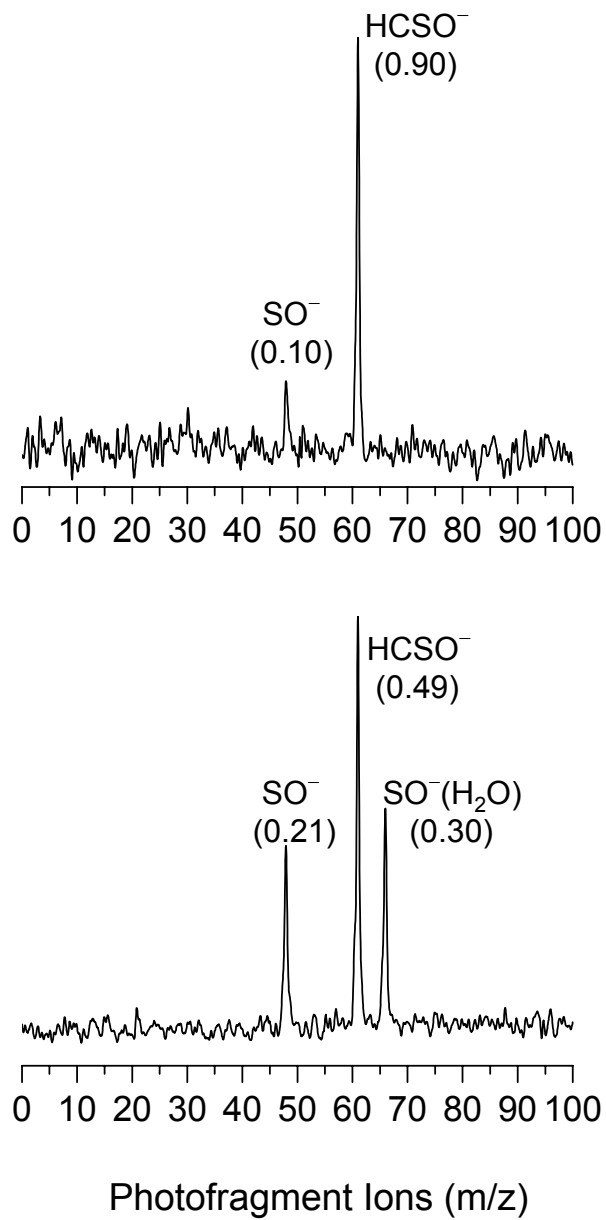


Figure 7.4: 532 nm photofragment mass spectrum of parent CH_3SOCH^- and $\text{CH}_3\text{SOCH}^- \cdot \text{H}_2\text{O}$ anions. The number in parenthesis are the relative yields for the different fragments.

H bonding to the oxygen atom. For this anionic complex, the combined yield for the SO^- based products accounts for about 51 % of the fragmentation yield, with the remaining 49 % attributed to HCSO^- .

7.3.3 Isomeric Structures and Computational Results

To aid the analysis of the experimental data, minimum energy structures were located using the Gaussian03 suite of programs [191] running on The University of Arizona high performance computing system. The hybrid B3LYP method was employed for most of the calculations shown in this work using the aug-cc-pVTZ basis set. Calculations at the MP2 and CCSD(T) level were consistent with the energetic orderings of our DFT calculations varying only slightly on their respective relative energies. The obtained global minimum energy structures are displayed in Figure 7.5. No imaginary frequencies were found for those optimized geometries at the B3LYP/aug-cc-pVTZ level of theory.

Vertical detachment energies for the anions shown in Figure 7.5 corresponding to the low-lying singlet and triplet states of the neutral are calculated by performing a single-point energy calculation using the minimum energy structure obtained for the anion. The resulting single point energies for the neutral are then subtracted from that of the ground state anion to obtain the VDEs shown in Table 7.1.

We now focus on structure I, which best matches the experimental photoelectron spectra and is also consistent with the observed photofragments—in particular with formation of the HCSO^- fragments. The optimized HC–S distance is 1.72 Å, which shows no variation compared to the H_2C –S distance for the dimsyl anion (1.72 Å from [182]). This is an indication that no changes occur to the C–S bonding between these

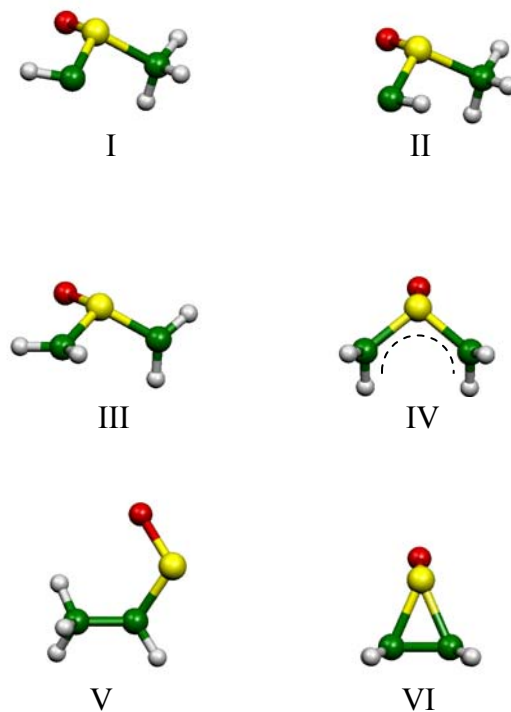


Figure 7.5: Optimized structures at the B3LYP/aug-cc-pVTZ level of theory.

Table 7.1: Energies and VDEs obtained with B3LYP/aug-cc-pVTZ.

	Energy (Hartrees)	Relative Energy (eV)	VDE (eV)	
			singlet	triplet
I	-552.031146	0.0	1.967	2.522
II	-552.026963	0.114	2.026	2.573
II	-552.029071	0.057	2.486	2.40
IV	-552.032491	-0.037	2.270	2.525
V	-552.100545	-1.89	0.944	2.300
VI	-552.056532	-0.691	-0.353	
Exp.			1.80	2.48

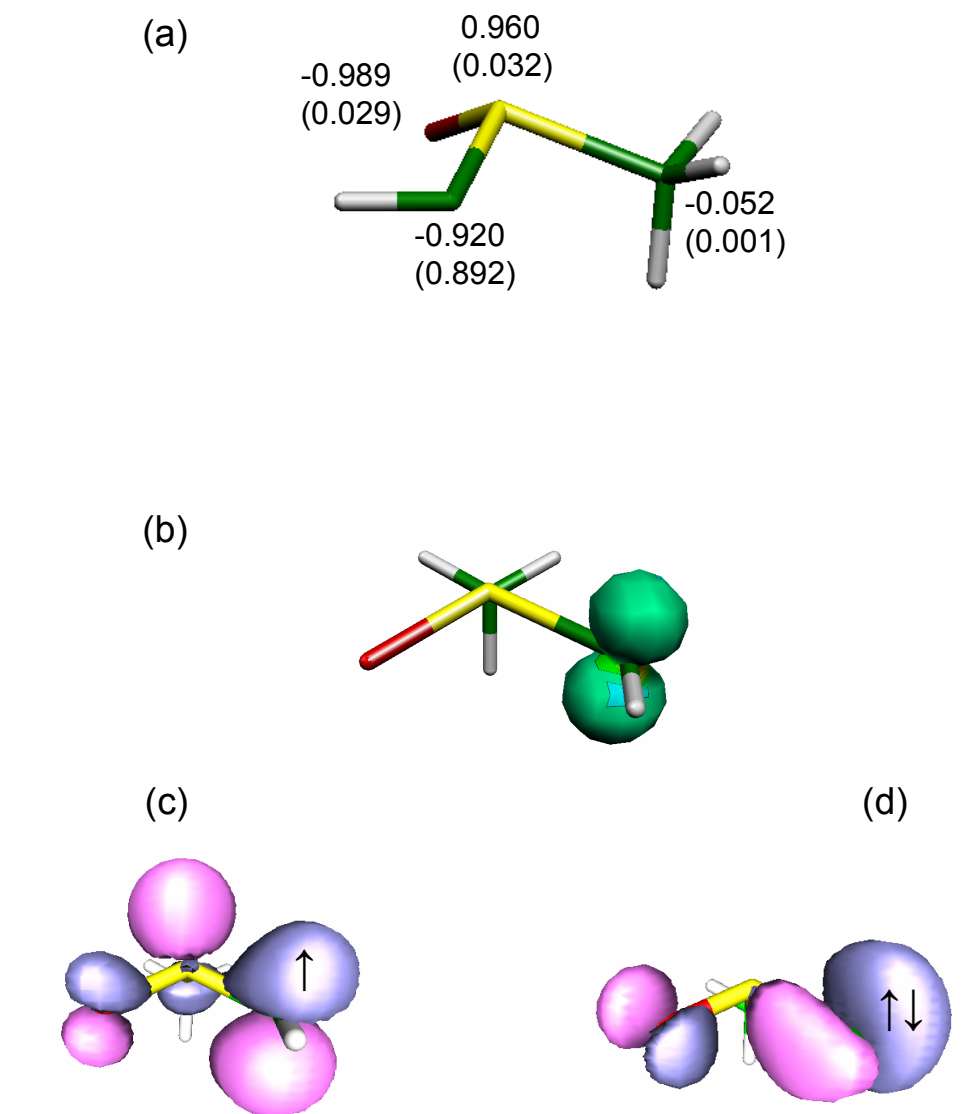


Figure 7.6: (a) Mulliken charges (top) and spin densities (bottom) for CH_3SOCH^- obtained at the B3LYP/aug-cc-pVTZ level of theory; (b) spin density contour plot ($\alpha-\beta$) showing the location of the unpaired electron; (c) HOMO; (d) HOMO-1.

two anions. The extra electron then occupies the empty out-of-plane orbital of the carbon atom. The obtained Mulliken spin densities and charges shown in Figure 7.3.2 are consistent with this picture and also show the highly polarized S–O σ -bond, best described as S^+O^- [192]. The S–O bond length of the optimized anion is 1.55 Å, which is also similar to that of dimethyl sulfide, both being longer than the 1.49 Å S–O bond distance of neutral DMSO (see for example [182]).

7.4 Discussion

7.4.1 Photodetachment Bands

Three main photoelectron bands were observed in the spectra displayed in Figure 7.2. The calculated VDEs for structure I, reported on Table 7.1, are in best agreement with the observed photoelectron spectrum displayed in Figure 7.2(c). For instance the experimental VDEs for the first two bands are 1.80 and 2.48 eV, respectively, compared to the calculated (B3LYP/aug-cc-pVTZ) VDEs corresponding to the ground singlet (1.97 eV) and excited triplet (2.52 eV) states of the neutral. For comparison, the VDEs obtained with the anion reoptimized at the MP2/aug-cc-pVTZ level are 2.10 and 2.66 eV for the singlet and triplet transitions, respectively. The CCSD(T)/aug-cc-pVDZ calculations using this re-optimized MP2 structure give 1.75 eV as the VDE of the singlet band and 2.36 eV for the triplet. Contributions from the symmetric $CH_2SOCH_2^-$ anion (structure IV in Figure 7.5) are not evident from the observed photoelectron spectra, although the predicted transitions would fall mostly in between the bands of structure I, and possible weak contributions could have been disguised as baseline noise.

Photodetachment from the CH_3SOCH^- anion (structure I) leaves either singlet or

triplet carbenes. Results from our molecular orbital calculations indicate that the lowest eBE band corresponds to removal an electron from the singly-occupied HOMO of the anion (out-of-plane p orbital), resulting in a neutral that can be viewed as a singlet carbene with two nonbonding paired electrons located on the in-plane sp^2 hybridized orbital of the divalent carbene center. Geometry optimization of this singlet neutral state reveals that the carbene is further stabilized by electron donation from the sulfur substituent into the empty p orbital of carbon, ultimately resulting in a planar C–(SO)–C skeleton with a much shorter HC–S bond length (1.58 Å compared to 1.72 Å for the anion) originating from the additional π C–S bonding. The adiabatic electron affinity (without zero-point energy correction) is estimated to be 1.18 eV at the B3LYP/aug-cc-pVTZ level of theory.

The middle band in the photoelectron spectra, assigned to the excited triplet of the neutral, results after removal of a β -electron from the HOMO-1 of the anion (the in-plane sp^2 hybridized orbital shown in Figure 7.3.2(d)), leaving a triplet carbene center. The geometry of the optimized triplet structure shows the most variation in the \angle SCH angle compared to that of the anion, opening from 105° to 123° according to our B3LYP/aug-cc-pVTZ calculations. It is interesting to notice that the geometry relaxation on this state does not result in a linear S–C–H configuration. The third band, corresponding to the highest binding energy, is tentatively assigned to a high energy singlet of the neutral. Our excited state calculations for the neutral molecule at the optimized geometry of the anion give excitation energies for the next singlet of 1.99 eV for CIS/aug-cc-pVTZ 1.99 eV, 1.52 eV for TD-B3LYP/aug-cc-pVTZ, and 1.54 eV for SAC-CI/6-311+G*. Assuming that the first band is located at 1.8 eV these calculations predict that removal of an α -electron from the HOMO-1 of the anion should result in

photoelectrons in the 3.3–3.8 eV energy range which is consistent with the experimental data. However, the markedly positive anisotropy of this transition, compared to the other two rings, is somewhat puzzling, hence the tentative nature of our assignment. The spectrum recorded for the monohydrated anion shows that all three bands are shifted to higher binding energies by an equal amount (0.54 ± 0.05 eV), attributed to the stabilization induced on the anion by a solvent water molecule.

Of crucial importance to carbene chemistry is the accurate determination of the singlet-triplet energy gap, and photoelectron spectroscopy of negative ions has proven to be a valuable technique for the experimental determination of this energy difference. Characterization of the singlet and triplet states of neutral carbenes by means of anion photodetachment has been reported previously by Lineberger and co-workers for several systems, including CH_2^- [193, 194], halocarbene anions HCX^- , X=halogen, and the HCCN^- and HCNC^- isomeric anions [195].

7.4.2 Dissociation Mechanisms

Figure 7.8 displays a schematic reaction coordinate diagram showing the relative energies (calculated at the B3LYP/aug-cc-pVTZ level of theory) for the isomers shown in Figure 7.5 and their connections to the plausible mechanisms leading to the formation of HCSO^- and SO^- photofragments.

The HCSO^- products are proposed to originate from direct S–C bond cleavage followed by methyl elimination from the CH_3SOCH^- anion. The mechanism for SO^- production, however, is less clear and several possible mechanisms are discussed below:

- (i) Decomposition of HCSO^- photofragments into $\text{SO}^- + \text{CH}$. A mechanism similar

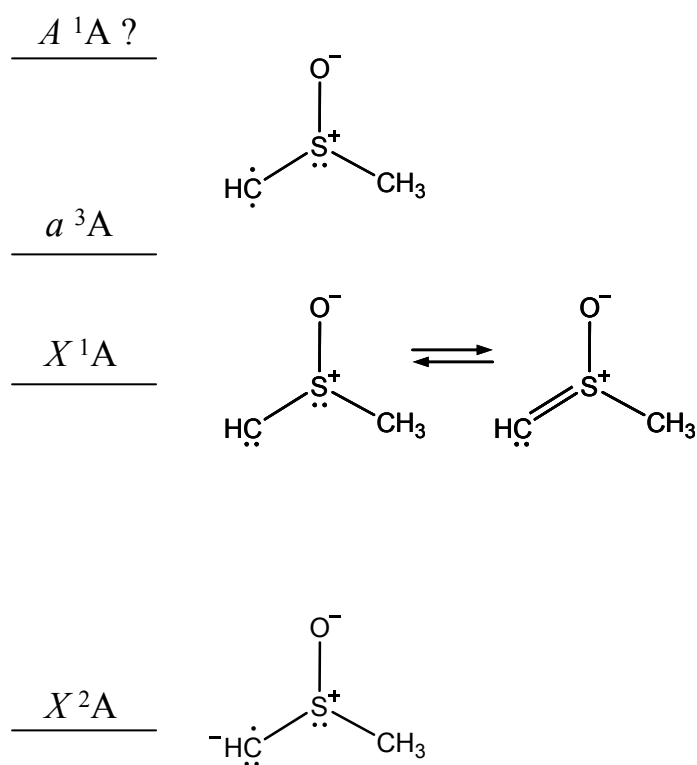


Figure 7.7: Schematic picture of the states involved in photodetachment from the CH_3SOCH^- anion.

to the production of CO from CH_3COCH_3 , where the fragmentation of the CH_3CO photoproduct [196, 197] is attributed as the source of the observed carbonyl fragments. Further decomposition of nascent HCSO^- products is therefore explored as a possible mechanism for SO^- formation.

- (ii) Concerted two bond breakage to give $\text{CH} + \text{SO}^- + \text{CH}_3$ after absorption of a photon by CH_3SOCH^- (or by the symmetric $\text{CH}_2\text{SOCH}_2^-$ anion to give $\text{SO}^- + 2\text{CH}_2$). A recent study shows concerted bond-breaking of DMSO upon UV excitation as a possible pathway for the production of $\text{SO} + 2\text{CH}_3$. [198].
- (iii) A nucleophilic attack by the electron lone-pair on CH to the carbon of the methyl group, promoting methyl migration from the sulfur atom to the carbon of CH forming the CH_3CHSO^- anion. Subsequently, S–C bond cleavage can potentially result in $\text{CH}_3\text{CH} + \text{SO}^-$ provided there is enough energy available in the system.
- (iv) Intramolecular C–H insertion resulting in a cyclic anion that undergoes decomposition into $\text{C}_2\text{H}_4 + \text{SO}^-$. Since neutral ethylene episulfoxide is a well-known pyrolytic [199] (or photolytic [200]) source of SO radicals, this anion analog is therefore studied as a possible source of SO^- .

Our calculations indicate that HCSO^- anion is pronouncedly more stable than the combined $\text{SO}^- + \text{CH}$ fragments as shown in Figure 7.8, making (i) a not so strong argument. In addition to this, no $\text{HCSO}^-(\text{H}_2\text{O})$ fragments were detected that could explain the observed $\text{SO}^-(\text{H}_2\text{O})$ product based on pathway (i) alone. Mechanism (ii) is also not very likely since there is not enough energy provided by the absorption of a single 532 nm photon to break two bonds simultaneously. A photoinitiated methyl migration, as

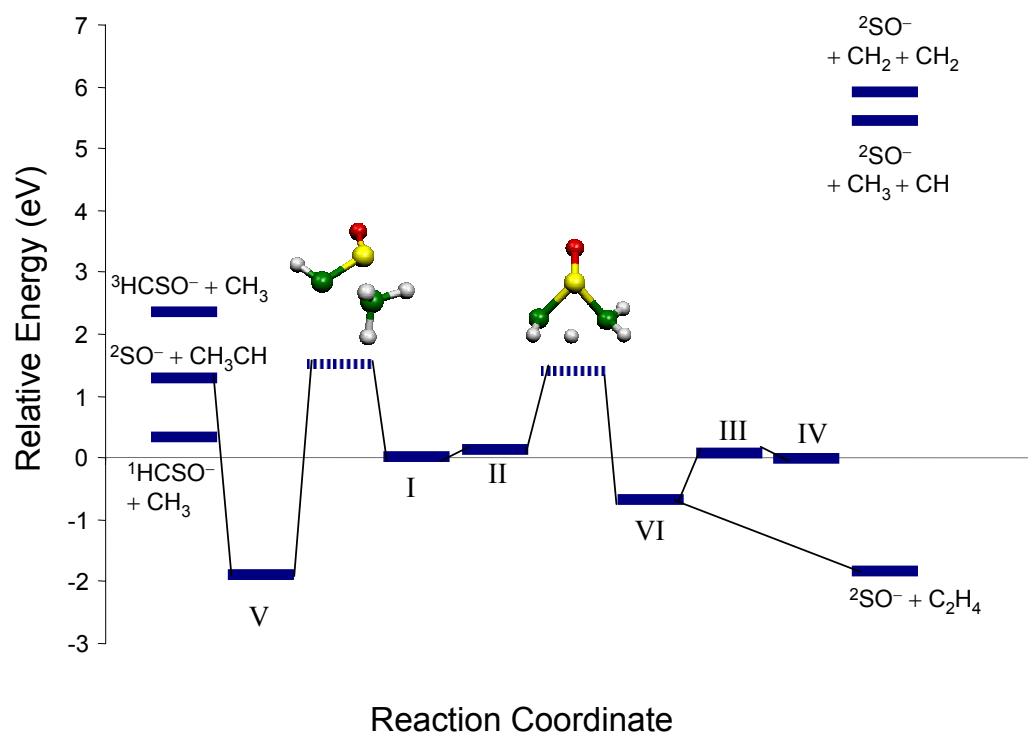


Figure 7.8: Schematic reaction coordinate calculated at the B3LYP/aug-cc-pVTZ. Two transition states are shown in striped lines, corresponding to C or H nucleophilic attack by the lone pair on the CH carbon.

suggested in (iii), seems to be energetically accessible at this photon energy and remains as a possible pathway in this discussion. Mechanism (iv) is also highly favored based on energetic arguments. Bowie et al. [201] reported that the HOS^- fragment that was observed in their mass spectra originated from the fragmentation of the $\text{CH}_3\text{SOCH}_2^-$ anion (dimethyl). Their proposed mechanism involved proton transfer to oxygen followed by a subsequent cyclization and elimination of the C_2H_4 olefin to give HOS^- . Interestingly, if the proton that is transferred to oxygen originates from the CH_2 group, then we are presented with a very similar situation to the current CH_3SOCH^- case.

A complication with the argument in mechanism (iv) is that the excess electron needs to vacate the out-of-plane p orbital of carbon for the C–H insertion to occur. One possibility is having this electron transferred to the sulfoxide group. Nonetheless, the poor electron affinity of cyclic ethylene episulfoxide does not favor the formation of a valence anion (as it can be seen by the negative VDE calculated for the cyclic structure VI). Nonetheless, the high dipole moment of the cyclic neutral (3.94 D calculated at the B3LYP/aug-cc-pVTZ level) suggests that a dipole-bound state is likely to exist. Dipole-bound states can therefore act as "doorways" into dissociative valence states as demonstrated by studies on nitromethane [66]. The enhancement in the SO^- based products upon hydration may be an indication of an increased electron affinity on the monohydrated cyclic intermediate. In this light, the smaller SO^- signal for the bare anion may be thought of as resulting from the strong competition with autodetachment. It is interesting to notice that our calculated dipole moment for the CH_3SOCH neutral is in the 2.40–2.60 D range, which is right at the 2.5 D threshold necessary for a dipole-bound state [176]. In contrast, the calculated dipole for the monohydrated case was 4.44 D at

the B3LYP/aug-cc-pVTZ level of theory.

The photofragmentation mechanisms presented here may be an incipient indication of the interesting synthetic and mechanistic properties of the CH_3SOCH^- anion. It would be worth examining how this anion reacts with nearby molecules and to explore its potential applications.

7.5 Summary

In this Chapter we report, to the best of our knowledge, the first observation of the CH_3SOCH^- and $\text{CH}_3\text{SOCH}^-\cdot\text{H}_2\text{O}$ anions. Photodetachment reveals singlet and triplet carbenes for the remaining neutral, with the singlet state assigned as the ground state. The proposed structure of the CH_3SOCH^- ion is analogous to that of the well-known dimethyl anion $\text{CH}_3\text{SOCH}_2^-$, with the additional unpaired electron localized in the site of the missing H atom. The photoelectron spectrum of HCSO^- is also observed and reported for the first time in this Chapter.

Two main type of products were found by 532 nm photofragmentation of CH_3SOCH^- , namely, a dominant HCSO^- fragment peak resulting after methyl elimination, and a smaller SO^- product. For the monohydrated anion, an additional $\text{SO}^-(\text{H}_2\text{O})$ fragment was observed. Intriguingly, both this $\text{SO}^-(\text{H}_2\text{O})$ product and SO^- were produced in much higher yields in the fragmentation of $\text{CH}_3\text{SOCH}^-(\text{H}_2\text{O})$ compared to the total yield of SO^- from dissociation of the bare anion. Two possible pathways were proposed as likely mechanisms for the SO^- based photoproducts, both involving a photoinduced intramolecular rearrangement mediated by the highly reactive carbon in the CH group. One involves methyl migration from sulfur to CH, forming a

CH_3CHSO^- anion that is followed by C-S bond cleavage to give $\text{CH}_3\text{CH} + \text{SO}^-$. The other possibility involves a cyclic intermediate that quickly dissociates into $\text{C}_2\text{H}_4 + \text{SO}^-$.

CHAPTER 8

PHOTOELECTRON IMAGING OF ACETONITRILE CLUSTER ANIONS

8.1 Dipole-Bound Anions of CH₃CN

Ground state dipole-bound molecular anions have attracted much attention in recent gas phase ion chemistry studies. These weakly-bound species are often formed when a slow electron becomes attached to a closed-shell neutral molecule through the long-range interaction with the molecular electric dipole moment. A value of $\mu \sim 2.5$ D is generally ascribed as the critical dipole moment required to form a dipole-bound state [176]. Acetonitrile (CH₃CN) was the first dipole-bound state observed, and it was produced by Rydberg electron transfer (RET) to the neutral parent [202]. Theoretical work by Jordan and Wendoloski [203] indicated that the anion consisted of a diffuse electron weakly bound to the neutral molecule, suggestion corroborated experimentally [176]. Later, Johnson and co-workers obtained the photoelectron spectra of the dipole-bound CH₃CN⁻ anion, prepared by photodissociation of the I⁻·CH₃CN complex [204]. Bowen and co-workers independently observed the photoelectron spectra of the [CH₃CN·H₂O]⁻ anion [205]. If the ground state of the CH₃CN⁻ ion is regarded as a technically unperturbed neutral molecule linked to a distant electron which can be easily detached, then the photoelectron spectrum of the CH₃CN⁻ ion should contain only a single sharp feature at the dipole binding energy. However, both Bowen's [205] and Johnson's [204] spectra displayed significant vibrational excitation of the neutral complex during

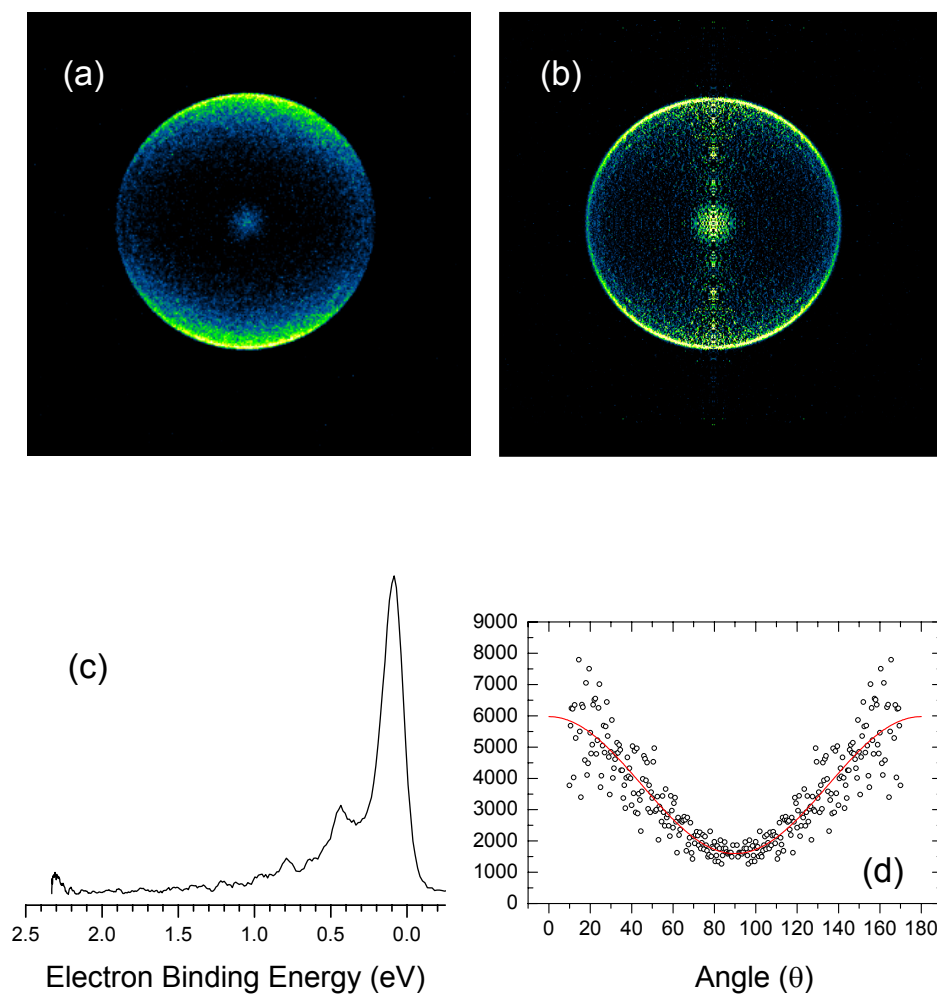


Figure 8.1: (a) raw photoelectron image of the $\text{CH}_3\text{CN}\cdot\text{H}_2\text{O}^-$ anion at 532 nm; (b) Abel-inverted reconstructed image; (c) photoelectron energy spectra; (d) PAD corresponding to $\beta = 0.95 \pm 0.1$.

photodetachment. This vibrational excitation was later attributed by Johnson [204] to a perturbation of the weakly bound electron by the fluctuating dipole moment of the vibrating neutral molecule.

In this Chapter we report the generation of $[\text{CH}_3\text{CN}\cdot\text{H}_2\text{O}]^-$ anions by expansion of argon (30 psi backing pressure) through a heated reservoir containing acetonitrile and some water contamination. The obtained photoelectron image of this $[\text{CH}_3\text{CN}\cdot\text{H}_2\text{O}]^-$ anion is shown in Figure 8.1. Its corresponding photoelectron energy spectra is consistent with the one reported by Bowen and co-workers [205]. The obtained anisotropy parameter of $\beta = 0.95 \pm 0.1$ differs from the expected value of $\beta = 2$ for a detachment from pure *s*-orbital. Reported anisotropies for other dipole-bound anions range from 0.92 for $(\text{H}_2\text{O})_{18}^-$ [206], to 1.4 for dipole-bound anion states of the nucleic acid bases uracil, thymine, and cytosine [207]. The fact that the observed anisotropy is not exactly 2 may be an indication of some p_z character in the diffuse orbital of the electron [176, 207].

8.2 The HCCN^- and H_2CN^- anions

Chemical ionization by O^- gives the HCCN^- and H_2CN^- valence anions [208]. In our experimental setup, secondary electron attachment to N_2O serves as a source of O^- . A typical mass spectrum obtained by expansion of N_2O (20–40 psi) through a reservoir containing liquid acetonitrile is shown on Figure 8.2. The peaks at $m/z = 39$ and 40 are assigned to the HCCN^- and H_2CCN^- anions and are reproducibly formed with good intensity.

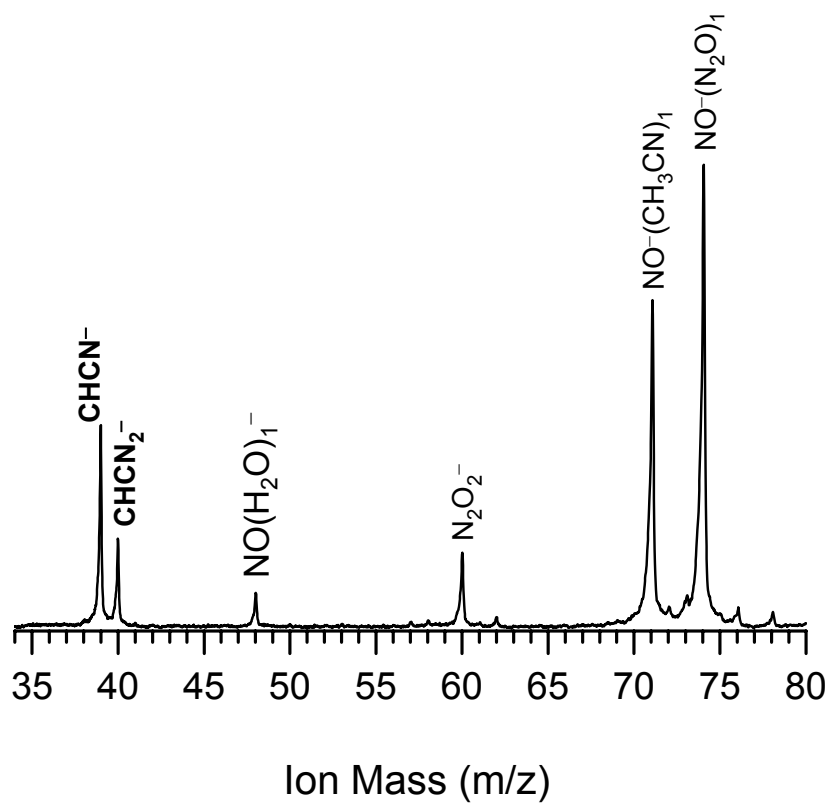


Figure 8.2: Mass spectrum of parent anions, displaying the formation of HCCN⁻ and H₂CCN⁻.

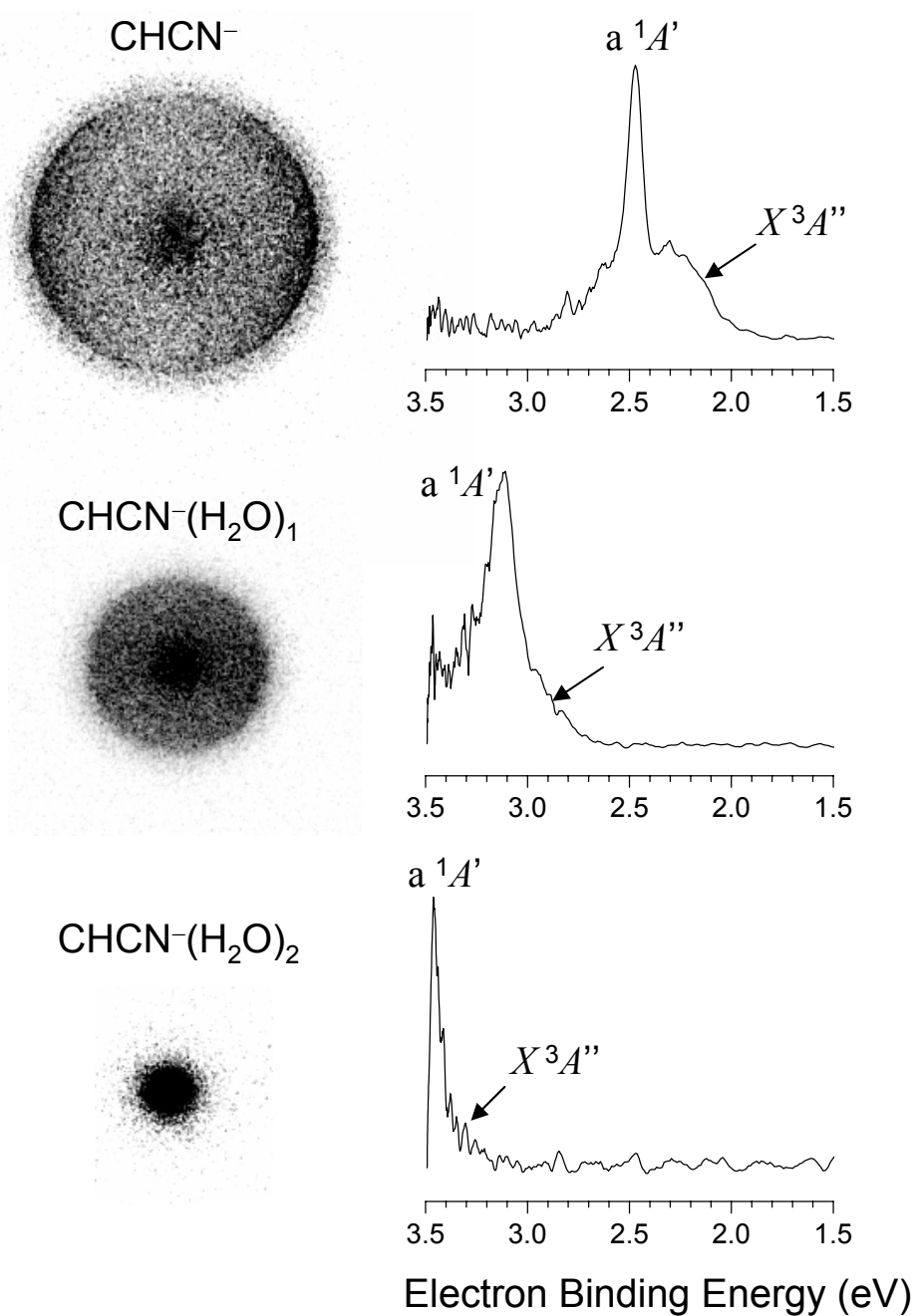


Figure 8.3: 355nm photoelectron images (left) and energy spectra (right) of the $\text{HCCN}^-(\text{H}_2\text{O})_n$, $n = 0 - 2$, Cluster Anions. The measured anisotropy parameters for detachment of HCCN^- give $\beta = -0.8$ for the triplet and $\beta = -0.36$ for singlet states.

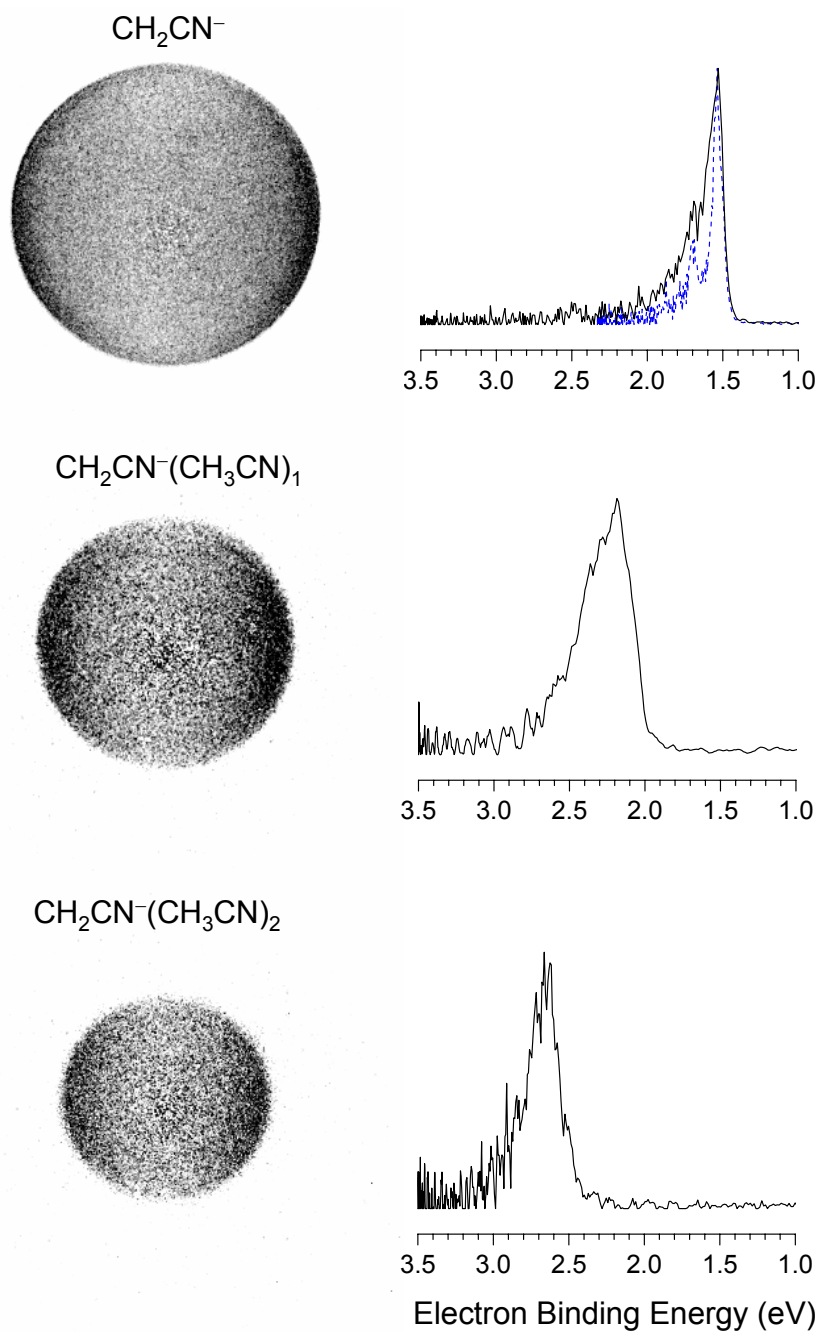


Figure 8.4: 355nm photoelectron images (left) and energy spectra (right) of the $\text{H}_2\text{CCN}^-(\text{CH}_3\text{CN})_n$, $n = 0 - 2$, Cluster Anions.

8.2.1 Photoelectron Imaging of the $\text{HCCN}^-(\text{H}_2\text{O})_n$ Cluster Anions

When larger amounts of water are present in the line, HCCN^- anions are preferentially formed, consistent with Yang et al. [208]. Photoelectron images obtained for this cluster series are displayed in Figure 8.3 along with its corresponding energy spectra. The photoelectron spectrum for HCCN^- has been reported previously by Nimlos et al. [195]. The HCCN^- spectrum shows that detachment from the X^2A'' anion to the X^3A'' state of neutral HCCN exhibits a long progression attributed to the H–CCN bending vibration. This progression is evidence of the linear equilibrium geometry of the triplet HCCN carbene compared to the bent structure of the anion. In addition, detachment to the excited single a^1A' is also observed giving a much narrower peak at higher binding energies. Therefore this singlet state is expected to be bent. The effect of hydration on the observed spectra seems to somewhat narrow the extent of the triplet progression. It would be interesting to investigate if the water solvent presents some changes on the relaxation of the neutral to the linear geometry.

8.2.2 $\text{H}_2\text{CCN}^-(\text{CH}_3\text{CN})_n$ Series

The $\text{H}_2\text{CCN}^-(\text{CH}_3\text{CN})_n$ cluster series are preferentially formed under dry conditions. The photoelectron images and their corresponding spectra are shown in Figure 8.4. The photoelectron spectrum of the H_2CCN^- carbanion was reported previously by [209]. The vibrational structure was attributed to the umbrella mode of the H_2CCN radical. The interesting peak broadening observed for the $\text{H}_2\text{CCN}^-(\text{CH}_3\text{CN})_1$ anion is reproducible under varying source conditions and remains to be studied. Intriguingly, the pronounced broadening disappears for the $\text{H}_2\text{CCN}^-(\text{CH}_3\text{CN})_2$ case.

CHAPTER 9

CONCLUSIONS AND FUTURE OUTLOOK

9.1 Dissertation Summary

A summary of the main accomplishments of this dissertation is presented in this section. Interaction of short laser pulses with anionic clusters can lead to photodetachment or to photofragmentation of the cluster. In this dissertation, we investigate these competing processes by means of photoelectron imaging spectroscopy combined with tandem time-of-flight (TOF) mass spectrometry for ionic fragment determination. Different anionic systems of mass-selected cluster anions are employed to study solvent-dependent changes in structural motifs as well as solvent perturbations to the electronic structure and to the outcomes of the photoinitiated processes. Photoelectron images and fragmentation studies are reported for the $[(\text{CO}_2)_n(\text{H}_2\text{O})_m]^-$ cluster series. For the homogeneous clusters ($m = 0$), the energetics of the photodetachment bands show evidence for cluster core switching between a CO_2^- monomer anion and a covalent $(\text{CO}_2)_2^-$ dimer anionic core, confirming previous observations [79]. Intriguingly, the photoelectron angular distributions (PADs) of the monomer and dimer-based cluster types did not show much variation despite the different nature of their molecular orbitals. A two-center photoelectron wave interference effect was attributed as the plausible model to explain this observations.

Photoelectron images and quantum chemical calculations show a much greater

stabilization of the metastable CO_2^- anion by addition of water solvent molecules, increasing its ability to "trap" an excess electron on CO_2 by virtue of the stabilization interactions with the water network. Most surprising is the effect of the water solvent in quenching the autodetachment channel in excited states normally embedded in the electron detachment continuum (anionic resonances), allowing excited $\text{CO}_2^-(\text{H}_2\text{O})_m$ clusters to follow reaction pathways that lead into cluster fragmentation. Observed $\text{O}^-(\text{H}_2\text{O})_{m-k}$ photoproducts are attributed to photodissociation of the CO_2^- cluster core and are dominant for small parent clusters, whereas a water evaporation channel $\text{CO}_2^-(\text{H}_2\text{O})_{m-k}$ dominates for larger clusters. Addition of a second CO_2 to these clusters is shown to preferentially form $\text{CO}_2^-(\text{H}_2\text{O})_m\text{CO}_2$ clusters in the range of medium to large m . The photodissociation spectra for these clusters exhibit an additional CO_3^- based channel, characteristic of a photo-initiated intra-cluster ion molecule reaction between nascent O^- and the additional CO_2 solvent molecule. As the number of water molecules is increased, the probability of this intra-cluster reaction decreases monotonically as a result of the physical obstruction presented by the water molecules around the monomer core.

An additional perspective of solvent interactions with nascent photoproducts is revealed in the resonant scattering of photodetached electrons by the solvent molecules. Changes in the PADs of NO^- are monitored as a function of electron kinetic energy in the $\text{NO}^-(\text{N}_2\text{O})_n$ and $\text{NO}^-(\text{H}_2\text{O})_n$ cluster anions. In contrast with hydration, angular distributions become progressively more isotropic for the N_2O case, particularly when the photoelectron kinetic energies are in the vicinity of the $^2\Pi$ shape resonance of the N_2O solvent molecules.

First time observation of the $[\text{M}-2\text{H}]^-$ anion of dimethylsulfoxide (DMSO) is

achieved by chemical ionization of DMSO by O^- . Photoelectron images of this organic anion and its monohydrated cluster are reported. Based on the spectra we have described the anions as CH_3SOCH^- . Observed photodissociation products are $HCSO^-$ and SO^- , with the latter dissociation channel highly enhanced in the monohydrated case. Deprotonated anions of acetonitrile were also found by chemical ionization with O^- , and we report the observation of both $HCCN^-$ as well as H_2CCN^- anions and their clusters.

These findings present a wide range of photochemical processes that help elucidate the roles that various solvents play in determining the structure and reactivity of anions. These results also prove clusters as valuable tools for the detailed study of embryonic states of the condensed phase.

9.2 Future Directions

This section describes some possible future experiments. This discussion about future work is intended to inspire further investigation on these topics and perhaps expand on the findings already presented in this dissertation.

9.2.1 Photoelectron Imaging of Mass-Selected Photofragments

We have described in Chapter 2 the new imaging assembly that would be capable of imaging the photoelectrons of mass-selected photofragments by making use of the ability of the reflectron to refocus the fragment ions on the off-axis detector located below the principal molecular beam. This is in principle a two laser beam experiment where the first laser beam would dissociate the parent anion and a second laser would be used to photodetach the electrons from a photofragment anion as it passes below the first laser

interaction region on its reversed trajectory to the off-axis detector. The assembly consists of four electrodes, where an additional plate is added to our previous three-plate assembly (see for example the work by Surber [1]) to focus the photoelectrons from the reflected photofragments onto our imaging detector.

The potential applications of such arrangement are many. An attractive aspect is the capability of obtaining the photoelectron spectra of novel anions that are not typically created by our electron impact source. For example, the “dipole-bound” CH_3CN^- negative ion was prepared by the photodissociation of the $\text{I}^- \cdot \text{CH}_3\text{CN}$ ion-molecule complex [204].

Conformational changes could also be detected by this technique. If the geometry of a core anion changes upon absorption of a photon, followed by some evaporation of solvent monomers, the mass spectroscopy results would only indicate that there is a solvent evaporation channel, however the photoelectron spectra of the fragments would reveal if isomerization took place followed by a relaxation process mediated by the evaporation of solvent molecules.

Finally, the ability to obtain photoelectron images (and corresponding spectra) of anions formed in excited electronic states is also very promising. This will not only complement the information needed to characterize the dynamics and energy disposal of the photodissociation process, but can also be used to obtain experimental information about excited anionic states.

9.2.2 Studies of Hydration Stabilized Anions

In this dissertation we observed how a single water molecule was sufficient to stabilize the metastable CO_2^- radical anion. The addition of a larger number of water solvents not only stabilized the anion, but also provided new pathways for excited state dynamics. Surber et al. [210] found that a single water molecule was sufficient to stabilize the OCS^- anion. Another striking example of the hydration interaction is given by the uracil anion. Solvation of dipole bound, uracil anions by noble gases give anionic complexes which, according to their photoelectron spectra, remained dipole bound [211]. However, upon solvation of the uracil anion by a single water molecule, a drastic change was observed in the photoelectron spectrum of the resulting anionic complex where only a valence anionic state was observed, with no evidence of dipole binding remaining [211, 207]. This behavior was also observed in the photoelectron spectra of the anions of thymine and cytosine, where in each case a single water molecule was sufficient to stabilize the corresponding valence anion [207].

9.2.3 $[\text{M}-n\text{H}]^-$, $n = 1, 2$ Anions

Another method of creating stable valence anions is by deprotonation. This can be achieved by dissociative electron attachment or by chemical ionization. For example, Neumark and co-workers recently reported photoelectron images of deprotonated thymine and cytosine anions [212]. A wide variety of radicals and biradicals can be generated by abstraction of a proton or abstraction of H_2^+ from many organic molecules as shown in Chapters 7 and 8. Several anions produced from cyclic and acyclic ketones have been successfully generated by this ionization method [187]. It would be interesting

to obtain the photoelectron spectra as well as to characterize the possible photochemistry occurring in such systems, with acetone as simplest ketone to be studied next.

REFERENCES

- [1] E. Surber, Ph.D. thesis, University of Arizona (2005).
- [2] R. E. Continetti, *Ann. Rev. Phys. Chem.* **52**, 165 (2001).
- [3] M. Johnson and W. Lineberger, in *Techniques for the Study of Ion Molecule Reactions*, edited by J. Farrar and W. Saunders (Wiley, New York, 1988), pp. 591–635.
- [4] A. W. Castleman and K. H. Bowen, *J. Phys. Chem.* **100**, 12911 (1996).
- [5] A. Sanov and W. C. Lineberger, *Phys. Chem. Chem. Phys.* **6**, 2018 (2004).
- [6] D. W. Chandler and P. L. Houston, *J. Chem. Phys.* **87**, 1445 (1987).
- [7] A. J. R. Heck and D. W. Chandler, *Annu. Rev. Phys. Chem.* **46**, 335 (1995).
- [8] E. Surber and A. Sanov, *J. Chem. Phys.* **116**, 5921 (2002).
- [9] R. Mabbs, E. Surber, and A. Sanov, *Analyst* **128**, 765 (2003).
- [10] R. Mabbs and A. Sanov, *Int. Rev. Phys. Chem.* **27**, 53 (2008).
- [11] J. Cooper and R. N. Zare, in *Atomic Collision Processes*, edited by S. Geltman, K. T. Mahanthappa, and W. E. Brittin (Gordon and Breach, Science Publishers, New York, London, Paris, 1968), vol. XI-C of *Lectures in Theoretical Physics*, pp. 317–337.
- [12] J. Cooper and R. N. Zare, *J. Chem. Phys.* **48**, 942 (1968).
- [13] J. Cooper, *J. Chem. Phys.* **49**, 4252 (1968).
- [14] M. E. Nadal, P. D. Kleiber, and W. C. Lineberger, *J. Chem. Phys.* **105**, 504 (1996).
- [15] E. Surber, R. Mabbs, and A. Sanov, *J. Phys. Chem. A* **107**, 8215 (2003).
- [16] C. E. Klots and R. N. Compton, *J. Chem. Phys.* **69**, 1636 (1978).
- [17] I. Shimamura and K. Takahashi, eds., *Electron-Molecule Collisions*, Physics of Atoms and Molecules (Plenum Press, New York, 1984).
- [18] M. L. Alexander, N. E. Levinger, M. A. Johnson, D. Ray, and W. C. Lineberger, *J. Chem. Phys.* **88**, 6200 (1988).

- [19] M. E. Nadal, Ph.D. thesis, University of Colorado (1996).
- [20] L. A. Posey, M. J. DeLuca, and M. A. Johnson, *Chem. Phys. Lett.* **131**, 170 (1986).
- [21] R. J. Cotter, in *Time-of-Flight Mass Spectrometry (ACS Symposium Series 549)*, edited by R. J. Cotter (American Chemical Society, Washington, 1994), pp. 16–48.
- [22] B. A. Mamyrin, V. I. Karataev, D. V. Shmikk, and V. A. Zagulin, *Sov. Phys. -JEPT* **37**, 45 (1973).
- [23] U. Boesl, R. Weinkauf, and E. W. Schlag, *Int. J. Mass Spectrom. Ion Process.* **112**, 121 (1992).
- [24] A. T. J. B. Eppink and D. H. Parker, *Rev. Sci. Instrum.* **68**, 3477 (1997).
- [25] A. Osterwalder and D. Neumark (personal communication).
- [26] V. Dribinski, A. Ossadtchi, V. A. Mandelshtam, and H. Reisler, *Rev. Sci. Instrum.* **73**, 2634 (2002).
- [27] S. J. Cavanagh, S. T. Gibson, M. N. Gale, C. J. Dedman, E. H. Roberts, and B. R. Lewis, *Phys. Rev. A* **76**, 052708 (2007).
- [28] J. L. Hall and M. W. Siegel, *J. Chem. Phys.* **48**, 943 (1968).
- [29] D. Hanstorp, C. Bengtsson, and D. J. Larson, *Phys. Rev. A* **40**, 670 (1989).
- [30] E. P. Wigner, *Phys. Rev.* **73**, 1002 (1948).
- [31] Y. Itikawa, *J. Phys. Chem. Ref. Data* **31**, 749 (2002).
- [32] M. J. W. Boness and G. J. Schulz, *Phys. Rev. A* **9**, 1969 (1974).
- [33] K. H. Kochem, W. Sohn, N. Hebel, K. Jung, and H. Ehrhardt, *J. Phys. B* **18**, 4455 (1985).
- [34] H. Estrada and W. Domcke, *J. Phys. B* **18**, 4469 (1985).
- [35] L. A. Morgan, *Phys. Rev. Lett.* **80**, 1873 (1998).
- [36] D. Field, N. C. Jones, S. L. Lunt, and J. P. Ziesel, *Phys. Rev. A* **64**, 022708 (2001).
- [37] G. A. Ropp and C. E. Melton, *J. Am. Chem. Soc.* **80**, 3509 (1958).
- [38] C. D. Cooper and R. N. Compton, *Chem. Phys. Lipids* **14**, 29 (1972).
- [39] C. D. Cooper and R. N. Compton, *J. Chem. Phys.* **59**, 3550 (1973).

- [40] D. Schroder, C. A. Schalley, J. N. Harvey, and H. Schwarz, *Int. J. Mass Spec.* **187**, 25 (1999).
- [41] R. Middleton and J. Klein, *Phys. Rev. A* **60**, 3786 (1999).
- [42] M. Knapp, O. Echt, D. Kreisler, T. D. Mark, and E. Recknagel, *Chem. Phys. Lett.* **126**, 225 (1986).
- [43] M. Krauss and D. Neumann, *Chem. Phys. Lipids* **14**, 26 (1972).
- [44] T. Sommerfeld, *J. Phys. B* **36**, L127 (2003).
- [45] T. Sommerfeld, H. D. Meyer, and L. S. Cederbaum, *Phys. Chem. Chem. Phys.* **6**, 42 (2004).
- [46] W. Vanroose, Z. Y. Zhang, C. W. McCurdy, and T. N. Rescigno, *Phys. Rev. Lett.* **92**, 053201 (2004).
- [47] W. Vanroose, C. W. McCurdy, and T. N. Rescigno, *Phys. Rev. A* **66**, 032720 (2002).
- [48] C. W. McCurdy, W. A. Isaacs, H. D. Meyer, and T. N. Rescigno, *Phys. Rev. A* **67**, 042708 (2003).
- [49] M. K. Raarup, H. H. Andersen, and T. Andersen, *J. Phys. B* **32**, L659 (1999).
- [50] A. Dreuw and L. S. Cederbaum, *J. Phys. B* **32**, L665 (1999).
- [51] A. F. Jalbout, *Mol. Phys.* **100**, 3691 (2002).
- [52] K. Kuchitsu, ed., *Structure Data of Free Polyatomic Molecules*, vol. II/21 (Landolt-Börnstein, Berlin, 1992).
- [53] G. L. Gutsev, R. J. Bartlett, and R. N. Compton, *J. Chem. Phys.* **108**, 6756 (1998).
- [54] R. N. Compton, P. W. Reinhardt, and C. D. Cooper, *J. Chem. Phys.* **63**, 3821 (1975).
- [55] M. K. Scheller, R. N. Compton, and L. S. Cederbaum, *Science* **270**, 1160 (1995).
- [56] A. Rauk, D. A. Armstrong, and D. Yu, *Int. J. Chem. Kinet.* **26**, 7 (1994).
- [57] S. Barsotti, T. Sommerfeld, M. W. Ruf, and H. Hotop, *Int. J. Mass Spectrom.* **233**, 181 (2004).
- [58] W. E. Thompson and M. E. Jacox, *J. Chem. Phys.* **111**, 4487 (1999).
- [59] M. F. Zhou and L. Andrews, *J. Chem. Phys.* **110**, 2414 (1999).
- [60] K. H. Bowen and J. G. Eaton, in *The Structure of Small Molecules and Ions*, edited by R. Naaman and Z. Vager (Plenum, New York, 1988), pp. 147–169.

- [61] D. M. Tomazela, A. A. Sabino, R. Sparrapan, F. C. Gozzo, and M. N. Eberlin, *J. Am. Soc. Mass Spec.* **17**, 1014 (2006).
- [62] T. N. Rescigno, D. A. Byrum, W. A. Isaacs, and C. W. McCurdy, *Phys. Rev. A* **60**, 2186 (1999).
- [63] T. Sommerfeld, *Phys. Chem. Chem. Phys.* **3**, 2394 (2001).
- [64] M. Allan, *J. Phys. B* **35**, L387 (2002).
- [65] D. Field and L. B. Madsen, *J. Chem. Phys.* **118**, 1679 (2003).
- [66] T. Sommerfeld, *Phys. Chem. Chem. Phys.* **4**, 2511 (2002).
- [67] M. J. Frisch, G. W. Trucks, H. B. Schlegel, G. E. Scuseria, M. A. Robb, J. R. Cheeseman, V. G. Zakrzewski, J. A. Montgomery, R. E. Stratmann, J. C. Burant, et al., *GAUSSIAN 98* (1998).
- [68] M. Allan, *Lecture notes*, 332th Wilhelm und Else Heraeus-Seminar "Processes driven by Low Energy Electron-Molecule Interactions", URL http://www.chem.unifr.ch/ma/dir_allan/Lectures.html.
- [69] C. E. Klots and R. N. Compton, *J. Chem. Phys.* **67**, 1779 (1977).
- [70] A. Stamatovic, K. Leiter, W. Ritter, K. Stephan, and T. Mark, *J. Chem. Phys.* **83**, 2942 (1985).
- [71] S. Barsotti, E. Leber, M. W. Ruf, and H. Hotop, *Int. J. Mass Spectrom.* **220**, 313 (2002).
- [72] I. Fabrikant and H. Hotop, *Phys. Rev. Lett.* **94** (2005).
- [73] I. Fabrikant, *J. Phys. B* **38**, 1745 (2005).
- [74] M. L. Alexander, M. A. Johnson, N. E. Levinger, and W. C. Lineberger, *Phys. Rev. Lett.* **57**, 976 (1986).
- [75] I. A. Shkrob and M. C. Sauer, *J. Phys. Chem. B* **105**, 4520 (2001).
- [76] I. A. Shkrob, M. C. Sauer, C. D. Jonah, and K. Takahashi, *J. Phys. Chem. A* **106**, 11855 (2002).
- [77] M. Michaud, E. M. Hebert, P. Cloutier, and L. Sanche, *J. Chem. Phys.* **126** (2007).
- [78] S. H. Fleischman and K. D. Jordan, *J. Phys. Chem.* **91**, 1300 (1987).
- [79] M. J. DeLuca, B. Niu, and M. A. Johnson, *J. Chem. Phys.* **88**, 5857 (1988).

- [80] T. Tsukuda, M. A. Johnson, and T. Nagata, *Chem. Phys. Lett.* **268**, 429 (1997).
- [81] T. Tsukuda, M. Saeki, R. Kimura, and T. Nagata, *J. Chem. Phys.* **110**, 7846 (1999).
- [82] S. A. Corcelli, J. A. Kelley, J. C. Tully, and M. A. Johnson, *J. Phys. Chem. A* **106**, 4872 (2002).
- [83] J. W. Shin, N. I. Hammer, M. A. Johnson, H. Schneider, A. Gloss, and J. M. Weber, *J. Phys. Chem. A* **109**, 3146 (2005).
- [84] V. Vorsa, Ph.D. thesis, University of Colorado (1996).
- [85] T. Habteyes, L. Velarde, and A. Sanov, *J. Chem. Phys.* **126**, 154301 (2007).
- [86] R. Mabbs, E. Surber, and A. Sanov, *Chem. Phys. Lett.* **381**, 479 (2003).
- [87] R. Mabbs, E. Surber, L. Velarde, and A. Sanov, *J. Chem. Phys.* **120**, 5148 (2004).
- [88] M. Dewar, *Proc. Cambridge Phil. Soc.* **45**, 638 (1949).
- [89] L. Combs, *Int. J. Quantum Chem.* **11**, 1001 (1977).
- [90] M. Saeki, T. Tsukuda, and T. Nagata, *Chem. Phys. Lett.* **340**, 376 (2001).
- [91] M. Saeki, T. Tsukuda, and T. Nagata, *Chem. Phys. Lett.* **348**, 461 (2001).
- [92] M. Saeki, T. Tsukuda, S. Iwata, and T. Nagata, *J. Chem. Phys.* **111**, 6333 (1999).
- [93] O. P. Balaj, C. K. Siu, I. Balteanu, M. K. Beyer, and V. E. Bondybey, *Chem. Eur. J.* **10**, 4822 (2004).
- [94] E. Surber, R. Mabbs, T. Habteyes, and A. Sanov, *J. Phys. Chem. A* **109**, 4452 (2005).
- [95] C. E. Klots, *J. Chem. Phys.* **71**, 4172 (1979).
- [96] J. P. Keene, Y. Raef, and A. J. Swallow, in *Pulse Radiolysis*, edited by M. Emert, J. P. Keene, and A. J. Swallow (Academic Press, London, New York, 1965), pp. 99–106.
- [97] A. Fojtik, G. Czapski, and A. Henglein, *J. Phys. Chem.* **74**, 3204 (1970).
- [98] G. V. Buxton and R. M. Sellers, *J. Chem. Soc., Faraday Trans. I* **69**, 555 (1973).
- [99] R. Flyunt, M. N. Schuchmann, and C. von Sonntag, *Chem. Eur. J.* **7**, 796 (2001).
- [100] T. Habteyes, Ph.D. thesis, University of Arizona (2008).
- [101] T. Tsukuda and T. Nagata, *J. Phys. Chem. A* **107**, 8476 (2003).

- [102] *CRC Handbook of Chemistry and Physics* (CRC Press, Boca Raton, Florida, 2008), 88th ed.
- [103] G. J. Schulz, *Phys. Rev.* **128**, 178 (1962).
- [104] M. J. W. Boness and G. J. Schulz, *Phys. Rev. Lett.* **21**, 1031 (1968).
- [105] G. J. Schulz and D. Spence, *Phys. Rev. Lett.* **22**, 47 (1969).
- [106] M. A. Huels, L. Parenteau, P. Cloutier, and L. Sanche, *J. Chem. Phys.* **103**, 6775 (1995).
- [107] G. W. Chantry and D. H. Whiffen, *Mol. Phys.* **5**, 189 (1962).
- [108] K. O. Hartman and I. C. Hisatsune, *J. Chem. Phys.* **44**, 1913 (1966).
- [109] P. J. Linstrom and W. G. Mallard, eds., *NIST Chemistry WebBook, NIST Standard Reference Database No. 69* (National Institute of Standards and Technology, Gaithersburg, MD, 2005), nist standard reference database number 69, june 2005 release ed.
- [110] D. R. Harding, R. E. Weston, and G. W. Flynn, *J. Chem. Phys.* **88**, 3590 (1988).
- [111] M. C. Lin and S. H. Bauer, *J. Chem. Phys.* **50**, 3377 (1969).
- [112] C. Valli, C. Blondel, and C. Delsart, *Phys. Rev. A* **59**, 3809 (1999).
- [113] J. Bentley, J. Y. Collins, and D. M. Chipman, *J. Phys. Chem. A* **104**, 4629 (2000).
- [114] K. Tanaka and E. R. Davidson, *J. Chem. Phys.* **70**, 2904 (1979).
- [115] R. N. Dixon, *Mol. Phys.* **54**, 333 (1985).
- [116] C. E. Klots and R. N. Compton, *J. Chem. Phys.* **67**, 1779 (1977).
- [117] A. Muraoka, Y. Inokuchi, N. Nishi, and T. Nagata, *J. Chem. Phys.* **122**, 094303 (2005).
- [118] T. Habteyes, L. Velarde, and A. Sanov, *Chem. Phys. Lett.* **424**, 268 (2006).
- [119] C. R. Claydon, G. A. Segal, and H. S. Taylor, *J. Chem. Phys.* **52**, 3387 (1970).
- [120] O. J. Orient and S. K. Srivastava, *Chem. Phys. Lett.* **96**, 681 (1983).
- [121] P. J. Chantry, *J. Chem. Phys.* **57**, 3180 (1972).
- [122] A. Stamatovic and G. J. Schulz, *Phys. Rev. A* **7**, 589 (1973).
- [123] R. Dressler and M. Allan, *Chem. Phys.* **92**, 449 (1985).

- [124] M. A. Buntine, D. J. Lavrich, C. E. Dessent, M. G. Scarton, and M. A. Johnson, *Chem. Phys. Lett.* **216**, 471 (1993).
- [125] A. Stamatovic, K. Stephan, and T. D. Mark, *Int. J. Mass Spectrom. Ion Process.* **63**, 37 (1985).
- [126] W. C. Wiley and I. H. McLaren, *Rev. Sci. Instrum.* **26**, 1150 (1955).
- [127] H. Massey, *Negative Ions* (Cambridge University Press, Cambridge, 1976), 3rd ed.
- [128] K. M. Ervin and W. C. Lineberger, in *Advances in Gas Phase Ion Chemistry*, edited by N. G. Adams and L. M. Babcock (JAI, Greenwich, 1992), vol. 1, p. 121.
- [129] M. L. Alexander, Ph.D. thesis, University of Colorado (1987).
- [130] J. C. Bopp, E. G. Diken, J. M. Headrick, J. R. Roscioli, and M. A. Johnson, *J. Chem. Phys.* **124**, 174302 (2006).
- [131] A. A. Viggiano, R. A. Morris, C. A. Deakyne, F. Dale, and J. F. Paulson, *J. Phys. Chem.* **94**, 8193 (1990).
- [132] C. M. Roehl, J. T. Snodgrass, C. A. Deakyne, and M. T. Bowers, *J. Chem. Phys.* **94**, 6546 (1991).
- [133] X. Yang and A. W. Castleman, *J. Am. Chem. Soc.* **113**, 6766 (1991).
- [134] R. G. Keesee and A. W. Castleman, *J. Phys. Chem. Ref. Data* **15**, 1011 (1986).
- [135] R. G. Keesee, N. Lee, and A. W. Castleman, *J. Am. Chem. Soc.* **101**, 2599 (1979).
- [136] C. Lifshitz, *J. Phys. Chem.* **86**, 3634 (1982).
- [137] D. M. Chipman and J. Bentley, *J. Phys. Chem. A* **109**, 7418 (2005).
- [138] J. R. Roscioli, E. G. Diken, M. A. Johnson, S. Horvath, and A. B. McCoy, *J. Phys. Chem. A* **110**, 4943 (2006).
- [139] L. G. Christophorou and J. K. Olthoff, *Fundamental Electron Interactions* (Kluwer Academic/Plenum, New York, 2004).
- [140] R. Mabbs, E. Surber, and A. Sanov, *J. Chem. Phys.* **122**, 054308 (2005).
- [141] R. Nakanishi, A. Muraoka, and T. Nagata, *Chem. Phys. Lett.* **427**, 56 (2006).
- [142] J. Coe, J. Snodgrass, K. Friedhoff, and K. Bowen, *J. Chem. Phys.* **87**, 4302 (1987).
- [143] J. H. Hendricks, H. L. de Clercq, C. B. Freidhoff, S. T. Arnold, J. G. Eaton, C. Fancher, S. A. Lyapustina, J. T. Snodgrass, and K. H. Bowen, *J. Chem. Phys.* **116**, 7926 (2002).

- [144] M. S. Resat, V. Zengin, M. C. Garner, and R. E. Continetti, *J. Phys. Chem. A* **102**, 1719 (1998).
- [145] M. M. Maricq, N. A. Tanguay, J. C. O'Brien, S. M. Rodday, and E. Rinden, *J. Chem. Phys.* **90**, 3136 (1989).
- [146] M. C. McCarthy, J. W. R. Allington, and K. S. Griffith, *Chem. Phys. Lett.* **289**, 156 (1998).
- [147] C. Winstead and V. McKoy, *Phys. Rev. A* **57**, 3589 (1998).
- [148] F. A. Gianturco and T. Stoecklin, *Eur. Phys. J. D* **40**, 369 (2006).
- [149] M. Kitajima, Y. Sakamoto, R. J. Gulley, M. Hoshino, J. C. Gibson, H. Tanaka, and S. J. Buckman, *J. Phys. B* **33**, 1687 (2000).
- [150] H. Hotop, M. W. Ruf, M. Allan, and I. I. Fabrikant, *Adv. At. Mol. Opt. Phys.* **49**, 85 (2003).
- [151] J. M. Weber, E. Leber, M. W. Ruf, and H. Hotop, *Phys. Rev. Lett.* **82**, 516 (1999).
- [152] L. Velarde, T. Habteyes, E. Grumbling, K. Pichugin, and A. Sanov, *J. Chem. Phys.* **127**, 084302 (2007).
- [153] L. A. Posey and M. A. Johnson, *J. Chem. Phys.* **88**, 5383 (1988).
- [154] S. A. Chacko and P. G. Wenthold, *Mass Spectrom. Rev.* **25**, 112 (2006).
- [155] M. J. Travers, D. C. Cowles, and G. B. Ellison, *Chem. Phys. Lett.* **164**, 449 (1989).
- [156] M. W. Siegel, R. A. Bennett, R. J. Celotta, J. L. Hall, and J. Levine, *Phys. Rev. A* **6**, 607 (1972).
- [157] C. A. Arrington, T. H. Dunning, and D. E. Woon, *J. Phys. Chem. A* **111**, 11185 (2007).
- [158] K. Hiraoka, S. Fujimaki, K. Aruga, and S. Yamabe, *J. Phys. Chem.* **98**, 8295 (1994).
- [159] J. W. Torchia, K. O. Sullivan, and L. S. Sunderlin, *J. Phys. Chem. A* **103**, 11109 (1999).
- [160] A. Snis and I. Panas, *Chem. Phys. Lett.* **305**, 285 (1999).
- [161] A. Alijah and E. S. Kryachko, *J. Mol. Struct.* **844**, 193 (2007).
- [162] J. G. Eaton, S. T. Arnold, and K. H. Bowen, *Int. J. Mass Spectrom. Ion Process.* **102**, 303 (1990).

- [163] E. M. Myshakin, K. D. Jordan, W. H. Robertson, G. H. Weddle, and M. A. Johnson, *J. Chem. Phys.* **118**, 1735 (2003).
- [164] F. A. Akin, L. K. Schirra, and A. Sanov, *J. Phys. Chem. A* **110**, 8031 (2006).
- [165] R. Polak and J. F. Fiser, *Chem. Phys.* **303**, 73 (2004).
- [166] C. G. Bailey, D. J. Lavrich, D. Serxner, and M. A. Johnson, *J. Chem. Phys.* **105**, 1807 (1996).
- [167] K. J. Reed, A. H. Zimmerman, H. C. Andersen, and J. I. Brauman, *J. Chem. Phys.* **64**, 1368 (1976).
- [168] L. E. Machado, L. M. Brescansin, I. Iga, and M. T. Lee, *Eur. Phys. J. D* **33**, 193 (2005).
- [169] R. W. Gra, S. Roszak, and J. Leszczynski, *Asian J. Spectrosc.* **4**, 1 (2000).
- [170] Y. Itikawa and N. Mason, *J. Phys. Chem. Ref. Data* **34**, 1 (2005).
- [171] G. Hanel, T. Fiegele, A. Stamatovic, and T. D. Mark, *Int. J. Mass Spectrom.* **205**, 65 (2001).
- [172] E. Surber and A. Sanov, *J. Chem. Phys.* **118**, 9192 (2003).
- [173] C. Szmytkowski, G. Karwasz, and K. Maciag, *Chem. Phys. Lett.* **107**, 481 (1984).
- [174] S. Oae and Y. Uchida, in *The Chemistry of Sulphones and Sulphoxides*, edited by R. Z. Patai, S. and C. Stirling (John Wiley & Sons, Chichester, 1988), pp. 583–664.
- [175] S. Carle, C. Desfrancois, J. P. Schermann, J. Berges, and C. Houee-Levin, *Int. J. Mass Spectrom.* **205**, 227 (2001).
- [176] C. Desfrancois, H. Abdoulcarime, and J. P. Schermann, *Int. J. Mod. Phys. B* **10**, 1339 (1996).
- [177] N. I. Hammer, K. Diri, K. D. Jordan, C. Desfrancois, and R. N. Compton, *J. Chem. Phys.* **119**, 3650 (2003).
- [178] N. I. Hammer, R. J. Hinde, R. N. Compton, K. Diri, K. D. Jordan, D. Radisic, S. T. Stokes, and K. H. Bowen, *J. Chem. Phys.* **120**, 685 (2004).
- [179] A. G. Harrison, *Chemical Ionization Mass Spectrometry* (CRC Press, Boca Raton, Florida, 1992), 2nd ed.
- [180] E. J. Corey and M. Chaykovsky, *J. Am. Chem. Soc.* **84**, 866 (1962).
- [181] S. Wolfe, A. Stolow, and L. A. Lajohn, *Tetrahedron Lett.* **24**, 4071 (1983).

- [182] P. Speers, K. E. Laidig, and A. Streitwieser, *J. Am. Chem. Soc.* **116**, 9257 (1994).
- [183] S. Dozmorov, *J. Appl. Spectr.* **45**, 957 (1986).
- [184] D. A. Bors and A. Streitwieser, *J. Am. Chem. Soc.* **108**, 1397 (1986).
- [185] E. Buncel, K. T. Park, J. M. Dust, and R. A. Manderville, *J. Am. Chem. Soc.* **125**, 5388 (2003).
- [186] J. Lee and J. J. Grabowski, *Chem. Revs.* **92**, 1611 (1992).
- [187] M. X. Lin and J. J. Grabowski, *Int. J. Mass Spectrom.* **237**, 149 (2004).
- [188] J. H. J. Dawson, A. J. Noest, and N. M. M. Nibbering, *Int. J. Mass Spectrom. Ion Process.* **30**, 189 (1979).
- [189] K. B. Eisenthal, R. A. Moss, and N. J. Turro, *Science* **225**, 1439 (1984).
- [190] S. Moran and G. B. Ellison, *J. Phys. Chem* **92**, 1794 (1988).
- [191] M. J. Frisch, G. W. Trucks, H. B. Schlegel, G. E. Scuseria, M. A. Robb, J. R. Cheeseman, J. J. A. Montgomery, T. Vreven, K. N. Kudin, J. C. Burant, et al., *GAUSSIAN 03* (2004).
- [192] J. A. Dobado, H. Martinez-Garcia, J. M. Molina, and M. R. Sundberg, *J. Am. Chem. Soc.* **121**, 3156 (1999).
- [193] D. G. Leopold, K. K. Murray, and W. C. Lineberger, *J. Chem. Phys.* **81**, 1048 (1984).
- [194] D. G. Leopold, K. K. Murray, A. E. S. Miller, and W. C. Lineberger, *J. Chem. Phys.* **83**, 4849 (1985).
- [195] M. R. Nimlos, G. Davico, C. M. Geise, P. G. Wenthold, W. C. Lineberger, S. J. Blanksby, C. M. Hadad, G. A. Petersson, and G. B. Ellison, *J. Chem. Phys.* **117**, 4323 (2002).
- [196] D. J. Donaldson and S. R. Leone, *J. Chem. Phys.* **85**, 817 (1986).
- [197] D. Liu, W. H. Fang, and X. Y. Fu, *Chem. Phys. Lett.* **325**, 86 (2000).
- [198] J. W. Ho, W. K. Chen, and P. Y. Cheng, *J. Am. Chem. Soc.* **129**, 3784 (2007).
- [199] S. Saito, *Bull. Chem. Soc. Jpn.* **42**, 667 (1969).
- [200] F. Wu, X. R. Chen, and B. R. Weiner, *J. Am. Chem. Soc.* **118**, 8417 (1996).

- [201] J. H. Bowie, M. B. Stringer, and R. N. Hayes, *Rapid. Comm. Mass Spectrom.* **4**, 129 (1990).
- [202] J. Stockdale, F. Davis, R. N. Compton, and C. E. Klots, *Chem. Phys.* **60**, 4279 (1974).
- [203] K. D. Jordan and J. J. Wendoloski, *Chem. Phys.* **21**, 145 (1977).
- [204] C. G. Bailey, C. E. H. Dessent, M. A. Johnson, and K. H. Bowen, *J. Chem. Phys.* **104**, 6976 (1996).
- [205] J. H. Hendricks, H. L. deClercq, S. A. Lyapustrina, T. P. Fancher, T. P. Lippa, J. M. Collins, S. T. Arnold, D. H. Lee, and B. K. H., in *Proc. Yamada Conference XLIII, Structures and Dynamics of Clusters* (Universal Academy, Tokyo, 1995).
- [206] P. J. Campagnola, L. A. Posey, and M. A. Johnson, *J. Chem. Phys.* **92**, 3243 (1990).
- [207] J. Schiedt, R. Weinkauff, D. M. Neumark, and E. W. Schlag, *Chem. Phys.* **239**, 511 (1998).
- [208] X. Yang, X. Zhang, and A. W. Castleman, *J. Phys. Chem.* **95**, 8520 (1991).
- [209] S. Moran, H. B. Ellis, D. J. Defrees, A. D. McLean, and G. B. Ellison, *J. Am. Chem. Soc.* **109**, 5996 (1987).
- [210] E. Surber, S. P. Ananthavel, and A. Sanov, *J. Chem. Phys.* **116**, 1920 (2002).
- [211] J. H. Hendricks, S. A. Lyapustina, H. L. Declercq, and K. H. Bowen, *J. Chem. Phys.* **108**, 8 (1998).
- [212] B. F. Parsons, S. M. Sheehan, T. A. Yen, D. M. Neumark, N. Wehres, and R. Weinkauff, *Phys. Chem. Chem. Phys.* **9**, 3291 (2007).